Final Project Report

Understanding and Improving High-Temperature Structural Properties of Metal-Silicide Intermetallics

Research sponsored by the U.S. Department of Energy,
National Energy Technology Laboratory for the period of
07/15/2001 to 07/14/2004 (with one-year no cost extension to 07/14/2005)

Report Prepared by

Bruce S. Kang (project P.I.)

Mechanical and Aerospace Engineering Department
West Virginia University
Morgantown, WV 26506
October 10, 2005

for

U.S. Department of Energy
under contract **DE-FG02-01ER45899**

PROJECT SUMMARY

The objective of this project was to understand and improve high-temperature structural properties of metal-silicide intermetallic alloys. Through research collaboration between the research team at West Virginia University (WVU) and Dr. J.H. Schneibel at Oak Ridge National Laboratory (ORNL), molybdenum silicide alloys were developed at ORNL and evaluated at WVU through atomistic modeling analyses, thermo-mechanical tests, and metallurgical studies. In this study, molybdenum-based alloys were ductilized by dispersing $MgAl_2O_4$ or MgO spinel particles. The addition of spinel particles is hypothesized to getter impurities such as oxygen and nitrogen from the alloy matrix with the result of ductility improvement. The introduction of fine dispersions has also been postulated to improve ductility by acting as a dislocation source or reducing dislocation pile-ups at grain boundaries. The spinel particles, on the other hand, can also act as local notches or crack initiation sites, which is detrimental to the alloy mechanical properties. Optimization of material processing condition is important to develop the desirable molybdenum alloys with sufficient room-temperature ductility. Atomistic analyses were conducted to further understand the mechanism of ductility improvement of the molybdenum alloys and the results showed that trace amount of residual oxygen may be responsible for the brittle behavior of the as-cast Mo alloys.

For the alloys studied, uniaxial tensile tests were conducted at different loading rates, and at room and elevated temperatures. Thermal cycling effect on the mechanical properties was also studied. Tensile tests for specimens subjected to either ten or twenty thermal cycles were conducted. For each test, a follow-up detailed fractography and microstructural analysis were carried out. The test results were correlated to the size, density, distribution of the spinel particles and processing time. Thermal expansion tests were carried out using thermo-mechanical analyzer (TMA). Results showed that the coefficient of thermal expansion (CTE) value decreases with the addition of spinel and silicide particles. Thermo-cycling tests showed that molybdenum alloy with 6% wt of spinel ($MgAl_2O_4$) developed microcracks which were caused by thermal expansion mismatch between the spinel particles and molybdenum matrix, as well as the processing conditions. Detailed post-mortem studies of microstructures and segregation of impurities to the oxide dispersion/Mo interfaces were conducted using x-ray diffraction (XRD), scanning electron microscpy (SEM), and energy dispersive spectroscopy (EDS).

PUBLICATIONS

Conference Proceedings

1. Study of fracture behavior of molybdenum alloys using moiré interferometry, Chuanyu Feng, Bruce S Kang, Ning Ma and Bernard R. Cooper, submitted to 2005 ASME International Mechanical Engineering Congress and Exposition, Orlando, Florida, November 5-11, 2005.
2. Development of a Transparent Indenter Measurement System and indentation analysis for material mechanical property evaluation, Bruce S. Kang, Chuanyu Feng, submitted to 2005 ASME International Mechanical Engineering Congress and Exposition, Orlando, Florida, November 5-11, 2005.
3. In-situ Indentation TIM System and Material Mechanical Property Evaluation, Chuanyu Feng, Bruce S. Kang, Proceedings of the 2005 SEM Annual Conference and Exposition on Experimental and Applied Mechanics, Portland, Oregon, June 7-9, 2005.
4. Residual Surface Deformation Analysis in IN783 after Spherical Indentations, Chuanyu Feng, Bruce S. Kang, Proceedings of the 2005 SEM Annual Conference and Exposition on Experimental and Applied Mechanics, Portland, Oregon, June 7-9, 2005.
5. Thermomechanical properties of molybdenum alloys with spinel particles, B.S. Kang, C. Feng, J. H. Schneibel, Twentieth Annual International Pittsburgh Coal Conference proceeding. Sep, 2003.

M.S Theses

6. Thermomechanical Properties of Molybdenum Alloys with dispersing MgAl2O4 (Spinel) and MgO Particles, Dongxiang Sun, West Virginia Univeristy, Dec 2003.
7. Thermomechanical Property Evaluation of Molybdenum Alloys, Ashok Varadarajan, West Virginia University, May 2004.
8. Methodology to Determine Post Yield Material Mechanical Properties from Spherical Indentation, Bharath Konda, West Virginia Univeristy, May 2005.
9. Microstructure Evaluations and Thermomechanical Properties of Spinel (MgAl2O4) Dispersed Molybdenum Alloys, Chee Kiat Lee, West Virginia University, August, 2005.

Ph.D Theses

10. Development of an Indentation Method for Material Surface Mechanical Properties Measurement, Ziheng Yao, West Virginia Univeristy, May 2005.
11. Development of a Through Indenter Measurement System and Indentation Analysis for Material Mechanical Property Evaluation, Chuanyu Feng, West Virginia University, August 2005.

TABLE OF CONTENTS

CHAPTER 1 INTRODUCTION

1.1 Introduction

Significant progress is expected during the 2000s in the application of high temperature materials in the aerospace, energy, materials processing and many other fields. FutureGen [1] is being under development at the Office of Fossil Energy, Department of Energy. This futuristic energy program envisions a virtually pollution-free energy plant. Unlike today's single purpose power plants that produce only electricity, the next generation power plant would produce multiple products-perhaps electricity in combination with liquid fuels and chemicals or hydrogen or industrial process heat. It also would not be restricted to a single fuel type; instead, it could process a wide variety of fuels such as coal, natural gas, biomass, petroleum coke (from oil refineries), and municipal waste. It would generate electricity at unprecedented efficiencies, and coupled with carbon sequestration technologies, it would emit little if any greenhouse gases into the atmosphere. The approach of the plan is to develop a suite of technology modules that can be interconnected in different configurations to produce selected products. These modular facilities will be capable of using a multiplicity of fuels to competitively produce a number of commodities at efficiencies greater than 60 percent for coal-based systems and 75 percent for natural gas-based systems with near-zero emissions.

One of the key technologies for developing "21st Century Energy Plant" is the strong demands for special materials that have high strength, high temperature capability, oxidation and hot-corrosion resistance, etc. Most of the land and aircraft turbine components are exposed to severely oxidizing environments and high temperatures during operation. Mechanical integrity under these conditions is critical. A number of Mo-based alloys are currently being developed for high temperature applications (>1000°C) in advanced fossil energy combustion systems [2-5]. These alloys consist typically of Mo_3Si, Mo_5SiB_2, and a molybdenum solid solution phase. The Mo_5SiB_2 phase is required for oxidation resistance. One example is the Molybdenum silicides and Borosilicides. Akinc et al [33-35] investigated intermetallic alloys consisting of Mo_5Si_3, the T2 phase Mo_5SiB_2, and the A15 phase Mo_3Si, which showed excellent oxidation resistance at high temperatures. The ductile molybdenum solid solution phase provides

toughening [6-7]. The room and high temperature fracture toughness is also improved with the existence of a ductile phase α-Mo [36-37]. The goal is to maintain the desired high-temperature mechanical properties while also achieving the required high-temperature oxidation/hot corrosion resistance.

However, since the ductility of molybdenum phase is marginal, ways have to be found to improve it's room-temperature ductility. In the 1960's, Scruggs found that powder-metallurgical Cr can be ductilized by addition of MgO particles that transform into $MgCr_2O_4$ spinel particles [8]. Under the support of the DOE Fossil Energy Materials Program, M. P. Brady et al. verified this ductilizing effect [9]. They determined that segregation of detrimental impurities such as nitrogen to the particle-matrix interface is one of the factors responsible for ductilization. Although significant, M. P. Brady et al. argued that the observed impurity segregation/precipitation does not appear to be unique to or a special property of spinel phase dispersions in Cr. And the additions of MgO did lower the yield strength of Cr (tensile and compressive) compare to other tested samples. The ductility effect is also hypothesized to be the ability of $MgO/MgCr_2O_4$ dispersions to be better mechanically tolerated by Cr than other oxide and ceramic phase dispersions. Scruggs also found that Mo can be ductilized by adding $MgAl_2O_4$ or $NiAl_2O_4$ spinel particles [10]. Recently, Schneibel et al. showed that Mo with 3.4wt% $MgAl_2O_4$ micro oxide particles (vacuum hot-pressed at 1800°C for one hour) showed substantial increase of room-temperature ductility [11].

1.2 Objectives

The objective of this project was to understand and improve the high-temperature structural properties of metal-silicide intermetallics. Through the collaborative research work between the research team at West Virginia University (WVU) and Dr. J.H. Schneibel at Oak Ridge National Laboratory (ORNL), molybdenum silicide alloys targeted for land-based power plant turbines able to withstand temperature exceeding 1000ºC were developed at ORNL and evaluated at WVU through atomistic modeling analyses, thermo-mechanical tests, and metallurgical studies. The spinel particles can cause several competing effects: (1) particles as crack nucleation sites – embrittlement,

(2) particles as dislocation nucleation sites – ductilization, and (3) particles or particles interfaces as getters of detrimental impurities such as oxygen and nitrogen.

Based on the as-received molybdenum alloys, mechanical tests, including three-point-bending and uniaxial tensile tests, were conducted at both room and elevated temperatures. Three-point-bending specimen with notches was studied to evaluate the fracture toughness and detailed crack tip deformation analysis. Tensile tests were carried out on dog-bone specimens to study the loading rate effects, in which two different loading rates were applied; slow loading rate (0.00254mm/min) and fast loading rate (0.254mm/min). Thermal cycling effects were also studied for alloys with different dispersing spinel particles. Three types of tests, consisting of either 10 or 20 thermal cycles were conducted. Post-mortem SEM fractography analysis, microstructural analyses and Energy Dispersive Analysis of X-ray (EDAX) were conducted to study the fracture mode, thermal cycle effects and chemical composition.

By using Thermal Mechanical Analyzer (TMA), the coefficient of thermal expansion (CTE) of the test alloys was investigated. Post-mortem microstructural analyses of tested specimen using Scanning Electron Microscope (SEM) and Energy Dispersive Spectroscopy (EDX) were conducted to correlate the CTE with certain chemical composition.

The thermomechanical properties of spinel ($MgAl_2O_4$) dispersed molybdenum alloys and the segregation (gettering) of impurities to the oxide dispersion/Mo interfaces were also investigated through thermal cycling tests at temperature of 650°C and 1000°C. A series of post-mortem microstructure evaluation were conducted using X-ray diffraction (XRD), SEM, and Qualitative Energy Dispersive Spectroscopy (EDS).

CHAPTER 2 BACKGROUND

In this chapter, the background information presented will include a concise description of superalloys, which are the current choice for high temperature applications, such as turbine engines. Then the so-called ultra-high temperature materials, especially intermetallic compounds will be described followed by Mo alloys. Finally, Mo-Si-B development will be discussed.

2.1 Superalloys

The term "superalloy" was first used shortly after World War II to describe a group of alloys developed for use in turbo superchargers and aircraft turbine engines that required high performance at elevated temperatures [12]. The range of applications for which superalloys are used has expanded to other areas and now includes aircraft and land-based gas turbines, rocket engines, chemical, and petroleum plants. They are particularly well suited for these demanding applications because of their ability to retain most of their strength even after long exposure times above 650°C(1,200°F). The superalloys may roughly be divided into three groups based on nickel, cobalt and iron alloys. As technology advances, the need for higher operating temperature arises (for example, recently the turbine inlet temperature is increasing to temperature around 1450°C [13]), which exceeds the limit temperature capability of the superalloys whose melting points are lower than 1400°C.

2.2 Ultra-high temperature materials

For further development of high temperature and high efficiency gas turbines, a series of new high temperature materials are needed which should have superior temperature capability than those of the traditional superalloys. These materials are called “ultra-high temperature materials” [14]. Table 2.1 shows a classification of the ultra-high temperature materials [15].

Table 2. 1 Classification of the ultra-high temperature materials

Metallics	* Intermetallic compounds(IMCs): TiAl, NiAl, MoSi2, Nb3Al, etc. * Refractory metals and alloys: W, Ta, Mo, Nb, etc.
Ceramics	*Oxides: Al2O3, SIALON, Al2O3/YAG directionally solidified eutectic (MGCMeltgowth composite), etc *Non-oxides: SiC, Si3N4, etc.
Composites	*Metal matrix composites(MMC): SiC/Ti, SiC/TiAl, W/Superalloy, etc. *Ceramic matrix composites(CMC): SiC/SiC, SiC/LAS, C/SiC, etc. *Carbon/Carbon composites(C/C):C/C *Functionally graded materials(FGM): TiB/Ni, Al2O3+ZrO2/Ni, etc.

2.3 Intermetallics

The superalloys paved the way to the intermetallic material which has better high temperature properties than those of superalloys. Intermetallic material is defined as a "mixture of two metallic elements in a specific proportion which forms a different periodic crystalline structure different from those of the original elements". They are often called "bulk intermetallics" [23]. They differ in a number of important ways from conventional metallic alloys. Conventional alloys consist basically of a disordered solid solution of one or more metallic elements and they do not have any particular chemical formula, and are best described as consisting of a base material to which certain percentages of other elements have been added. In chemical terms, alloys are mixtures of phases. For example, a popular stainless steel has the composition Fe-18%Cr-8%Ni. An intermetallics compound, on the other hand, is a particular chemical compound based on a definite atomic formula, with a fixed or narrow range of chemical composition. An example could be $MoSi_2$. Silicides are considered as intermediate materials between ceramics and metals. For example, transition metal silicides are often classified as intermetallic compounds because of the shown similarities; nevertheless silicon is a semiconductor and not a metal. Crystal structure of silicon is shown in Figure 2.1. The atoms in conventional alloys are linked with relatively weak metallic bonds, while the bonds in intermetallics may be partly ionic or covalent, and therefore stronger. These particular structure of intermetallic compounds give the intermetallics their characteristic

properties - high melting points and great strength (particularly at high temperatures), but poor ductility.

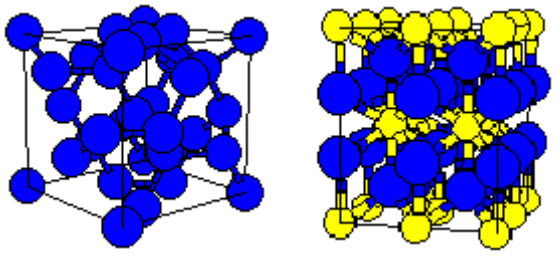

Figure 2.1 Crystal structures of silicon and $MoSi_2$

The particular structure of intermetallic compounds is because of the respectively larger strength of bounding between the unlike atoms than between like atoms. The result is an ordered atom distributions where atoms are preferentially surrounded by unlike atoms. This strength of bounding is the main reason of the high hardness of intermetallic compounds that can be observed by the modes of fracture. In fact, intermetallic compounds have three different modes of fracture such as: intergranular fracture, transgranular cleavage and a mixed of these two modes, as shown in Figure.2.2.

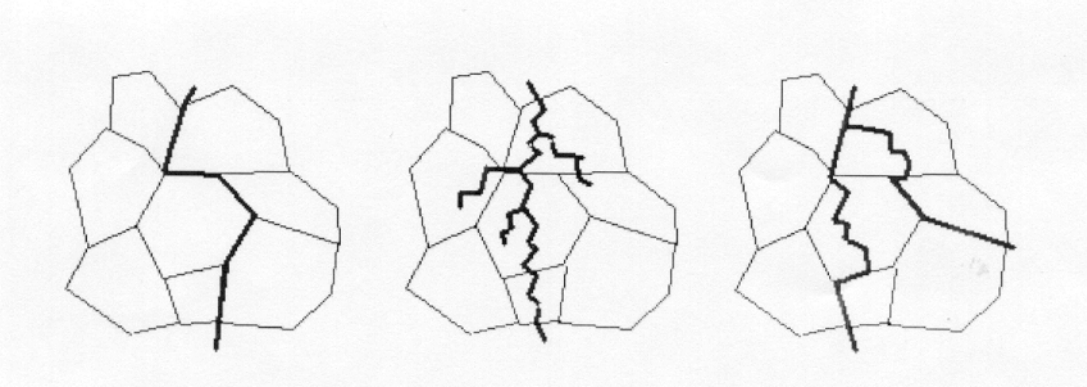

Figure 2.2 Fracture modes on intermetallic compounds

Intermetallics have been recognized as potential candidates for a variety of high temperature structural applications to operate due to their high specific modulus, strength, and excellent oxidation and corrosion resistance. However, the lack of sufficient room temperature ductility of the alloys limited the usage of intermetallics in general thus far. Therefore, recent effort to develop structural intermetallic alloys has been focused on

improving room temperature ductility and toughness to raise their potential for practical applications.

2.4 Molybdenum alloys

Molybdenum, which is hard silvery-white metal, belongs to the group 6 and period 5 of the periodic table (transition metals). Molybdenum has a body-centered cubic (bcc) crystal structure. It has a high melting point (2623^{o}C) [24] with high strength at high temperature. It has a high elastic modulus which makes it in the applications which require high stiffness and low weight. It has a very good thermal conductivity and low coefficient of thermal expansion. The important properties of molybdenum at room temperature are given in Table 2.2.

Table 2.2 Table of selected properties of Molybdenum at room temperature [24].

Atomic Symbol	Mo
Density	10.22 g/cm^3
Boiling Point	4639^{o}C
Melting Point	2636^{o}C
Crystal Structure	BCC
Young's Modulus (E)	324 GPa
Yield Strength[1,2]	690 MPa
Tensile Strength[2]	835 MPa
Elongation[2]	12%
Hardness[2]	240 HV
Coefficient of Thermal Expansion	4.9 X 10-6 /^{o}C
Thermal Conductivity	135 W/(mK)
Specific Heat	0.27 J/kg K
Poisson's Ratio	0.321
Electrical Resistivity	0.06 μ Σm

The property of molybdenum which makes it not suitable for high temperature structural material is its oxidation resistance at high temperature. It oxidizes readily at high temperature and forms MoO_2 in the presence of oxygen partial pressures, which is volatile in nature around 700^oC [16], as the temperature raises it forms MoO_3, which readily vaporizes at high temperature (~800^oC) hence at anytime there is no steady state oxide formation in molybdenum.

$$Mo(s) + O_2\,(g) \mid MoO_2(s)$$

As the temperature increases, it forms

$$MoO_2(s) + 1/2\ O_2\,(g) \mid MoO_3\,(g)$$

Whereas, when the Molybdenum when mixed with silica it forms molybdenum disilicide ($MoSi_2$) which has very good oxidation resistance at high temperature, because of the formation of the thin protective and adherent silica layer in high oxygen partial pressures at high temperatures.

Generally, molybdenum metal is developed by casting or by powder metallurgy techniques, in which Mo powder is hydrostatically compacted and sintered at high temperature (2100^oC). Hot working is done in the 850^oC-1250^oC range. As discussed in the oxidation of molybdenum alloy it forms a volatile oxide when heated above 650^oC, and thus limiting the use of alloys at high temperature only in oxidizing free or vacuum environment. Molysilicide, are made by pressure sintering techniques. This material is generally used as heating element and its properties made it a possible candidate material for high temperature structural applications. The main aspects are moderate density, high melting point, excellent oxidation resistance and high Young's modulus at elevated temperatures. But the main drawbacks of using these alloys as structural material are low fracture toughness at less than 1000^oC and poor creep resistance above 1200^oC. Table 2.3 shows the general physical and mechanical properties of molybdenum disilicide.

Table 2.3 Selected properties of Molybdenum Disilicide at room temperature [24]

Density (g.cm-3)	6.29
Melting Point (^{o}C)	2230
Young's Modulus (GPa)	430
Bend Strength (MPa)	250
Fracture Toughness K1C (MPa.m0.5)	3
Hardness (GPa)	9
Resistivity (ohm.cm)	3.5 x 10-7

In 1981, Oak Ridge National Laboratory started a program to increase understanding of intermetallic compounds and develop scientific principles for improving their properties. Similar research in Japan suggested that addition of small amounts of boron can make nickel aluminide compound more ductile, subsequently, Oak Ridge researchers led by Chain T. Liu determined the mechanism of increasing ductility with boron addition to the base Nickel aluminide alloy. Since then, there has been considerable research work showing that boron-modified molybdenum silicide alloys display an improved pest resistance as compared to unmodified molybdenum silicides [6-7]. The Mo-Si-B intermetallic system utilize the concept of ductile-phase toughening mechanism through in-situ processing techniques to incorporate ductile phase (α-Mo) in a brittle Mo matrix. For purposes of oxidation resistance, it is better to have a relatively small amount of Mo, but there is a cracking problem for Molybdenum alloys containing less than 50% α-Mo. Selecting the correct proportions of the three components is important but difficult.

2.4.1 Strength

The $MoSi_2$, in the polycrystalline form, exhibits a brittle-to-ductile transition in the vicinity of 1000^{o}C. It has a high thermal conductivity which is very beneficial for increased cooling effectiveness of engine components. The room temperature mechanical strength of the $MoSi_2$ is low when compared to other intermetallics because the brittle-to-

ductile transition temperature is around 1000^{o}C and hence it is limited to brittle fracture, while at high temperature it is governed by plastic flow. Above the DBTT (900-1000^{o}C) of $MoSi_2$, the ductility is greater when compared to other structural intermetallics and the fracture toughness will be high with a good resistance to catastrophic fracture, thus making it more dependable [6]. Depending upon the heat treatment and the composition the flexure strength varies from 300 to 600 MPa. Despite the high strength the alloys shows plasticity at temperature around 1400^{o}C. The alloys retain a reasonably high strength at 1200^{o}C showing their potential as high temperature structural materials.

2.4.2 Oxidation resistance

The oxidation resistance of the $MoSi_2$ is significant when compared to other intermetallic compounds based on titanium, niobium and tantalum composites as well as the single crystal nickel-based superalloy [7]. The addition of the silica makes the alloy to have a high oxidation resistance because at high temperature, the silica forms a thin layer which acts as a barrier and reduces the oxygen permeation rate. The addition of boron to the $MoSi_2$ increases the oxidation resistance as it forms a glassy layer of borosilicate [18].

2.4.3 Fracture toughness

The fracture toughness of the $MoSi_2$ decreases while the temperature increases, this was overcome by adding 2 wt% C which increases the fracture toughness [21]. The fracture mode also changes from intergranular to transgranular due to the addition of the C and the removal of the silica grain boundary phase reaction with carbon.

2.4.4 Microstructure

Depending upon the composition and heat treatment, a wide range of microstructure can be obtained. After grinding and polishing and viewing the microstructure of the specimens using SEM. Annealing causes a much more uniform microstructure of Mo_3Si particles. Finer grain alloys generally have Grain Boundary

Sliding (GBS), which is their principal deformation mode. The compounds, which are rich in Mo. like Mo_3Si, Mo_5Si_3, Mo_5SiB_2, MoB, Mo_2B are brittle at ambient temperature. The Mo_5SiB_2 creates a number of ternary phase fields, which allows controlling the mechanical properties by micro structural manipulations.

2.4.5 Applications

Due to its superior high temperature mechanical properties, molybdenum alloy has been in use by various industries. Molybdenum's most important use is as an alloying addition in steel. It provides tool steels and stainless steels with better wear resistance, strength and toughness. It also increases hot strength and corrosion resistance. Due to the alloy's good high temperature mechanical properties and electrical conductivity[24], some of the applications are nuclear reactor control rod production, rocket skirts, cones and heart shields, missile components heat shields in high temperature vacuum furnaces. Molybdenum is added in the form of molybdenum oxide or ferromolybdenum. Molybdenum also is used in nickel- and cobalt-base high performance superalloys for turbine engine components [15], which improve high temperature strength and corrosion resistance. Molybdenum exhibits valences of zero to six; as a result it or its compounds are used in catalysts in oxidation/reduction reactions, for organic synthesis and for a wide variety of petrochemical and pharmaceutical reactions. Molybdenum disulfide powder is a natural lubricant and is used in lubricating oils and greases. It is an effective lubricant in vacuum and at high temperatures. It is very useful in preventing galling or seizing of metals under severe conditions. It has a low coefficient of friction, resists extreme pressures, shears readily and adheres to metals and plastics [39].

2.5 Spinel and its properties

Spinel is an ancient name that originally referred to red gemstones, which today, we recognize as a mixture of a metal monoxide and a metal sesquioxide which combine according to the general formula MO.M2O3 (or MM2O4); where the M's may be the same or dissimilar metals. In this research work, the spinel is crystals of magnesium aluminum oxide, MgAl2O4. Spinels are documented in literature dating as early as the

sixteenth century. Spinels have commanded the attention of both scientists and engineers in recent years. It has a hardness value of 8 in Moh's scale. The specific gravity is about 3.58 to 3.61. The cleavage of the spinel particle is imperfect and the fracture type is either conchoidal or uneven. In the 1960's, Scruggs found that powder-metallurgical Cr can be ductilized by addition of MgO particles that transform into $MgCr_2O_4$ spinel particles [8]. Under the support of the DOE Fossil Energy Materials Program, M. P. Brady et al. verified this ductilizing effect [9]. He determined that segregation of detrimental impurities such as nitrogen to the particle-matrix interface is one of the factors responsible for ductilization. Scruggs found also that Mo is ductilized by adding $MgAl_2O_4$ or $NiAl_2O_4$ spinel particles [10]. The Spinel discussed here ($MgAl_2O_4$) is formed by solid-state interaction of magnesia and alumina. The Coefficient of Thermal Expansion for Spinel is given as 7.45 X 10-6 /°C.

CHAPTER 3 EXPERIMENTAL PROGRAM

Experimental tests were conducted to evaluate the thermal and mechanical properties of molybdenum alloys. Numbers of testing were performed, including three-point-bending testing of notched specimen under different thermal conditions, uniaxial tensile tests under different loading condition and thermal condition, thermal expansion and thermal cycling testing, detailed microstructural analyses before and after these tests. In this chapter, specimen preparation, testing method, testing and facilities and testing procedures were discussed accordingly.

3.1 Three-point-bending tests

Three-point-bending tests were conducted to investigate the fracture toughness at different temperature, detailed crack tip deformation and microstructural analyses were also investigated.

3.1.1 Specimen and preparation

As shown in Table 3.1, two casting molybdenum alloys were studied in this research, (1) Mo (vacuum casting and then annealed 24hr/1600°C/vacuum), (2) MoSi (0.745wt%Si, vacuum casting and then annealed 24hr/1600°C/vacuum). The as-received casting material for each alloy is in cylinder shape, about 12mm in diameter and 55mm in height. Three-point-bending specimens were designed and obtained using wire-EDM cutter.

For each alloy, two specimens were tested under room temperature (26°C) and elevated temperature (550°C). The shape and dimension of four specimens were shown in Figure 3.1 and Table 3.2. Every specimen was polished to obtain mirror surface finish. 600 lines/mm zero thickness grating was made on one side of the specimen which covered the crack tip region [55].

Table 3.1 Material matrix for three-point-bending tests

MATERIALS*	COMPOSITION	PROCESSING CONDITION
Mo (#648)	100% Molybdenum	Annealed 24hr/1600°C/Vaccum
MoSi (#649)	99.255wt% Molybdenum 0.745wt% (2.5at%)Silicon	Annealed 24hr/1600°C/Vaccum

Table 3.2 Dimension of miniature three-point-bending specimens

Material	a (mm)	w (mm)	a/w	B (mm)	Nominal Testing Condition
Mo_1	1.61	9.0	0.18	1.51	26ºC
Mo_2	1.53	9.0	0.17	1.85	550ºC
MoSi_1	1.41	8.0	0.18	1.74	26ºC
MoSi_2	1.34	8.0	0.17	2.33	550ºC

a: crack length, w: specimen width, B: specimen thickness

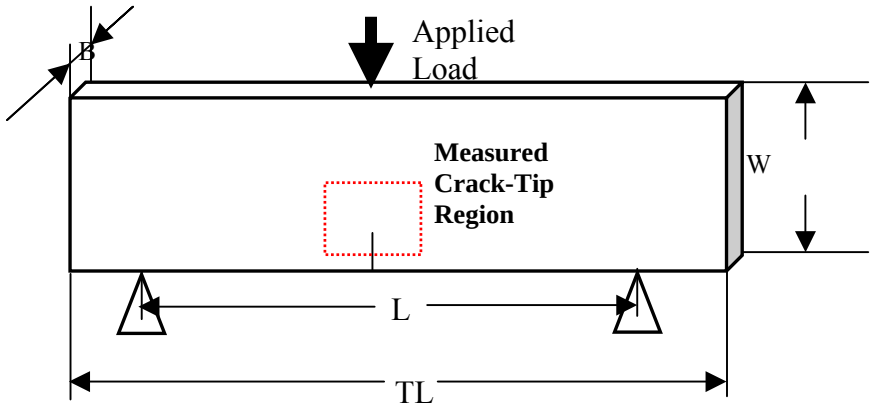

B=2mm, L=40mm, TL = 50mm, W=9mm
Figure 3.1 Notched specimen geometry

3.2.2 Crack tip deformation measurement

Figure 3.2 shows phase-shifting high temperature moiré interferometry for in-plane (u, v) deformation measurement. Phase-shifting technique was introduced using a

liquid crystal variable retarder (LCVR) to improve the spatial resolution and automation [56].

As shown in Figure 3.2(a), an argon ion laser beam with 45-degree linear polarization is split by a polarization beam splitter (PBS) into two beams which have mutually perpendicular polarization direction, P and S. These two beams are shone on the specimen and reflected to the imaging system. As shown in Figure 3.2(b), phase-shifting is introduced in the imaging system as these two beams entering LCVR, which is configured such that the P and S polarization directions are aligned to fast- and slow-axis, respectively. Through the LCVR digital interface controller, phase-shifting is controlled by a PC. A polarizer is placed after the LCVR to view the fringe pattern in the imaging system [56]. A narrow-band filter is used to allow only the argon ion laser line to pass through to the imaging system.

Figure 3.2(c) shows laboratory setup. The sensitivity of current system is 0.8334□m/fringe. Customized loading frame is extended into the environmental/vacuum chamber and connected to a three-point-bending holder. Inside the chamber, a specimen with 600 lines/mm cross-line zero thickness grating is placed on the three-point-bending holder. Both room temperature and high temperature tests were conducted inside the chamber. The high temperature tests were conducted under vacuum condition (<10-5torr) to prevent oxidation on the surface of the specimen.

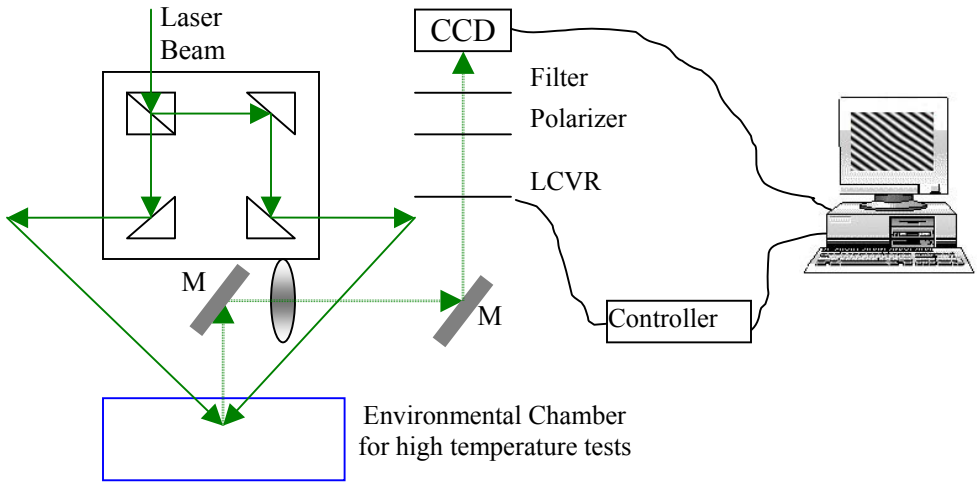

(a) Principle of high temperature moiré interferometry

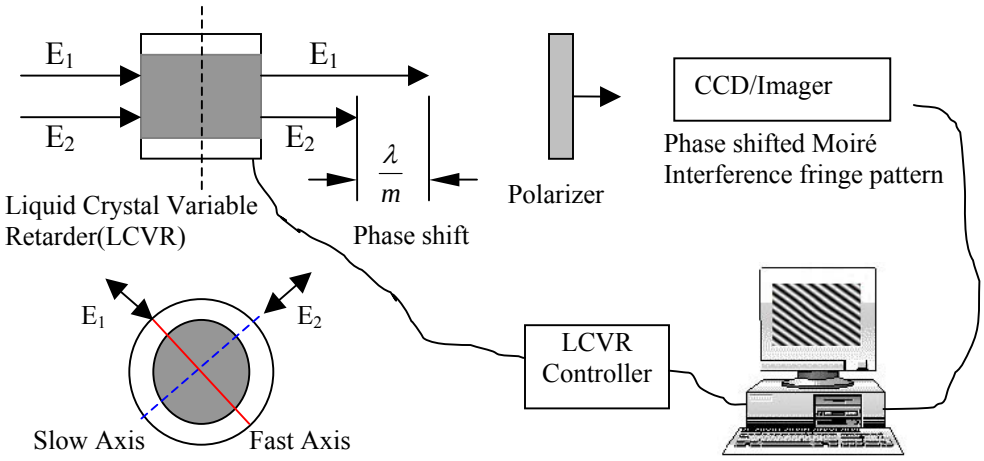

(b) Phase-shifting technique using LCVR

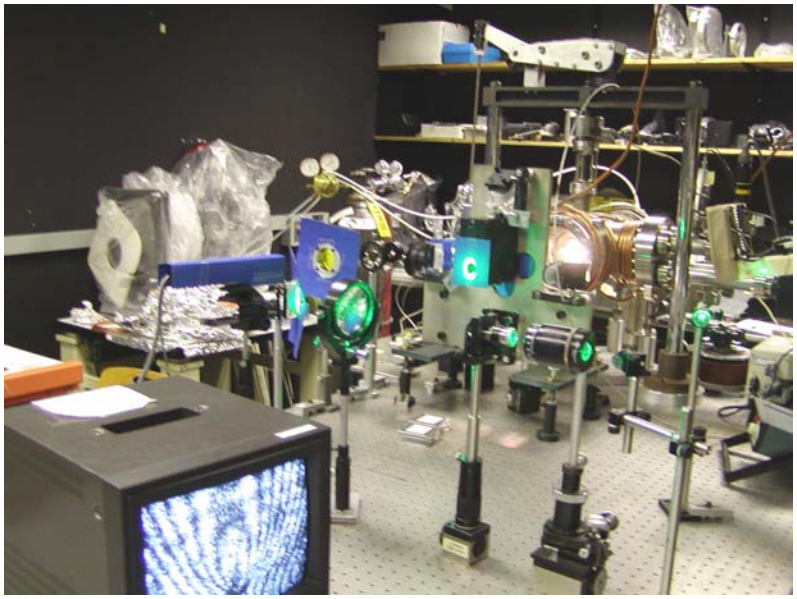

(c) Laboratory setup

Figure 3.2 High temperature moiré interferometry with automatic phase-shifting control

3.2.3 Testing procedures

During tests, all specimens were put into the environmental chamber. At room temperature, after mounting the three-point-bending specimen, load was gradually

applied. At each loading step, crack tip in-plane deformation was recorded using moiré interferometry.

At high temperature, vacuum condition was first achieved. During heating up the specimen, coefficient of thermal expansion (CTE) was measured using moiré interferometry. At room temperature, T_0, carrier fringe pattern was artificially applied. Then temperature was gradually increased in steps. Denser fringe patterns were captured at each corresponding step. The CTE was calculated,

$$\varepsilon_T = \left(\frac{1}{\Delta x_T} - \frac{1}{\Delta x_{T_0}} \right) \cdot \frac{1}{2f} \tag{3-1}$$

$$\alpha(T) = \frac{d\varepsilon_T}{dT} \tag{3-2}$$

Where Δx_{T_0} is carrier fringe spacing at room temperature, Δx_T is fringe spacing at a temperature step (T), and f is grating frequency.

At designated testing temperature (550°C), high temperature moiré system was adjusted so that null fields were obtained. Then load was gradually applied till the specimen failed. Fracture toughness was calculated based on,

$$K_I = \frac{PS}{BW\sqrt{W}} f(\frac{a}{W}) \tag{3-3}$$

$$\text{Where} \quad f(\frac{a}{W}) = \frac{3*\sqrt{\frac{a}{W}}[1.99 - \frac{a}{W}(1-\frac{a}{W})(2.15 - 3.93\frac{a}{W} + 2.7\frac{a^2}{W^2})]}{2(1+\frac{2a}{W})(1-\frac{a}{W})\sqrt{1-\frac{a}{W}}}$$

3.2 Uniaxial tensile tests

3.2.1 Test materials and specimen geometry

Materials used for uniaxial tensile tests are described in Table 3.3. Five sets of molybdenum alloys were examined. The first four alloys were disks with 62 mm diameter and 13 mm height. As shown in Figure 3.3, flat dog-bone configurations approximately 1.8 ~ 1.9 mm thick with a gage length 10 mm were obtained using a wire-

cut EDM machine. For alloys #678, due to the size of the raw material, only bending tests was conducted. To minimize the influence of surface defect, all test specimens were polished down to 1μm surface finish.

3.2.1.1 Material matrix

Table 3.3 Material matrix

NO.	MATERIALS	PROCESSING CONDITION
#695	Mo	Mo powder (2- μm) Hot Pressed/1hr/1800ºC/3ksi/Vacuum
#696	Mo-3wt%$MgAl_2O_4$	Mo powder (2-8μm) 3wt% $MgAl_2O_4$(1~5μ m) Hot Pressed/1hr/1800ºC/3ksi/Vacuum
#697	Mo-6wt%$MgAl_2O_4$	Mo powder (2-8μm) 6wt% $MgAl_2O_4$ (1~5μm) Hot Pressed/1hr/1800ºC/3ksi/Vacuum
#698	Mo-3wt%MgO	Mo powder (AEE, 2-8 μm) 3 wt% MgO Hot Pressed/1hr/1800ºC/3ksi/Vacuum
#678	Mo-3.4wt%$MgAl_2O_4$	Mo powder(2-8μm)3.4 wt%$MgAl_2O_4$(1~5μm) Hot Pressed/4hr/1800ºC/3ksi/Vacuum

3.2.1.2 Specimen design

The specimen design was based on several considerations: (1) to obtain as many specimens as possible and (2) to avoid excessive stress concentration on the specimen.

All tensile specimens were numbered according to the position (1, 2, and 3) and layer (1, 2, 3, 4, 5, and 6). And Z series and R series were used for microstructure checking. Solid carbide drill was used to drill pin holes for these molybdenum alloy tensile specimen.

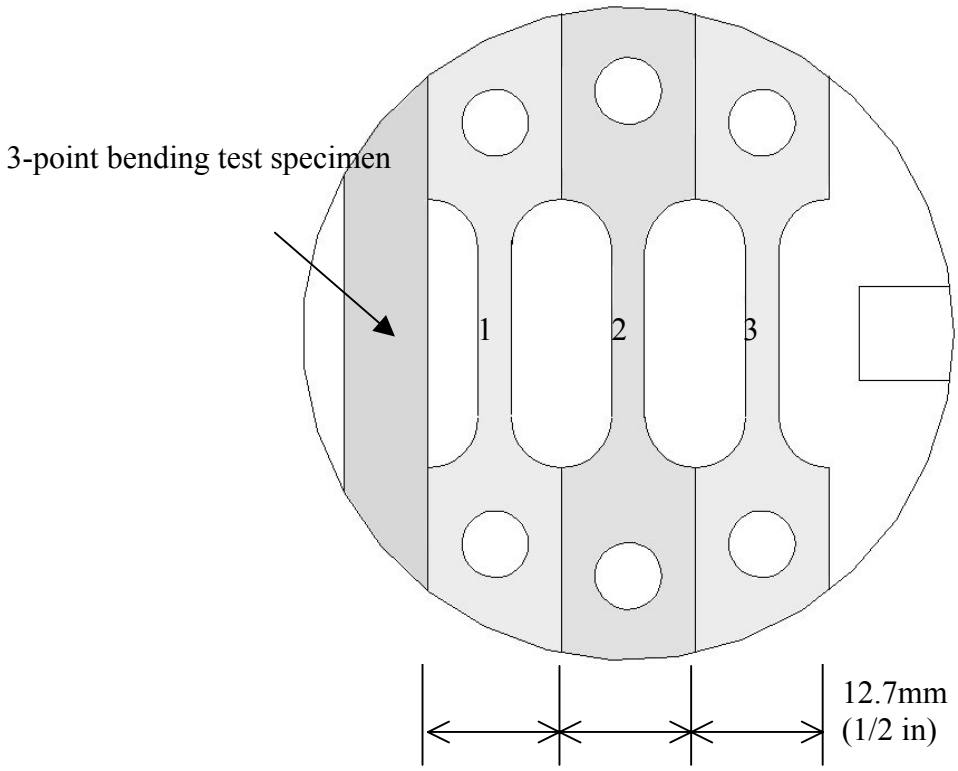

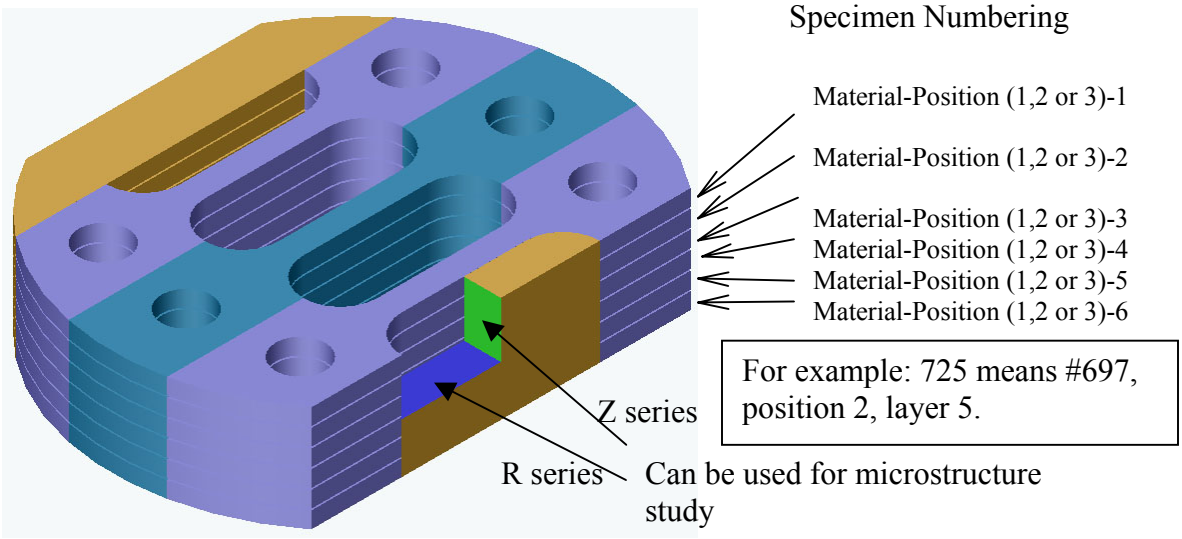

Figure 3.3 Specimen Design

3.2.2 Test equipment

3.2.2.1 MTS 810 system

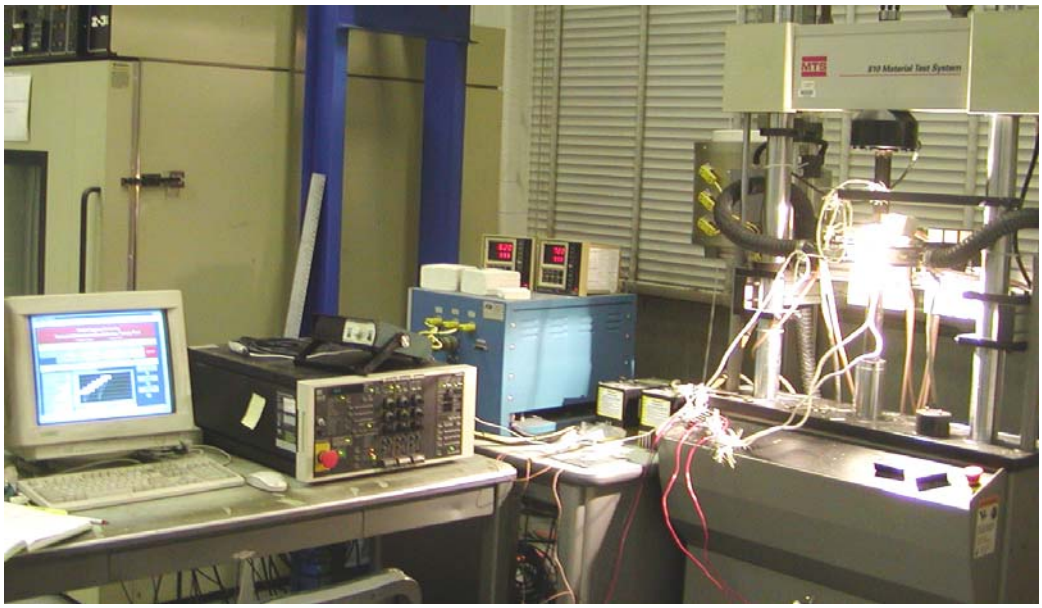

Figure 3.4 MTS 810 System

A MTS 810 material testing system was used to perform the tensile test as shown in Figure 3.4. The system is controlled using a PC-based National Instruments LabView Software. Through MTS MicroConsole, the software will control the MTS system with pre-defined parameters, which including loading/displacement rate, heating rate and temperature. It will also write these parameters and load-cross head movement information to the hard drive for future reference. This MTS is equipped with a quartz heating system, which is designed for high temperature test up to 1200°C. It can perform high and low cycle fatigue tests, tensile, and compression tests.

The customized software was designed in WVU with the original source code obtained from the Air Force Materials Research Laboratory. There are two unique function of this system: (1) crack monitoring system which provides the capabilities of measuring fatigue crack growth rates with constant K control; (2) computer programmable quartz heater system which not only can provide the abilities of measuring

on-cooling thermo-mechanical properties of various cooling paths but also can perform quench cracking test with different cooling rates.

Figure 3.5 show the MTS 810 high temperature setup with extensometer mounted. It consists of a MTS 810 materials test system, a customized quartz heater system (which can be used for high temperature material testing up to 1,200°C), an Epsilon Model 3448 high temperature extensometer and a PC data acquisition system. A customized computer program is used to control the heating, conduct the tensile test, and record the stress-strain curve.

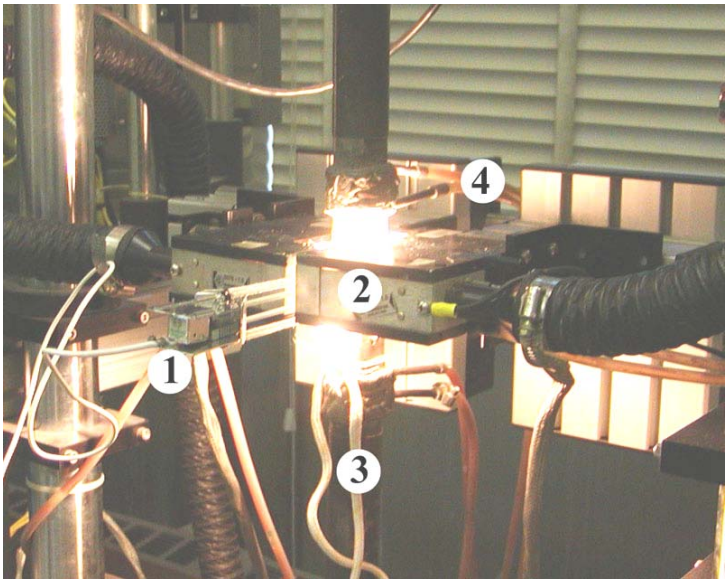

1. High temperature extensometer, 2. Quartz lamp heater with specimen mounted, 3. Thermocouple, 4. Water cooling lines

Figure 3.5 MTS 810 high temperature material testing system

3.2.2.2 High temperature extensometer

As shown in Figure 3.6, an Epsilon model 3448 high temperature 10mm gage length extensometer was used through all the tensile tests. This unit is designed for use up to 1200°C, and could be directly connected to a MTS MicroConsole.

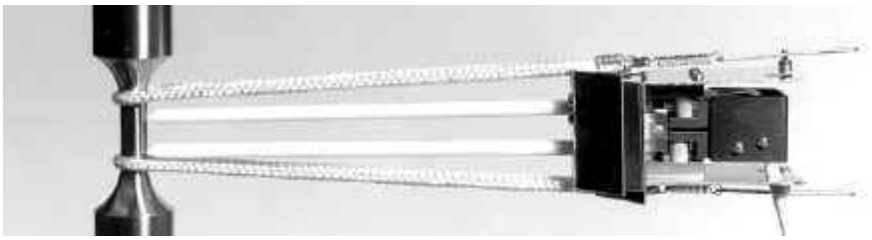

Figure 3.6 Epsilon 3448 high temperature extensometer

The unit is held on the specimen by light, flexible ceramic fiber cords, such that the extensometer is self-supported on the specimen and furnace mounting brackets are not required. It weighs less than 35 grams. The side load on the test sample is mostly eliminated because of the self-supported design and light weight of the extensometer. Material testing furnace with a side cut-out is readily to use this extensometer. It uses high purity alumina (min 99.7%) ceramic rods (Vee chisel or conical contact points).

The combination of radiant heat shields and convection cooling fins allow this model to be used at specimen temperatures up to 1200°C (2200 F) without any cooling. Like other strain gage transducers (load cells, extensometers, etc), this extensometer uses a full Wheatstone bridge design which is excited by 10VDC. This extensometer operates equally in tension and compression. Thus tensile, compression and cyclic tests such as low cycle fatigue can also be done with this unit.

As shown in Figure 3.7, the extensometer has been calibrated in-situ. A calibrator simulates the extension of the real specimen, and a PC with data acquisition (DAQ) system can record the voltage output. The voltage-displacement relation could be established as shown in Figure 3.8.

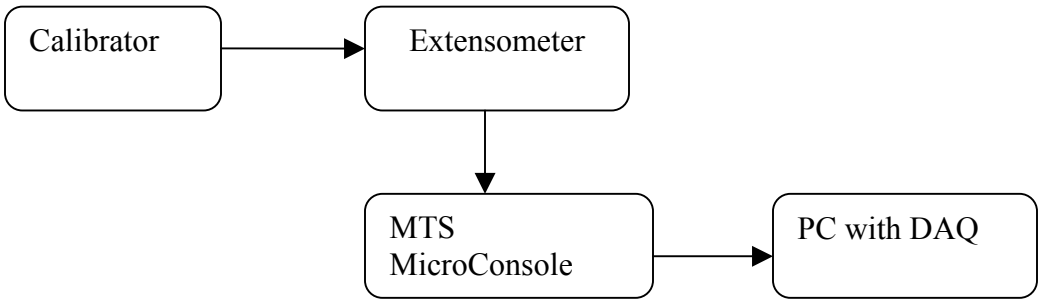

Figure 3.7 Calibration system

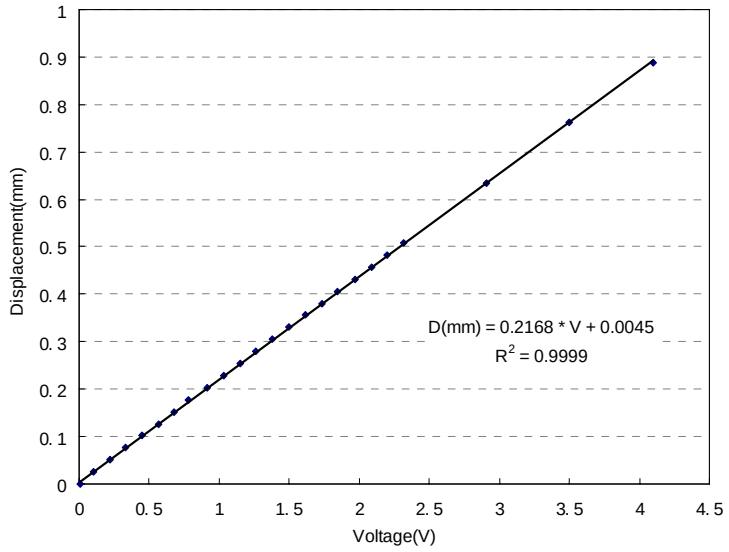

Figure 3.8 Extensometer calibration curve

3.2.2.3 Data acquisition (DAQ) system

Figure 3.9 shows the MTS 810 tensile test system configuration. It also controls the quartz heating unit. Due to the limit input channels of this PC, another PC with RTI 815 12-bit sampling DAQ system was also used to record the stress strain data.

On the main PC, a customized program can set all related testing parameter, including heating if necessary. It can also write the parameters to a file, and write load-cross head displacement to the file, which can be used to estimate the material properties and for later reference.

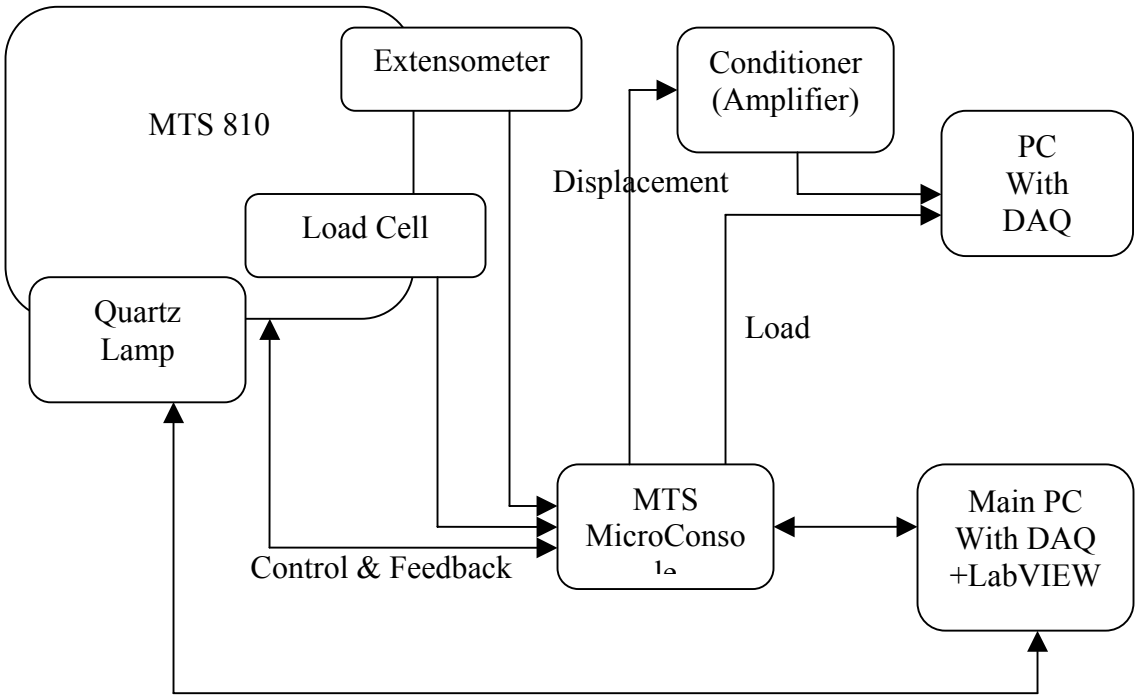

Figure 3.9 MTS 810 Tensile test system configuration

For materials with high Young's modulus value, the MTS 810 test system may not be able to obtain the Young's Modulus value accurately; in this case an amplifier is used to enhance the displacement signal.

3.2.2.4 Scanning Electron Microscope (SEM)

Scanning electron microscope (SEM) was also used to study the material surface morphology. SEM is designed for direct studying of the surfaces of solid objects. SEM uses electrons instead of light to form an image. A beam of electrons is produced by heating of a metallic filament. The electron beam makes its way through electromagnetic lenses which focus and direct the beam down towards the sample. Once it hits the sample, secondary and backscattered electrons are ejected from the sample. An image is formed in much the same way as a TV. A Detector collects the secondary or backscattered electrons and converts them to a signal that is sent to a viewing screen to produce an image [43]. The SEM column and sample must always be at high vacuum when it is in used. The reason for requiring a vacuum in an SEM is that the electron beam

cannot be generated and maintain its high stability. A gases environment would also hinder the transmission of electron beam through the electron optical column.

A JEOL JSM-6400 Scanning electron microscope (SEM) was used throughout this research. This machine offers a wide range of magnification (10X to 300,000X) and high resolution (35Angstroms at 35kV). The cathode is a tungsten hair pin filament. It is also equipped with a EDX system with Si(Li) spectrometer crystal and exchangeable beryllium-thin window configuration for light element detection[44]. The energy dispersive x-ray spectroscopy (EDX) capability of this SEM was used to study the elemental composition. When the electron beam of the SEM bombards a sample, electrons are ejected from the atoms comprising the material's surface. The resulting electron vacancy is filled with an electron from a higher shell, and an x-ray is emitted to balance the energy difference between the two electrons. The energy of these emitted x-rays is characteristic of the elements from which the x-rays were emitted. The EDX detector collects, counts, and sorts the x-rays and displays the results as an EDX spectrum, which is a plot of energy versus the relative counts of the detected x-rays. EDX spectra of the alloy layers and the base materials were taken and compared. EDX spectra were collected for a time of 30 seconds. Elemental mapping of several specimens was also performed. The mapping indicated the distribution and relative concentrations of elements across the sample surface using image brightness intensity [19].

3.2.3 Experimental procedure

3.2.3.1 System calibration

Calibration has been done by two steps, load and displacement. For load calibration, the DAQ computer reads the voltage from the MicroConsole, and the relation between load and voltage could be established as Figure 3.10. For displacement calibration, as discussed earlier, the extensometer is calibrated prior to each test.

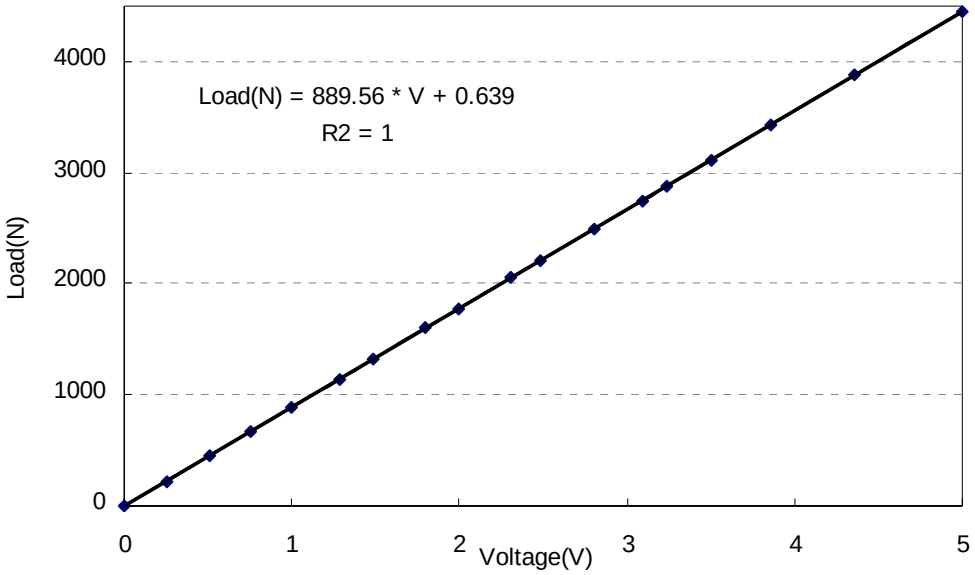

Figure 3.10 MTS Load cell calibration curve

3.2.3.2 Tensile test

The engineering tensile test is widely used to provide basic mechanical properties of the material such as Young's modulus, yield stress etc. An engineering stress-strain curve is constructed from the load-elongation measurements. Ductility is qualitative, subjective property of a material. The conventional measures of ductility that are obtained from the tension test are the engineering strain at fracture (usually called elongation) and the reduction of area at fracture.

Room temperature and high temperature (650°C) tests were conducted in this research work. In order to keep consistency, all the test specimens have the same configuration.

Due to the small dimension of the dog-bone specimen, surface defects may play an important role. To minimize this effect, a mirror-like specimen surface finish (down to 1 μm) was prepared for each test specimen.

To study the loading rate effect, two loading rates, 0.254mm/min and 0.00254mm/min, were use. For each alloy, four tests were conducted. Table 3.4 shows the testing scheme.

Table 3. 4 Tensile Test Scheme

	Room Temperature		650°C	
	0.254mm/min	0.00254mm/min	0.254mm/min	0.00254mm/min
Each Material	X	X	X	X

3.2.3.3 Microstructure evaluation

Proper specimen preparation is essential if the true microstructure is to be observed, identified, documented and measured.

According to the technical information provided by www.buehler.com, for refractory metals, such as molybdenum alloy, we follow their four-step procedure to prepare samples as shown in Table 3.5 Buehler's Ecomet-2 two speed Grinder-polisher with Automet-2 power head was used to prepare the specimen.

Table 3.5 Four Step Preparation for Molybdenum Alloy

Surface	Abrasive/Size	Load Lb. (N) /Specimen	Base Speed (rpm)/Direction	Time (min:sec)
CARBIMET® Abrasive Discs (Waterproof Paper)	320 (P400) grit SiC water cooled	6 (27)	150-250 Comp.	Until Plane
ULTRA-POL™ or ULTRA-PAD™ Cloths	9 um METADI® SUPREME Diamond Suspension*	6 (27)	150-200 Contra	10:00
TRIDENT™ or TEXMET®1000 Cloths	3 um METADI SUPREME Diamond Suspension*	6 (27)	150-200 Contra	8:00
MICROCLOTH®, NANOCLOTH™ or CHEMOMET® Cloths	~0.05um MASTERMET® Colloidal Silica plus attack polish agent**	6 (27)	120-150 Contra	5:00

*Plus METADI® Fluid extender as desired
** See helpful hints for more details
Comp. = Complementary (platen and specimen holder both rotate in the same direction)
Contra = platen and specimen holder rotate in opposite directions

There is a close correlation between material microstructure and mechanical properties of materials. Therefore, it is important to study the microstructure of the test alloys to understand their mechanical properties.

Using optical microscope, colorized grain structure could be revealed clearly. Scanning electron microscope is suitable for higher magnification and fractography studies.

First, use R & Z series, alloys' microstructure was studied. Spinel particle size and distribution were analyzed using backscattered image or optical microscopy.

Secondly, since important information about the nature of fracture can be obtained from microscopic examination of the fracture surface, fractography of post-mortem tensile test specimens was studied to reveal the fracture characteristics.

Thirdly, specimens undergone thermal cycles were analyzed to study the thermal cycle effect to the material microstructure.

3.3 Thermal expansion and thermal cycle tests

Thermal expansion is characterized by the *coefficient of thermal expansion*(CTE). It is defined by the amount of expansion in a unit length of a solid material as a result of a temperature rise of 1 degree (1^o).

$$\text{Coefficient of thermal expansion, } \alpha = dl / l / dT \qquad (3\text{-}4)$$

Where, l is the length, and dT is the temperature change.

Coefficient of thermal expansion, though it may be assumed to be a constant, for most materials, it increases slightly with temperature and changes with any phase change in the material.

The base alloys in this study were pure molybdenum, molybdenum with 0.745 weight percent silicon, molybdenum with 3.4 weight percent of Spinel ($MgAl_2O_4$) and molybdenum with 6% weight percentage of spinel ($MgAl_2O_4$). Table 3.6 shows the material composition and the processing method of the alloys under investigation. The heat treatment was done on the specimens as shown in the table. The test specimens were polished using SiC papers from 240 to 600, step by step.

Table 3.6 Tested materials National Lab

Ref. #	SPECIMEN	MATERIAL COMPOSITION	HEAT TREATMENT/PROCESS
648	PURE MOLYBDENUM	100% Molybdenum	Annealed 24hr/1600^{0}C/Vaccum
649	MOLYSILICIDE	99.255% Wt. Molybdenum 0.745% Wt. Silicon	Annealed 24hr/1600^{0}C/Vaccum
677	PURE MOLYBDENUM	100% Molybdenum	Hot pressed from 2-8μm Mo. Powder. 4hr/1800^{0}C/3Ksi/Vaccum
678	MOLYBDENUM-SP Mo-$MgAl_2O_4$	3.4% Wt. $MgAl_2O_4$ Rest Molybdenum	Hot pressed from 2-8μm Mo. Powder and 1-5μm $MgAl_2O_4$ Powder fused. 4hr/1800^{0}C/3Ksi/Vaccum
697	MOLYBDENUM-SP Mo-$MgAl_2O_4$	6% Wt. $MgAl_2O_4$ Rest Molybdenum	Hot pressed from 2-8μm Mo. Powder and 5μm $MgAl_2O_4$ Powder fused 1hr/1800^{0}C/3Ksi/Vaccum

3.3.1 Tests and testing equipment

The specimens stated above were mainly subjected to thermal tests to evaluate their thermal properties and to compare the composition and processing method. The following tests were conducted.

- Coefficient of thermal expansion test using a *Thermo-Mechanical Analyzer.*
- Thermo cycling test.
- Test for determining the energy transformation pattern using a *Differential Temperature Analyzer.*
- Scanning Electron Microscope (SEM), Energy Dispersive Spectroscopy (EDS) for examining the specimens after the tests.

3.3.2 The Thermo-Mechanical Analyzer (TMA 2940)

3.3.2.1 Introduction

The TMA 2940 is an analytical instrument used to test the physical properties of many different materials. It has two major parts, the TMA module cabinet and TMA assembly. The TMA assembly has various parts which cover the hardware *viz.,* the balance enclosure, the probe assembly, stage, which is interchangeable and supports the sample during measurement, the furnace assembly which surrounds the stage. The furnace also encapsulates the thermocouple. The weight tray, located behind the weight tray door, holds the weights to exert known force on the sample. The module cabinet contains the electronics and software needed to control the module, perform and store experiments and results.

3.3.2.2 Theory of operation

Thermo-mechanical analyzer 2940 is capable of heating or cooling the samples while applying the predetermined force on the material. The specimen is placed on the stage and the quartz probe is placed in contact with the sample, any linear or volumetric changes in dimension are determined at the selected temperature and force.

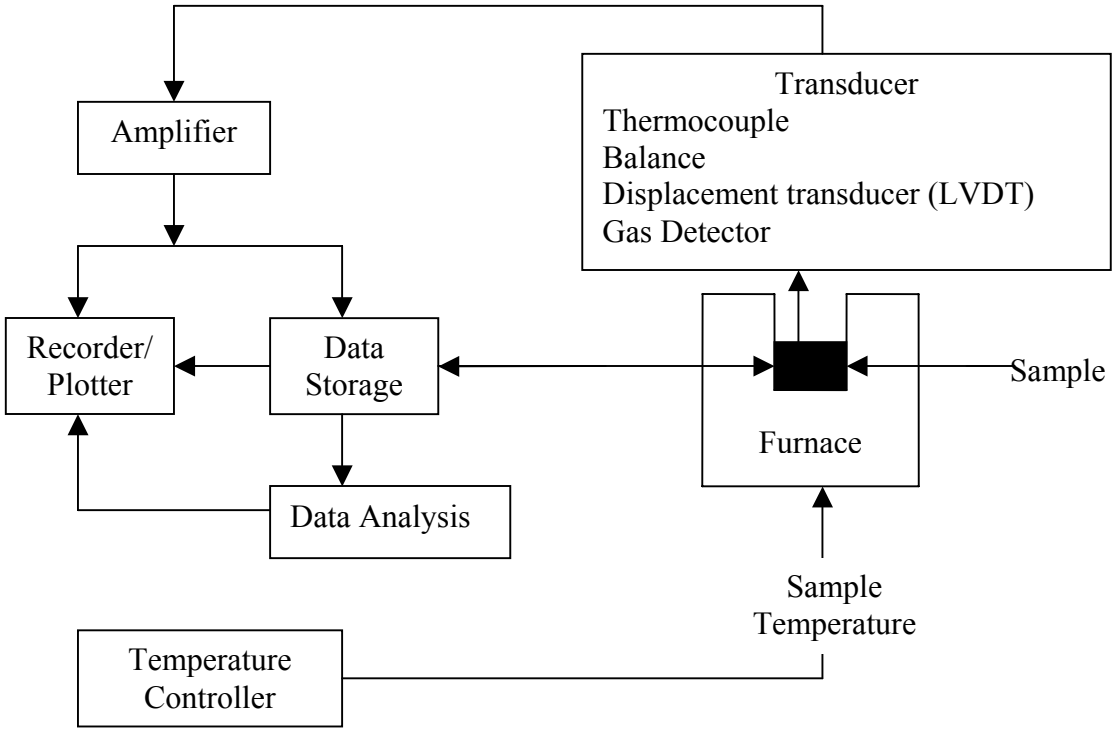

Figure 3.11 Schematic Layout of the TMA 2940

3.3.2.3 Testing procedure

The sample according to the ASTM E831 is to be prepared and polished, so that at least two parallel sides are optically flat. The specimen's flat surface must be placed on the stage and the probe should touch the other side of the specimen. Before placing the specimen the probe must be made to read zero at the start of the test the probe. Once the sample is placed and the probe is made to touch it, the sample's dimension will be measured; this can be done by pressing the "measure" button on the display panel. The initial parameters are automatically fed to the module controller which stores the data in the GPIB. The program must be keyed in according to the requirements for the test. The program will be saved in the GPIB. The thermocouple, which measures the temperature, is placed close to the sample. The furnace must be brought back to the initial place and an inert gas is allowed to pass through the chamber, to ensure an environment, where the process of oxidation is prevented. The experiment is started and the thermocouple reads the furnace temperature and the change in dimensions is sensed by the probe, which is connected to a LVDT. The data will be stored in the GPIB memory for analysis. The controller plots a real time graph and the data's can be analyzed using Universal Analysis® software in the TMA 2940.

3.3.3 The Differential Thermal Analyzer (DTA 1600)

3.3.3.1 Introduction

The Differential Scanning Calorimeter (DSC) is a thermal analysis technique, used to measure the temperature and heat flow associated in materials when there is a phase transition. This analyzer provides qualitative and quantitative information about the materials as a function of time and temperature. Differential Thermal Analyzer (DTA1600) which is mounted on the DSC, measures the difference in temperature between the sample and a thermally inert material as the temperature is increased.

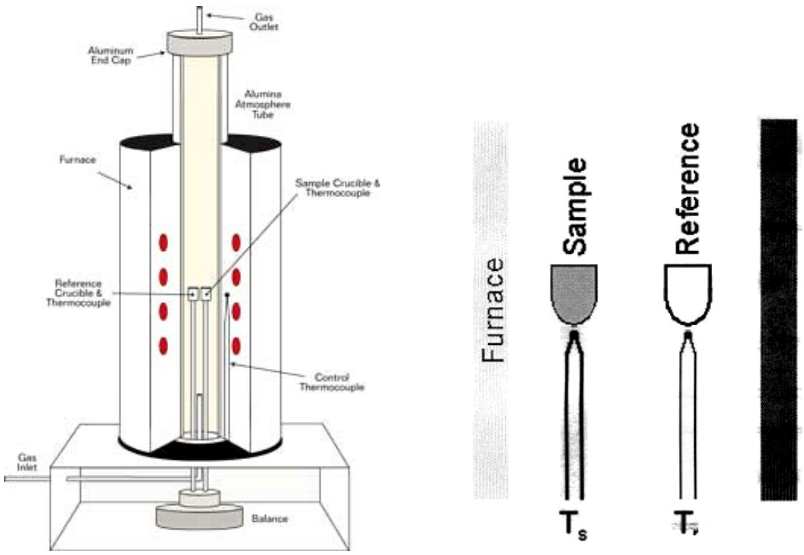

(a) (b)

Figure 3.12 (a) The figure shows the schematic diagram of the DTA furnace and thermocouple assembly. (b) The figure shows the positioning of the thermocouples under the specimen and the reference material.

3.3.3.2 Theory of operation

The DTA has two thermocouples (T/Cs) for measuring the temperature. On the left T/C sits a sample containing cup. On the right is an empty cup. The furnace heats up both cups at the same rate and so Ts-Tr is approximately zero until endothermic (exothermic) transition is reached. At this point energy (heat) is absorbed (released) by the sample and the sample thermometer becomes cooler (warmer). After the sample has completed the transition, Tr and Ts once again become equal. A plot of Ts-Tr versus Tr will show a negative (positive) peak at the temperature transition. The peak height corresponds to the amount of energy absorbed (released) by the sample and the peak width corresponds to the temperature range over which the transition occurred.

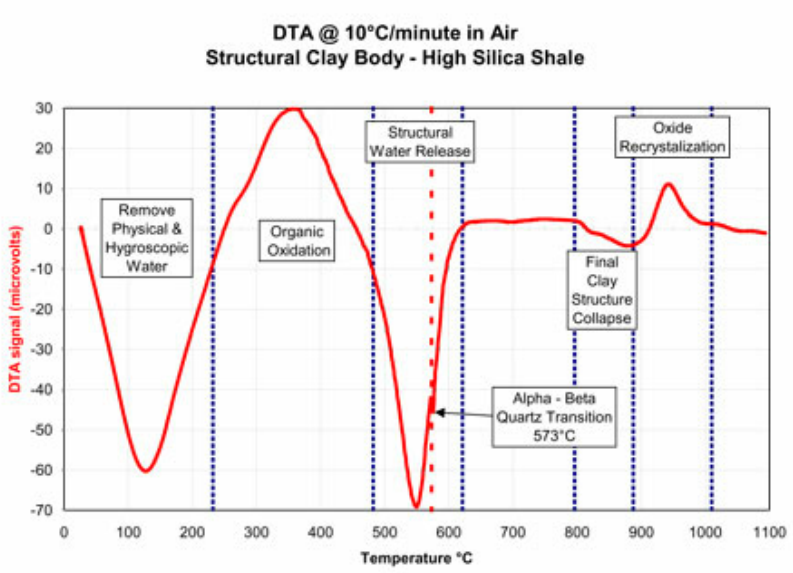

Figure 3.13 Schematic diagram showing typical results from Differential Temperature Analyzer.

3.3.3.3 Testing procedure

The specimen is to be prepared according to ASTM E 473. The specimen is weighed using a balance and it is placed in the reference cup inside the furnace on the right side. The furnace must be closed and the inert gas must be supplied through the furnace tube to maintain a oxidation free environment. The furnace is turned on by using the controller in which the program must be stored in the GPIB, which controls the analyzer. The thermocouple senses the temperature change between the sample and the reference material and the values are stored in the GPIB for the analysis. A real time plot is shown in the display. The data can be analyzed using the Universal Analyzer provided along with the instrument.

3.3.4 Microstructural analysis

The aforementioned JEOL scanning electron microscope was used for the post-mortem of the specimens after the tests to examine the cross-section to study the arrangement of crystals and to check the grain boundaries for any micro-cracks after thermo-cycling tests and to check for any oxides present after the tests. The phase identification in the alloys tested was difficult because of the presence of both light elements and heavy elements. The light elements having low atomic number like silicon, aluminum, oxygen and magnesium, whereas the heavy element having high atomic

number like molybdenum. The X-ray diffraction method was used to identify the phases present in the specimen, for example Mo-$MgAl_2O_4$, once the phases are identified, backscattered electron detector was used to detect the phases present. Backscattering electron detector detects the element by its contrast from the atomic number differences. For example, in this case the material molybdenum- spinel, molybdenum being heavy appears light and the spinel particle being lighter one appears dark. The oxygen, which forms the spinel by mixing with aluminum and magnesium, is not only found in the spinel region but also seen in the molybdenum matrix, which proves the presence of Molybdenum oxide formation at high temperature.

3.3.5 Thermo-cycling test

The alloys #678 and #697, Molybdenum with spinel (3.4% and 6% of $MgAl_2O_4$), in which the size of the molybdenum particle is 2-8μm and $MgAl_2O_4$ particle is 1-5μm, which are subjected to thermo cycling tests to evaluate the cracking pattern due to thermal stresses and expansion at high temperature.

The specimens were placed in a furnace, where the temperature reaches a maximum of 650^{o}C. The heating rate was 200^{o}C/min as shown in Figure 3.14. The specimens were maintained at isothermal once it reached 650^{o}C for 5 minutes [20]. The specimens were air-cooled after that. 3 different specimens were used for 1 cycle, 10 cycles and 20 cycles. After the tests, the specimen's surface was polished using diamond polish suspension till 0.5 micron. Once the test were done and polished, post-mortem of the samples was done using the Scanning Electron Microscope (SEM).

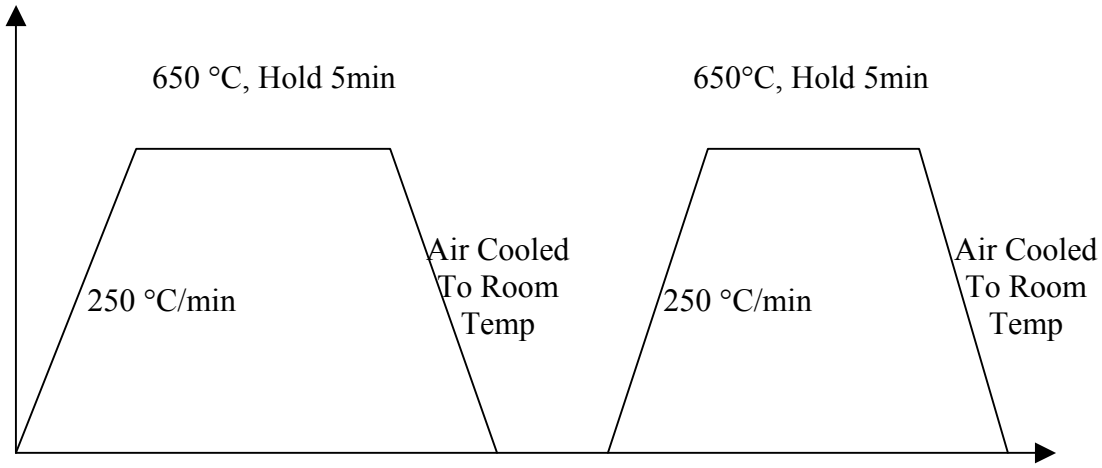

Figure 3.14 Graph showing the thermo-cycle process.

3.4 Microstructural analysis

3.4.1 Tested materials

The test alloys in this study is molybdenum alloys with different weight percentage of spinel ($MgAl_2O_4$) dispersion. Table 3.7 shows the tested materials.

Table 3.7 Tested materials

NO.	MATERIALS	PROCESSING CONDITION
#678	Mo-3.4wt%$MgAl_2O_4$	Mo powder(2-8μm), 3.4 wt%$MgAl_2O_4$(1~5μm) Hot Pressed 3ksi/1800ºC/4hr/Vacuum
#697	Mo-6wt%$MgAl_2O_4$	Mo powder (2-8μm) 6wt% $MgAl_2O_4$ (1~5μm) Hot Pressed 3ksi/1800ºC/1hr/Vacuum
#729	Mo	Mo powder(3~7μm) Hot pressed 3ksi/1800ºC /1hr/vacuum
#730	Mo-5wt%$MgAl_2O_4$	Mo powder(3~7μm), $MgAl_2O_4$, 325mesh Hot pressed 3ksi/1800ºC /1hr/vacuum
#731	Mo-10wt%$MgAl_2O_4$	Mo powder(3~7μm), $MgAl_2O_4$, 325mesh Hot pressed 3ksi/1800ºC /1hr/vacuum
#732	Mo-15wt%$MgAl_2O_4$	Mo powder(3~7μm), $MgAl_2O_4$, 325mesh Hot pressed 3ksi/1800ºC /1hr/vacuum

The specimens were cut into 10mm x 40mm size with thickness approximately 2mm. All the specimens were grinded and polished until 1μm finish to eliminate any

influences of surface defects. Proper sample preparation is crucial to obtain the true microstructure and properties of testing materials. Damage and stress concentration region due to sectioning of sample can also be removed with correct grinding and polishing procedure. The four-step sample preparation procedure described earlier is also adopted in the in-depth microstructural analysis.

3.4.2 Experimental techniques

3.4.2.1 Particle distribution

To evaluate the dispersed particle distribution, a probability function is defined. It normalizes the particle distribution, thus make it easier to compare particle distribution for different alloys. For each particle, square root of the area was used as the characteristic particle size in this research work.

$$P(x) = \frac{Total\_number\_of\_particle\_size \le x}{Total\_number\_of\_particles} \qquad (3\text{-}5)$$

Optical microscope could be used for dispersed particle size and distribution analysis, but due to the grain structure and other distracting information showed in the picture, it is difficult to use computer to automatically do the statistics. A backscattered electron (BSE) image would be much better and easier for particle size and distribution analysis. Figures 3.15 to 3.19 show typical spinel particle size and distribution.

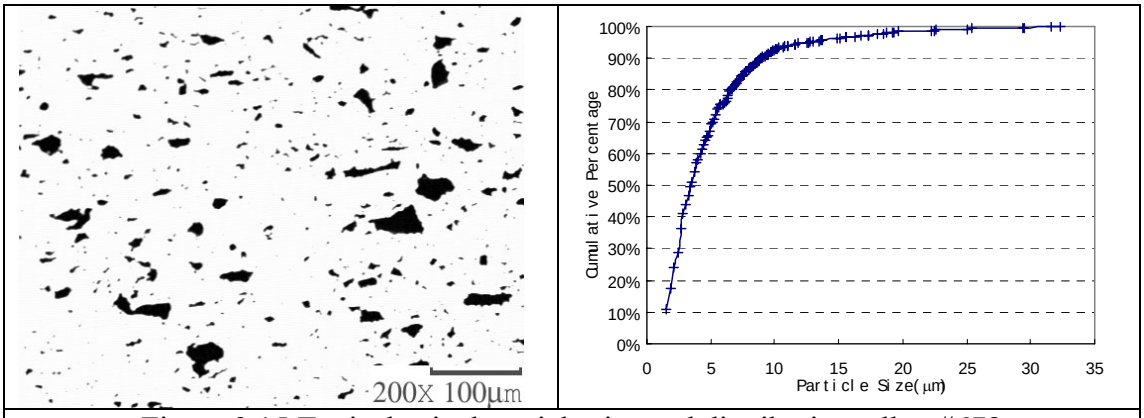

Figure 3.15 Typical spinel particle size and distribution, alloy #678

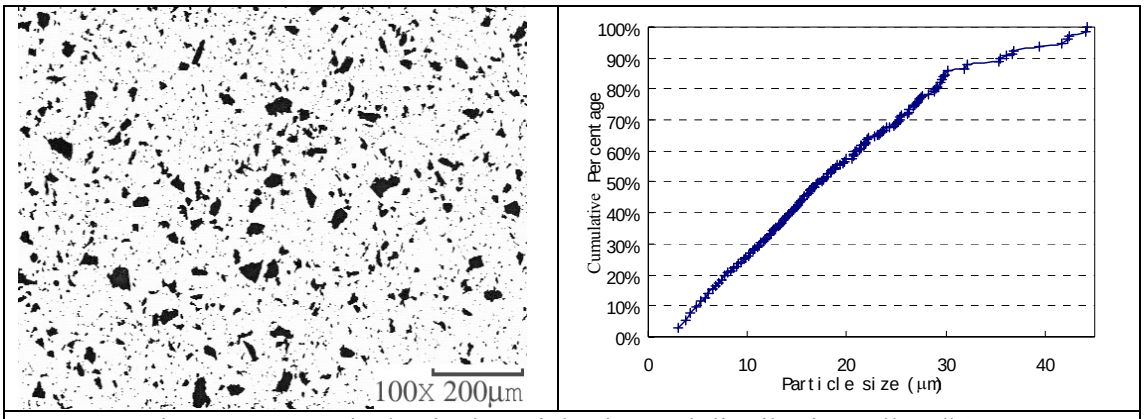

Figure 3.16 Typical spinel particle size and distribution, alloy #697

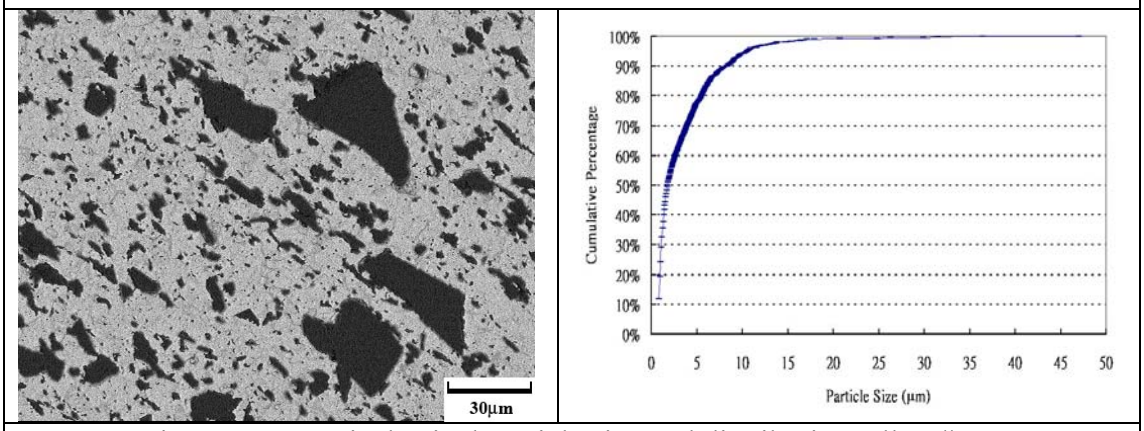

Figure 3.17 Typical spinel particle size and distribution, alloy #732

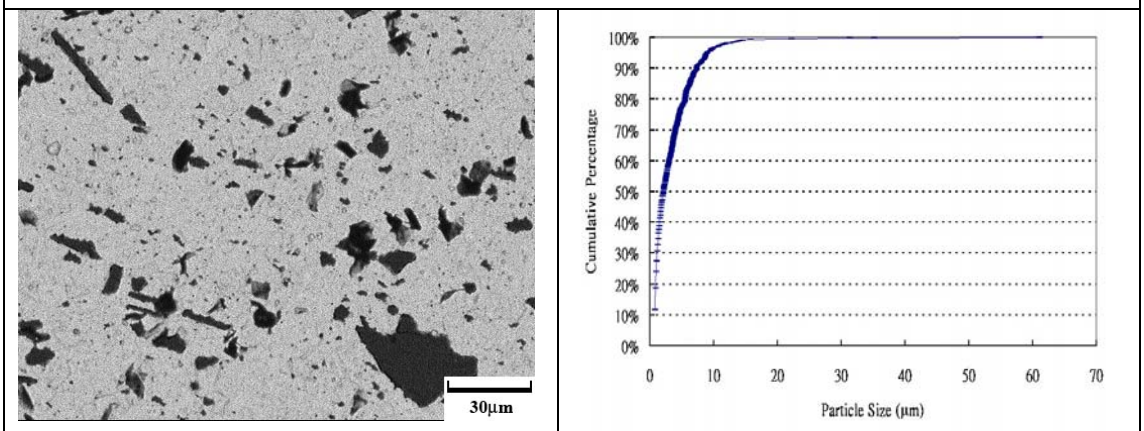

Figure 3.18 Typical spinel particle size and distribution, alloy #730

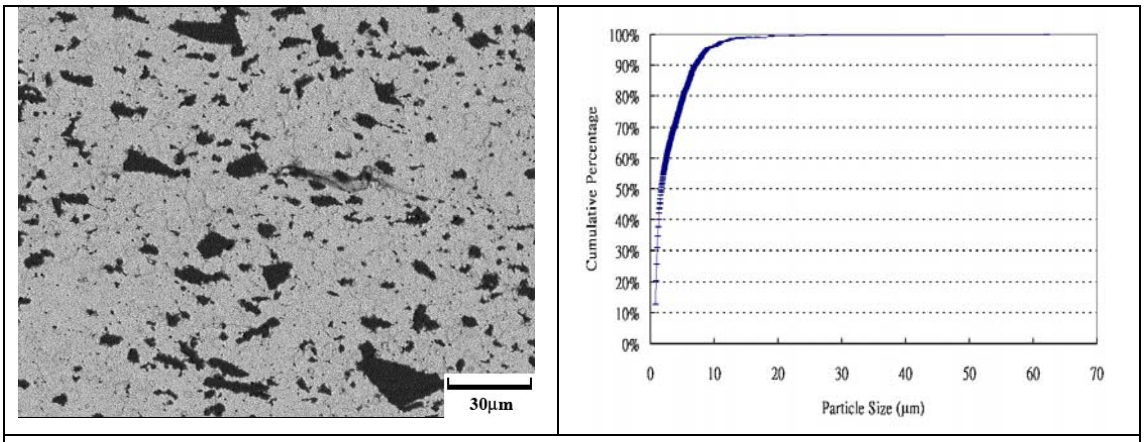

Figure 3.19 Typical spinel particle size and distribution, alloy #731

3.4.2.2 Thermal cycling process

All the test specimens were subjected to thermal cycling tests to evaluate the cracking pattern due to thermal stresses and expansion at high temperature. As described earlier, test specimens were placed in a furnace, where the temperature reaches a maximum of 650°C. The specimens were maintained at isothermal for 5 minutes once it reached 650°C. Specimens were then air-cooled to room temperature. Another set of test specimens were subjected to thermal cycling test at temperature of 1000°C. 20 thermal cycles were performed on 650°C testing condition and five thermal cycles for 1000°C testing condition. The schematic is shown in Figure 3.20. Test specimens were then polished using diamond polish suspension until 1µm finish and carried on with post mortem microstructure analysis.

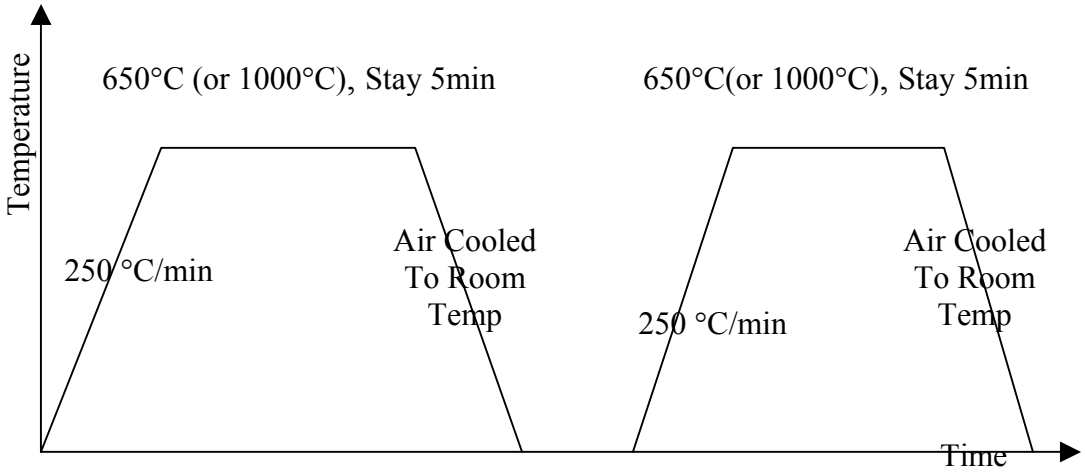

Figure 3.20 Thermal Cycling

3.4.2.3 X-Ray diffraction (XRD)

X-ray crystallography is one of the most useful methods for exploring the nature of matter. X-ray diffractometry (XRD) is used to determine the phase content in many minerals and materials. It complements other mineralogical methods, including optical light microscopy, electron microprobe microscopy, and scanning electron microscopy, in the identification of the constituents of mixtures of crystalline phases, e.g., in minerals, cements and alloys.

To understand X-ray diffraction, one must starts with Bragg's Law. Bragg's Law refers to the simple equation:

$$n\lambda = 2d \sin\theta, \qquad (3\text{-}6)$$

where *d* is the distance between atomic layers in a crystal, the variable lambda λ is the wavelength of the incident X-ray beam, and n is an integer. Bragg's Law is derived by the English physicists Sir W.H. Bragg and his son Sir W.L. Bragg in 1913 to explain the reason for the cleavage faces of crystals to reflect X-ray beams at certain angles of incidence (θ). This observation is an example of X-ray wave interference, commonly known as X-ray diffraction (XRD), and was a direct evidence for the periodic atomic structure of crystals postulated for several centuries [41].

To get a XRD pattern, one takes a sample of the material and places a powdered sample in a holder, then the sample is illuminated with x-rays of a fixed wave-length and the intensity of the reflected radiation is recorded using a goniometer. This data is then analyzed for the reflection angle to calculate the inter-atomic spacing (D value in Angstrom units - 10^{-8} cm). The intensity (I) is measured to discriminate (using I ratios) the various D spacings and the results are compared to the large database from the software used to identify possible matches [42].

Figure 3.21 below shows experimental x-ray diffraction patterns of cubic SiC using synchrotron radiation.

The use of degrees 2-theta in depicting X-ray powder diffraction scans is a matter of convention and can easily be related back to the geometry of the instrument in use.

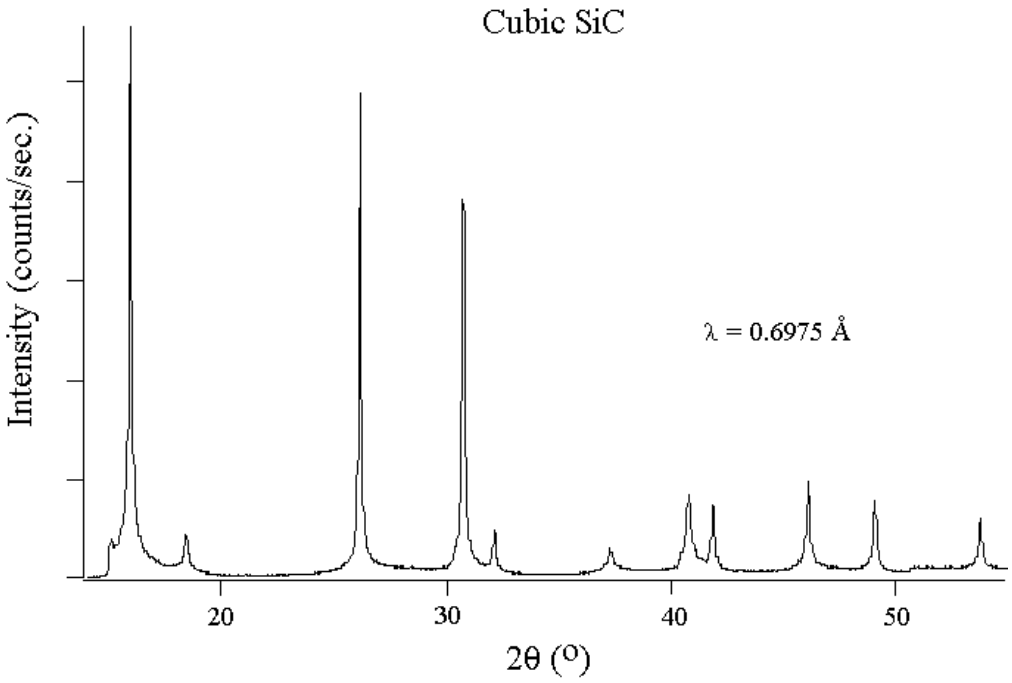

Figure 3.21 Typical X-ray Diffraction pattern

3.4.2.4 SEM and Energy Dispersive X-ray Spectroscopy

As described earlier, SEM was used to examine the detailed microstructure before and after tests. While the energy dispersive X-ray spectroscopy (EDX or EDS) is a method used to determine the energy spectrum of X-ray radiation. It is a standard procedure for identifying and quantifying elemental composition of specimen.

When the sample is bombarded by the electron beam of the SEM, X-rays are generated as a result of the ejection of an inner level electron (low energy) by the energetic electron from an electron column. The ejected electron is replaced by an electron from a higher energy shell. The energy lost as it moves from a high energy shell to a low energy shell is released in the form of X-rays. The energy of the radiation uniquely indicates the element from which it came, hence the term characteristic X-rays. Since atomic structure of each element is different, it follows that each element will emit a different pattern of X-rays [45].

X-ray elemental mapping is a characteristic X-rays intensity map which measured relative to lateral position on the sample surface. It is performed on the test specimen to show the elements distribution.

Quantitative results are readily obtained without standards. The accuracy of standardless quantitative analysis is highly sample-dependent. Greater accuracy is

obtained using known standards with similar structure and composition as the unknown sample [46]. Nevertheless standardless quantitative analysis is still performed by taking advantages that it gives faster results and the specimen geometry and structure is not highly restricted as in the case of standard analysis. Standardless Quantitative Analysis with Phi-Rho-Z method is also performed on the test sample to review the bulk sample element distribution of matrix (Mo), spinel ($MgAl_2O_4$), and Molybdenum oxide (MoO_x).

CHAPTER 4 ASTOMISTIC SIMULATION

A number of molybdenum-based structural materials are currently being developed for ultra-high temperature (>1000^{o}C) applications beyond those presently attainable with nickel-based super-alloys [11,17,21,33,35,59-61]. These materials consist of thermodynamically stable three-phase mixtures of Mo, Mo_3Si and Mo_5SiB_2, and possess attractive combination of high melting point (around 2000^{o}C), good high-temperature oxidation resistance and excellent corrosion resistance in many environments, which makes them of great interest for fossil energy applications.

In the above alloy systems, the oxidation resistance is provided by silicon and boron, which form protective glass scales to prevent further oxidation at medium and high temperatures. The mechanical property is provided by molybdenum through metal phase toughening mechanisms. For purposes of oxidation resistance, it is better to have a relatively small amount of Mo, but this often results in inferior mechanical properties. A fundamental problem, therefore, is that how to maintain the desired mechanical properties while also achieving the required oxidation resistance. It is hoped that through microstructure engineering, such alloy system may possess the right combination of good oxidation and creep resistance together with the necessary fracture toughness and ductility.

Selecting the correct proportions of the three components is important and difficult. It is known that the anisotropy and incompatibility of the thermal expansions of the ternary phase field causes thermal stress and this can lead to microcracking. To tailor the mechanical properties and oxidation resistance within the ternary phase field, it is highly desirable to be able to predict the off-stoichiometry temperature dependence of the thermal expansions of the three components up to very high temperatures. Computer simulations provide a very efficient way to assess the temperature-dependent coefficients of thermal expansion (CTE). In the first section of this article, we report our development of new tight-binding (TB) parameterization scheme for Mo-Si system, and the Monte Carlo (MC) simulation results based on the TB method.

In order to ensure maximum ductility of molybdenum phase it is desirable to inhibit intergranular fracture. Experimental evidence has correlated the intergranular fracture of Mo with the presence of oxygen impurities segregated in the vicinity of Mo grain boundary. It is well known that the grain boundary segregation of impurity elements like oxygen and others can strongly affect the mechanical properties of structural materials, but the detailed fundamental mechanisms depend on specific impurity elements and the hosting material. In the second section, we present our ab-initio studies of various impurity effects on selected high temperature structural materials, including molybdenum and chromium, and analysis of the recent discovered ductility enhancement by metal oxide dispersions, based on electronic structure point of view. Some of these topics are still in progress at the time this report is being prepared.

4.1 Tight binding parameterization of Mo-Si systems and the determination of their thermal expansion coefficients

4.1.1 Introduction

The numerical evaluation of CTEs for certain Mo-Si compounds has previously been attempted by Fu and Wang et.al.[26]. They have obtained interesting and valuable results from first-priciples calculations. By neglecting optical phonon modes and incorporating the Debye model for the acoustic response, their elegant approach involves essentially the evaluation of a few numbers of second and third order energy derivatives with respect to lattice distortion. However, a fundamental limitation is that the Debye temperature for molybdenum, below which the presumption of this approach remains valid, is only about 380^{o}K. At high temperatures typical for fossil energy application, optical phonon modes are significant, and the Debye model is no longer valid. Therefore, alternative techniques must be developed for predicting CTEs at all temperatures.

For this purpose, we decided to use direct Monte Carlo simulation to compute the temperature dependent CTEs. The idea is simple and straightforward: we start identical systems under a set of different temperatures and use the Metropolis algorithm to let the systems evolve. After equilibriums are established, the lattice constants are sampled and averaged to produce the lattice constant vs. temperature curve. The CTEs are then read from the tangential ratios of the curve.

The above scheme will work at any temperature, provided that the method of calculating the total energy is accurate. In addition, we may conveniently predict the effects of variation in stoichiometry and of additives, which is impossible with the previous method.

Nevertheless, computing CTEs via MC simulation still presents a numerical challenge, because the total energy is near its minimum when the lattice constants are sampled. This means that the lattice constant can fluctuate wildly without suffering energy penalties. Therefore, it takes much longer MC steps to converge. With the usual adoption of periodic boundary condition, we also need to have a fairly large system size (a large supercell) to correctly accounts for long wavelength acoustic modes. Thus, we need a reasonably fast and accurate method to evaluate the total energy of a relatively large system.

There are a number of classical potential based methods, including pairwise potential, embedded atom method (EAM), etc., that allow fairly fast determination of total energy for certain systems. However, these methods all suffer from grossly loss of accuracy when applied to transitional metals such as molybdenum. Nor is it clear how the interatomic potentials for different species of elements can be developed to simulate alloy systems.

For these reasons, we chose the tight binding total energy method in our MC simulation. Formulated in the classic work of Slater and Koster half a century ago [62], TB methods have experienced a renewed popularity in recent literatures. In contrast the original method, which was mainly an experimental data interpolation scheme, modern TB methods have been developed to predict electronic structure with accuracy comparable to first-principles electronic methods. The success of TB is due not only to its advantage of theoretical simplicity and numerical efficiency, but also to its real-space approach, which makes it widely applicable to systems that lack perfect crystalline symmetry (e.g., defects, impurities, surfaces and interfaces). Unlike other classical-potential-based empirical methods, TB is based on a quantum mechanical formulation and is therefore more appropriate to explore the quantum nature of chemical bonding properties and to describe complicated materials such as transition metals.

In the past, TB method has achieved considerable success in the modeling of pure elements [63] and many semiconducting alloy systems. However, the deployment of TB in intermetallic alloy systems [64-65] has been very limited, primarily due to the lack of quality TB parameters. The scarcity of TB parameters for intermetallic compound materials is due to a number of difficulties. First, the conventional means to obtain parameters is to fit the TB energy bands to those obtained either from first-principles theoretic calculations or experiment results. The numerical fitting procedure performs the standard nonlinear minimization on the merit function. It works well for single element materials where the number of independent parameters is relatively small. In contrast, a typical binary compound intermetallic material requires over 300 independent parameters. To fit so many parameters simultaneously is prohibitively tedious, and the merit function can easily be trapped into local minima, resulting in unphysical TB parameters that produce energy bands having little resemblance to the original ones. In addition, the validity of the parameters obtained through fitting is usually limited to the same structure or stoichometry as they are originally fitted for, restricting their applicability in MC simulations.

We have implemented a tight-binding parameter extraction scheme which avoids most of the afore-mentioned difficulties, and is particularly suitable for the modeling of intermetallic alloy materials. We will present the details of this scheme, and its application on Mo-Si system using Mo_3Si (crystal structure: A15, see Figure 4.1) as an example, in the following subsections.

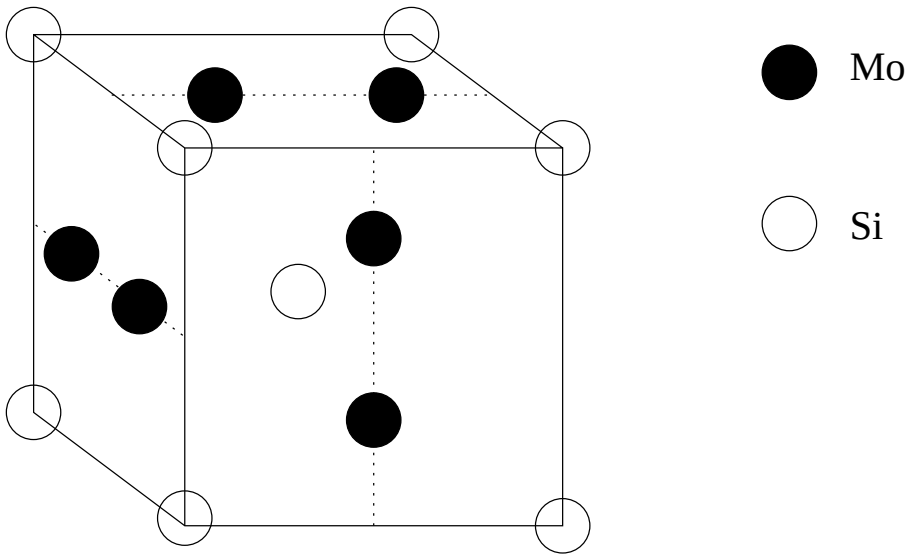

Figure 4.1 The cubic A15 structure for Mo_3Si: The Mo atoms (black circles) form lines bi-secting the cubic surfaces, and Si atoms (white circles) occupy the bcc lattice.

4.1.2 Developing tight-binding parameters for Mo_3Si

We first separate the total energy into TB band energy and a short range repulsive potential:

$$E_{total} = E_{band} + E_{repulsive} \qquad (4\text{-}1)$$

The above separation of total energy involves some arbitrariness. In some TB total energy schemes (notably Papaconstantopoulos [63-65]), the repulsive potential is entirely absorbed by the band energy as a chemical potential shift of the site energies. While this treatment simplifies the problem by reducing the number of parameters to be fitted, it ultimately obscures the physical meaning of each individual component. For example, after this treatment, the TB energy is no longer attractive as normally assumed. For this reason, we keep both terms in our total energy expression. The issue of the energy separation will be addressed later in the procedure of calibration of the band energy.

The Band Energy

In the non-orthogonal TB model, one computes the Hamiltonian and overlap matrices H and S, and solves the generalized eigenproblem:

$$(H - \varepsilon_i S)\psi_i = 0 \qquad (4\text{-}2)$$

The band energy is obtained by summing the energy eigenvalues, weighted by the Fermi function,

$$E_{band} = 2\sum \varepsilon_i f(\varepsilon_i) \qquad (4\text{-}3)$$

Slater and Koster used the two center approximation to express the Hamiltonian and overlap matrix elements as linear combinations of a set of parameters known as SK parameters [62]. For example, an intersite ($R \neq 0$) Hamiltonian or overlap matrix element may be written as (here we used the McMahan's convention [66])

$$\left\langle 0lm \mid H \mid \vec{R}l'm' \right\rangle = \sum_{\mu} g_{\mu}(lm, l'm', \hat{R}) t_{ll'\mu}(R) \qquad (4\text{-}4)$$

and

$$\left\langle 0lm \mid S \mid \vec{R}l'm' \right\rangle = \sum_{\mu} g_{\mu}(lm, l'm', \hat{R}) s_{ll'\mu}(R) \qquad (4\text{-}5)$$

where g_{μ}s are the linear coefficients that depend on the geometric alignment of the participating atomic orbitals, and $t_{ll'\mu}$s and $s_{ll'\mu}$s are the Hamiltonian and overlap SK parameters that depend only upon the scalar intersite distance *R*.

The inverse problem, namely to determine SK parameters from given Hamiltonian and overlap matrices, has been studied by McMahan and Klepeis [66]. They found an orthogonality relationship between the g_{μ}s that can be used to invert Eq.(4-4) and Eq.(4-5):

$$t_{ll'\mu}(R) = \frac{1}{2-\delta_{\mu\sigma}} \sum_{m,m'} g_{\mu}(lm, l'm', \hat{R}) \left\langle 0lm \mid H \mid \vec{R}l'm' \right\rangle \qquad (4\text{-}6)$$

$$s_{ll'\mu}(R) = \frac{1}{2-\delta_{\mu\sigma}} \sum_{m,m'} g_{\mu}(lm, l'm', \hat{R}) \left\langle 0lm \mid S \mid \vec{R}l'm' \right\rangle \qquad (4\text{-}7)$$

Thus, the procedure of obtaining intersite SK parameters is made straightforward: We first compute the k-space Hamiltonian and overlap matrices for the material using our accurate FP-LMTO [67] method. The matrices are then anti Fourier transformed into the real space. The steps have been discribed in detail by Djajaputra [68]. Using Eq.(4-6) and Eq.(4-7), the intersite TB parameters for a particular structure are thus obtained.

The crucial difference between this procedure and conventional schemes through parameter fitting is the following. Conventional schemes start with the total energy and

band structure, which are essentially the ***eigenvalues*** of the generalized Hamiltonian and overlap matrices. One then proceeds to probe the TB parameter space for the set that will generate these eigenvalues. From a mathematics point of view, more than one TB parameter set can result in the same set of eigenvalues (and hence the same band structure and total energy), therefore the numerical fitting result will generally be none unique. In contrast, our ab-initio based parameter retrieving scheme starts directly from the ***matrix elements*** themselves (rather than their derived eigenvalues). The subsequent problem of inverting these matrix elements to obtain their corresponding TB parameter set, under the usual assumption of two-center approximations, is mathematically well defined, and the solution is guaranteed to be unique. Thus, by avoiding working with eigenvalues and choosing to work with physically more informative matrix elements, we can eliminate the uncertainties inherited from numerical fitting procedures, and also avoid some of the common pitfalls inherited from numerical minimization procedures, such as producing unphysical parameters corresponding to local minima.

We note in passing that the idea of obtaining TB parameters directly from first-principles calculation actually dates back to Andersen and his co-workers [69], and has been continued by other groups [70]. The application to intermetallic alloy materials has been performed by Djajaputra for NiAl [68], where the Hamiltonian matrix elements were used as input to real-space calculation of the local density of states using the recursion method. Reported here is an extension to his work in that we further extract the two-center SK parameters, incorporate a repulsive potential to form a representation of the total energy, and subsequently apply it in MC simulation to compute CTEs.

When relating the intersite parameters prepared for different lattice structures (or even for the same structure, but with different lattice volumes, or lattice constants), some caution must be taken. This is because the SK parameterization implicitly assumes that the TB orbitals of the underlying basis remain fixed in all cases. However, in our FP-LMTO calculation, which searches for the optimal basis that minimizes the density functional, a fixed basis is usually not possible. In our practice, we find that if the change of first neighbor intersite distance is less than 10%, and if the muffin-tin (MT) radius parameter is kept fixed in all FP-LMTO calculations, the output basis set remains relatively fixed. This can be seen from Figure 4.2, where the overlap SK parameters *s(R)*

computed from a series of different volumes for Mo_3Si collapse into a common curve. We note in passing that the authors in Ref.1 did not use fixed basis to obtain overlap parameters. Instead, they performed an explicit unitary rotation transformation on the TB orbital basis to ensure a fixed set of overlap parameters. In their case, the issues of transferability were entirely relegated to the Hamiltonian parameters.

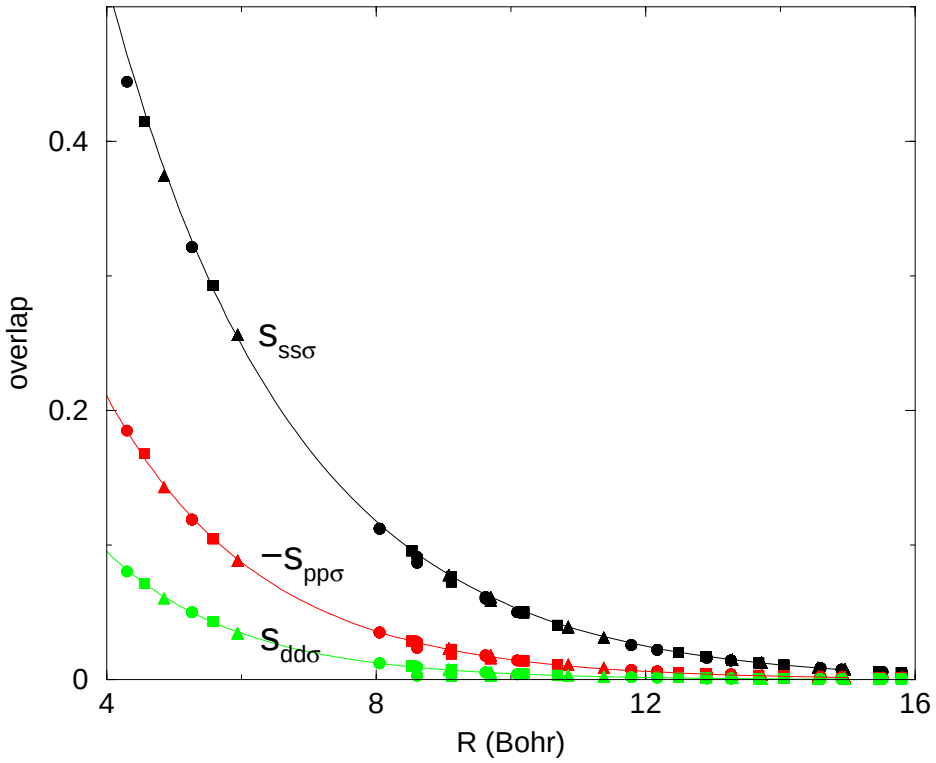

Figure 4.2: The overlap intersite parameters *s(R)* obtained at various lattice constants: circles *a*=8.608 Bohr, squares *a*=9.121 Bohr, and triangles *a*=9.707 Bohr.

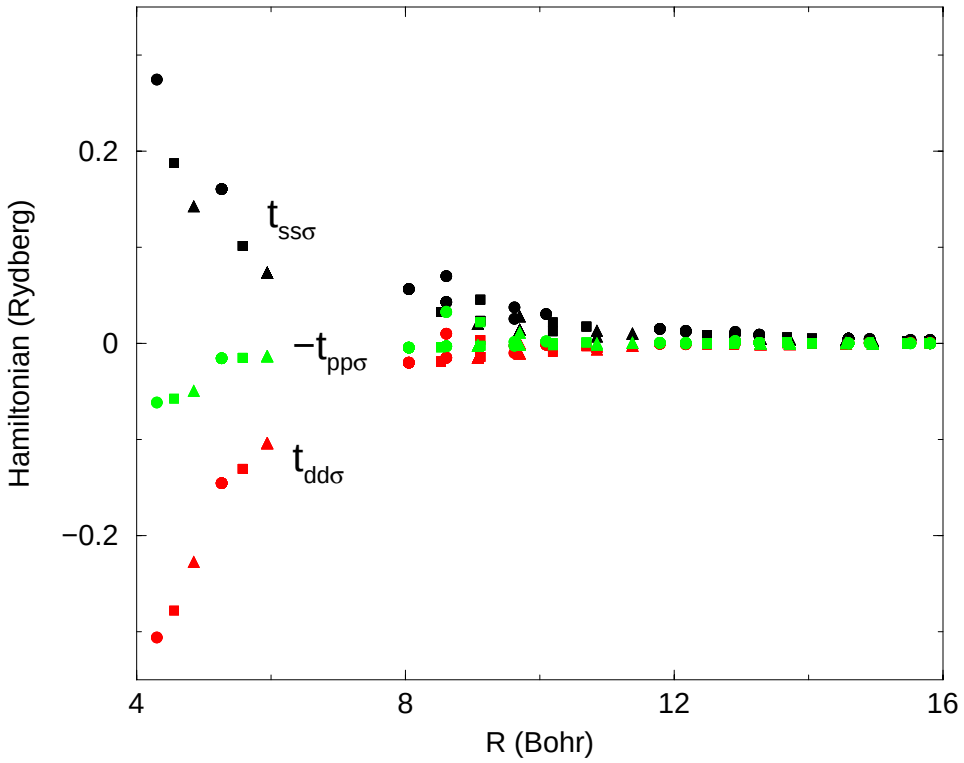

Figure 4.3: The Hamiltonian intersite parameters *t(R)* obtained at various lattice constants: circles *a*=8.608 Bohr, squares *a*=9.121 Bohr, and triangles *a*=9.707 Bohr.

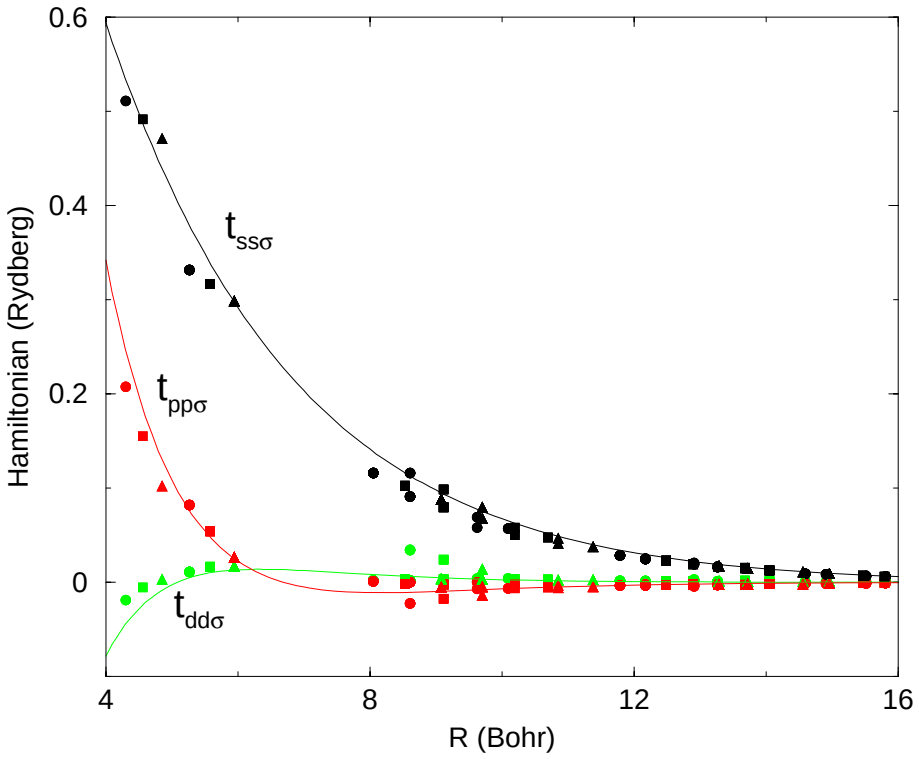

Figure 4.4: The calibrated Hamiltonian intersite parameters *t(R)* obtained at various lattice constants: circles *a*=8.608 Bohr, squares *a*=9.121 Bohr, and triangles *a*=9.707 Bohr.

In contrast to the overlap parameters, Hamiltonian parameters similarly obtained at different lattice volumes show noticeable disagreement (see Figure 4.3). Similar problems have been encountered in many other TB implementations, and sometimes schemes of environment-dependent TB parameters [71] have been used to resolve the discrepancy. Rather than resorting to those complicated schemes, we follow a procedure based on our belief that the arbitrariness involved in the separation of total energy into valence eigenvalue sum and remaining part in the FP-LMTO method is the primary cause to the disgreement of Hamiltonian parameters. Therefore, we performed energy caliberation of the Hamiltonian matrix (i.e., making the FP-LMTO band energy comparable for all lattice volumes) before extracting TB parameters. Within the FP-LMTO results, the lowest energy level of core electron (ε_{1s}) at each lattice volume has been chozen as the reference to measure TB band energy, because it is most unlikely to be affected by the variation of bonding environments. After the recalibration $t(R) \to t(R) - \varepsilon_{1s} s(R)$, the new Hamiltonian parameters are plotted in Figure 4.4, where the improved agreement over Figure 4.3 is apparent.

As a final step, we fit the overlap and calibrated Hamiltonian SK parameters into the following functional form:

$$t(R) = (a_0 + a_1 R)\exp(-a_2 R). \qquad (4\text{-}8)$$

Resulting SK parameters are available upon request.

We now turn to the on-site (*R=0*) matrix elements. The on-site overlap matrix is simply unity if the TB orbitals are properly orthonormalised. For the on-site Hamiltonian matrix, we assume that the off-diagonal mixing produced by crystal field potentials is negligibly small (which is often the case in a cubic crystal environment). Thus the remaining problem is to determine each of the diagonal Hamiltonian matrix elements, which is the site energy of the corresponding orbital plus crystal-field corrections. In contrast to the case of intersite SK parameters, neither the site energy nor the crystal-field correction can be directly extracted from the FP-LMTO results. It was found in Ref.[17] that certain sums of these parameters remain directly computable without fitting. However, these sums are structure dependent, i.e., none transferable. To obtain a

transferable set of TB on-site parameters, we used an alternative scheme described as follows.

First, we assume that the crystal-fields are just the superposition of a mesh of delta functions situated at each atomic site. Thus the crystal-field corrections are particularly easy to evaluate, and the resulting diagonal matrix elements now take the form:

$$e_{lm} = e_l^0 + \sum_{R \neq 0} h \,|\, \psi_{lm}(\vec{R}) \,|^2 \qquad (4\text{-}9)$$

Here e_l^0 is the site energy, h is the coefficient of the delta functions, or the strength of the crystal-fields, and $\psi(\vec{R})$ is the wavefunction of the orbital. The summation is carried out over all other atomic sites. For R sufficiently larger than the MT radius, we can replace $\psi(\vec{R})$ with its asymptotic behavior. It is parameterized in the following Gaussian form:

$$|\, \psi_{lm}(\vec{R}) \,|^2 = b_0 \exp[-(R - b_1)^2 / b_2^2] \,|\, Y_m^l(\hat{R}) \,|^2 \qquad (4\text{-}10)$$

In this form, orbitals that differ only in magnetic number share a common radial part. This enables us to significantly reduce the number of parameters in the fitting while still retaining the correct angular dependence of these orbitals. The fitting is individually performed for each angular momentum number. This fitting is to be contrasted to the conventional fitting scheme in that we are fitting parameters directly to the diagonal Hamiltonian matrix elements one at a time, rather than to the entire eigenvalue set and band structures. Therefore the results are expected to be uniquely defined within the functional form assumption.

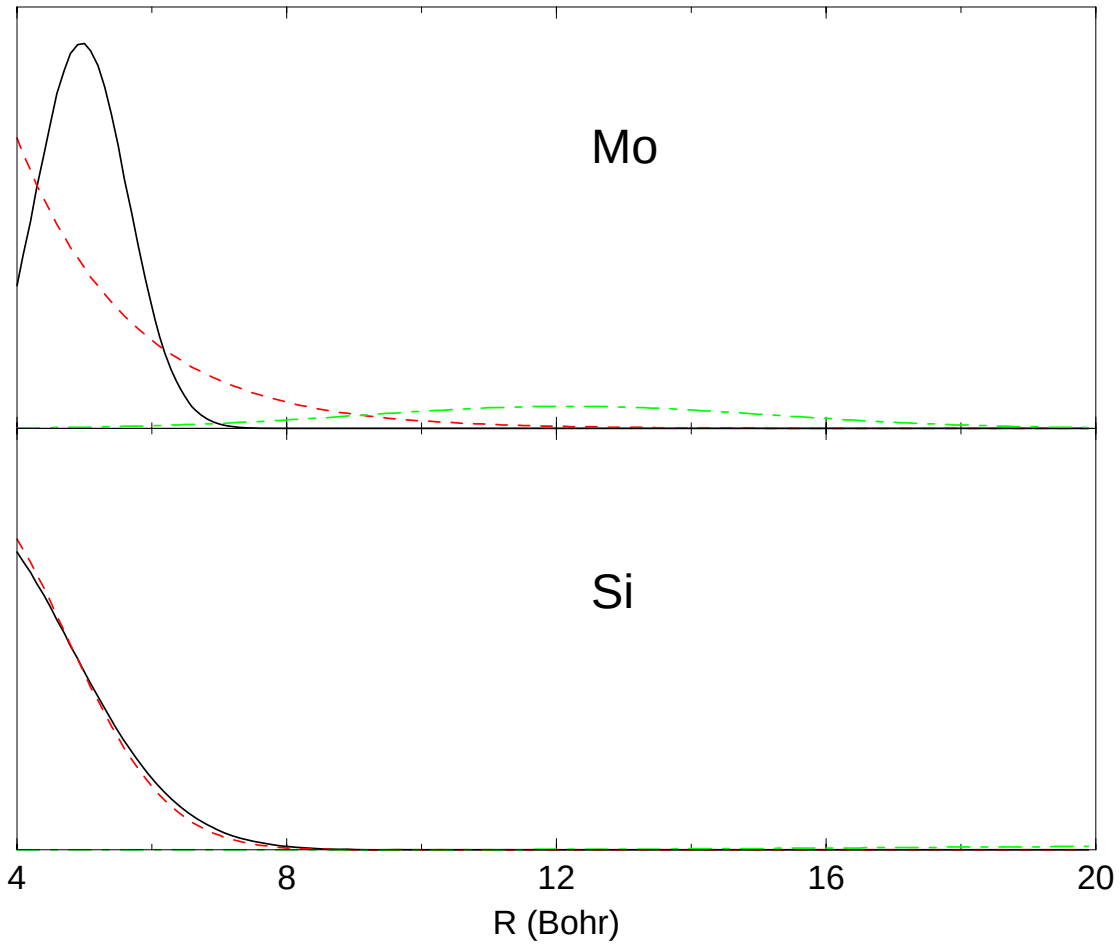

Figure 4.5: The radial distribution of each orbital for Mo (upper panel) and Si (lower panel). In the upper panel, solid: *5s*, dash: *4p*, and dot-dash: *4d*; in the lower panel, solid: *3s*, dash: *3p*, and dot-dash: *3d*.

The fitted radial shapes of each orbital are shown in Figure 4.5. Notice the radial shapes of Si's *3s* and *3p* orbitals are quite similar, indicating a tendency for *sp*-hybridization. The *d* orbitals in the figure are quite small because they are relatively more localized. A few remarks are in order: First, in practice we use the set of real combinations of Y_m^l s that has cubic symmetry. Second, the calibration of energy reference mentioned earlier is of crucial importance for successful fitting of on-site parameters. To see this, we point out that Eq.(4-9) requires that the volume dependence of e_{lm} vanish at large interatomic distance (i.e., at large lattice volumes). Without appropriate calibration, the diagonal Hamiltonian matrix elements computed at different lattice volumes may not be comparable due to the arbitrary shift in energy reference point. This difference usually does not vanish even at large lattice volumes. Therefore, the

successful fitting of on-site TB parameters can be used as an indication of good energy calibration.

The Repulsive Potential

The TB band energy is, as it should be, purely attractive. To explain the bonding behavior, we need a repulsive contribution to the total energy that accounts for the ion-ion repulsions and a correction for the overcounting of the electron-electron interactions.

We implement the repulsive potential in an EAM scheme [72], where the repulsive energy is a sum of embedding energies that depend on the local electron densities at each atomic site:

$$E_{repulsive} = \sum_{R} f(\rho(\vec{R})) \qquad (4\text{-}11)$$

The form of the embedding function f is unknown, and is determined by fitting. The electron density ρ at site R is taken to be a linear superposition of first-principles computed electron densities of corresponding isolated atoms:

$$\rho(\vec{R}) = \sum_{R' \neq R} \rho^{0}(\alpha \mid \vec{R}' - \vec{R} \mid) \qquad (4\text{-}12)$$

Figure 4.6 shows the spherically averaged electron densities for free Mo and Si atoms.

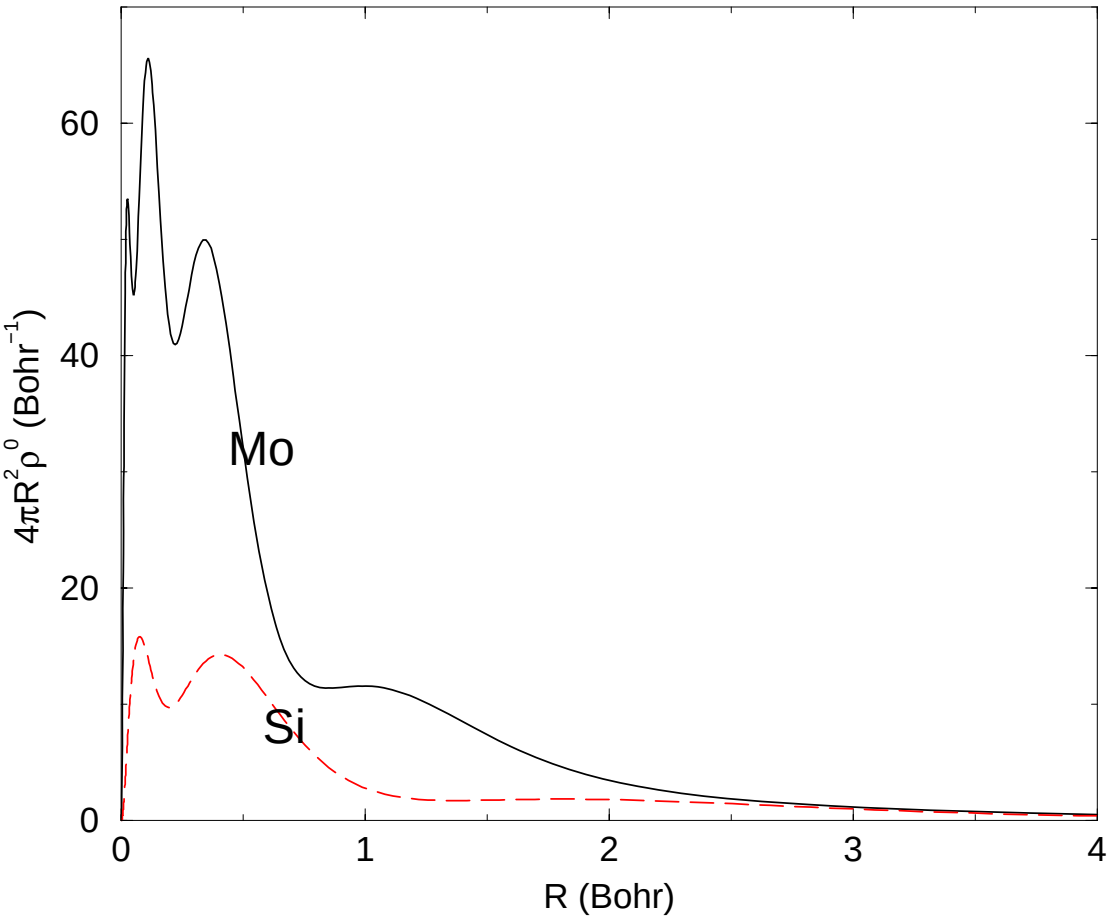

Figure 4.6: Spherically averaged electron density (multiplied by distance square) for free Mo (solid line) and Si (dashed line) atom.

The linear superposition of atomic densities may be quite different from the true density in the crystal. However, according to the density functional theory, the error should be of higher order. On the other hand, we find that the use of pure superposition of atomic densities yields a repulsive contribution that is often too short ranged. Therefore we introduce a scaling factor α for interatomic distance in Eq.(4-12), and find $\alpha = 0.74$ gives the best results. The need of a longer ranged density tail may be explained by the presence of the long range ion-ion Coulomb repusion.

Once the local densities at all sites are available, we fit the embedding function f in Eq.(4-11) to a piece-wise third order polynomial function. The left hand side of Eq.(4-11) is taken to be the difference between the total energy obtained by FP-LMTO method, and the TB band energy, computed using our SK parameters obtained earlier. The database consists of uniform contractions and expansions of the lattice about the

equilibrium volume. In the FP-LMTO calculation, we treat the *4p* semicore electrons of Mo as valence electrons in a separate energy window (to be distinguished from *5p* electrons), and use three-kappa linked basis to describe each valence orbital to achieve results of optimum accuracy. The resulting embedding function is shown in Figure 4.7. In the present work, we find a common embedding function for Mo and Si suffices for our purposes.

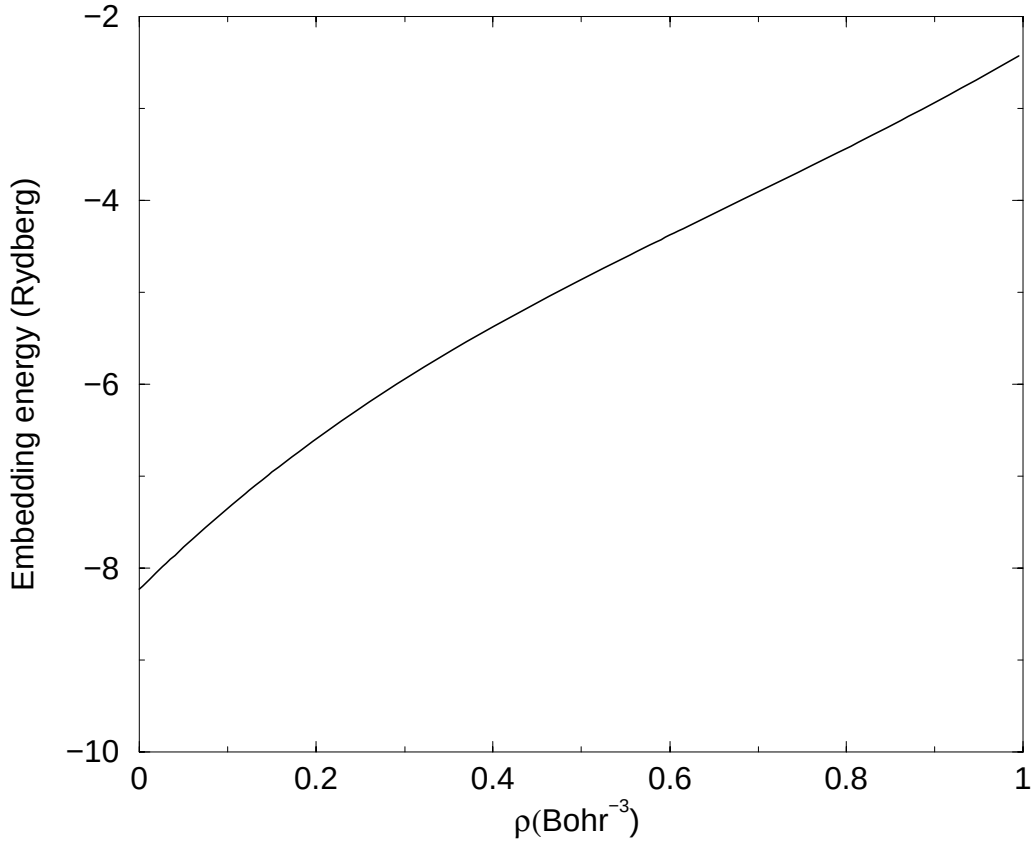

Figure 4.7: The embedding function for Mo_3Si.

4.1.3 Tests of TB parameters

The transferability and accuracy of obtained parameters were tested against ab-initio results. In this subsection, we discuss various tests on our parameters for their accuracy and transferability.

Accuracy Tests

In order to see how well our TB total energy scheme can reproduce the results of

accurate FP-LMTO calculations, we try both methods to compute the total energies of various deformed lattice structures. The deformations we consider fall into two categories. The first class of deformations are those used to obtain various elastic constants. They are intimately related to the acoustic excitations of the crystal. For a cubic structure, the following three types of deformations are normally used to evaluate elastic modules [73]:

- Type I (*orthorhombic*): expanding in the x and y directions by γ, while compressing in the z direction by $(1+\gamma)^{-2}-1$, so that the volume is conserved;
- Type II (*uniform expansion*): expanding in all directions by γ;
- Type III (*monoclinic*): squeezing the angle between x and y axis by γ while keeping the base area and height intact to conserve the volume.

Of these three types of deformations, type II deformation is already within our fitting database.

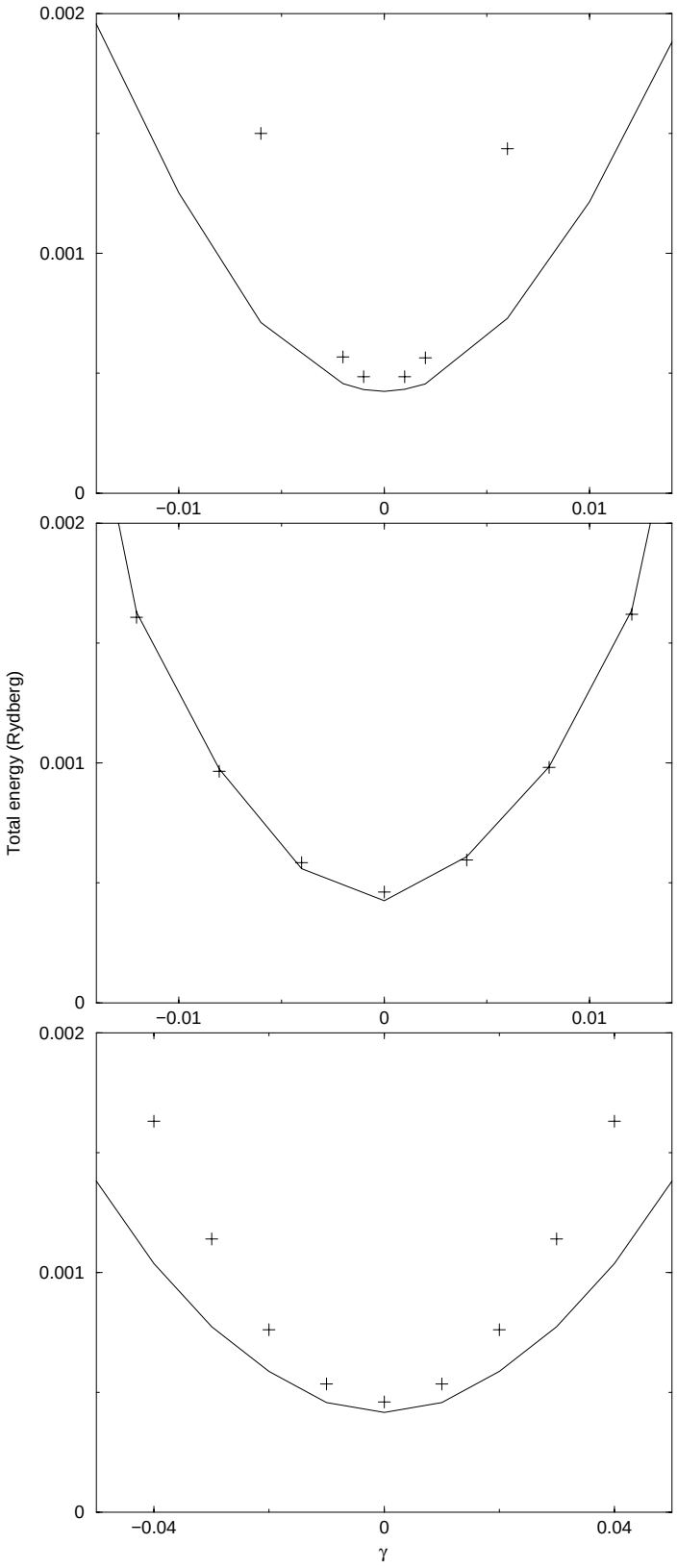

Figure 4.8: The comparison of FP-LMTO results (solid line) and TB total energy results (pluses) under three types of elastic deformations. Upper panel: type I orthorhombic

strain; middle panel: type II uniform expansion or contraction; lower panel: type III monoclinic strain.

Figure 4.8 shows the comparison of the results obtained by both methods for all three deformation types. For type I deformation, there is a large discrepancy between our TB method and FP-LMTO method. We believe the discrepancy mainly originates from the simple assumption of direct superposition of the atomic densities. Had these densities been allowed to relax according to the orthorhombic strain, i.e., the decay rates of atomic density in *x* and *y* directions are slower than that in *z* direction, the total energy should decrease as predicted by FP-LMTO. This relaxation effect will not be present in the remaining two types of deformations, namely type II and III, where the strains are more isotropic. Therefore, in those cases we see a better agreement between the two methods.

In the second class of distortions, which is more related to optical vibration modes of the lattice, we keep the unit cell fixed while displacing atoms away from their equilibrium positions. More specifically, we increase (or decrease) the distance between the nearest neighbor pairs of Mo atoms by γ. This deformation preserves maximum crystal symmetry in favor of our FP-LMTO calculations. The results, showing good agreement between the two methods, are shown in Figure 4.9.

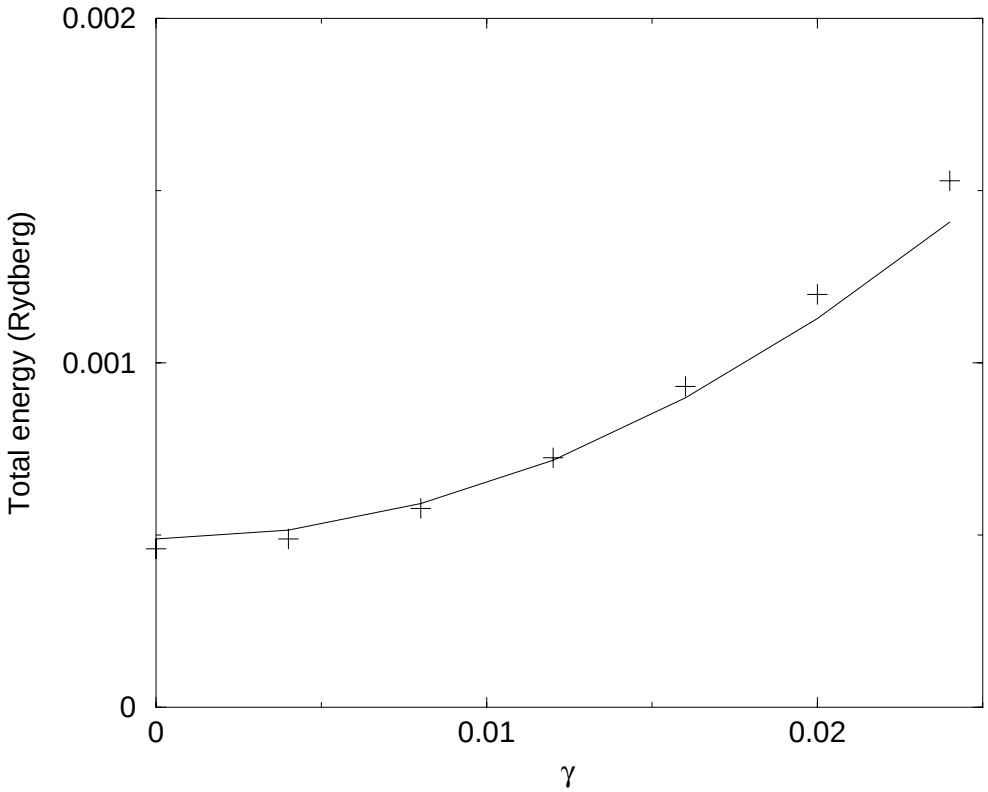

Figure 4.9: The comparison of FP-LMTO results (plus signs) and TB total energy results (solid line) under anti-phase Mo-Mo deformation.

Transferability Tests

For the purpose of simulating a dynamic process or calculating a finite temperature property, it is demanded that the parameters be transferable. Since we did not distinguish the element type in the repulsive part of the total energy, we shall limit our discussion to that of the TB band energy part.

The transferability of the intersite SK parameters for Mo_3Si over certain ranges of volumes and deformations around the cubic A15 structure has been discussed in our accuracy tests. Here we focus on the transferability with variations of structure and stoichiometry. For this purpose, we independently develop another set of intersite SK parameters for Mo in body centered cubic (b.c.c.) pure Mo and for Si in cubic diamond (c.d.) pure Si. The comparison of the two sets of SK parameters for Mo and for Si is shown in Figure 4.10 and 4.11, respectively. We see generally good agreement in Mo parameters. However, there are significant discrepancies in Si parameters. Considering the much greater difference in the atomic environment (the equilibrium nearest Si-Si distance is about 0.42nm in Mo_3Si while about 0.23nm in c.d. Si, a change about 46%),

the result is reasonable. We thus conclude that good transferability is limited to cases where the change in nearest neighbor distance is less than 10%. Typical thermal expansions in solid certainly meet this criterion.

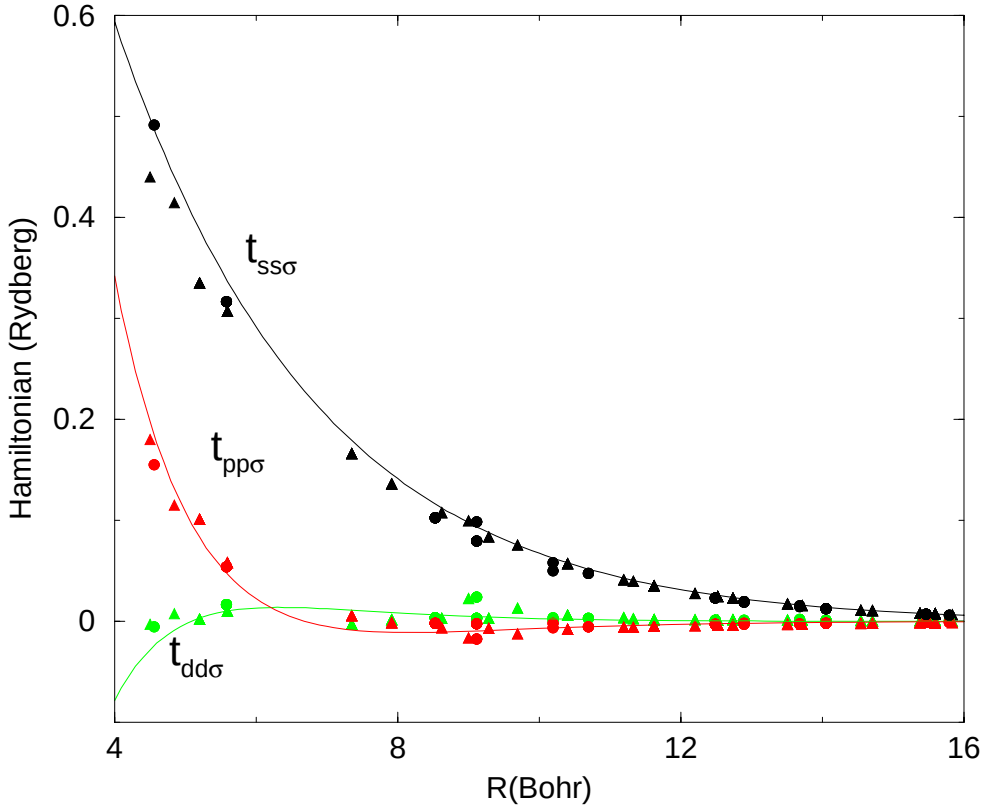

Figure 4.10: The comparison of two sets of parameters for Mo. The circles are obtained for A15 Mo_3Si, and the triangles are obtained for b.c.c. Mo.

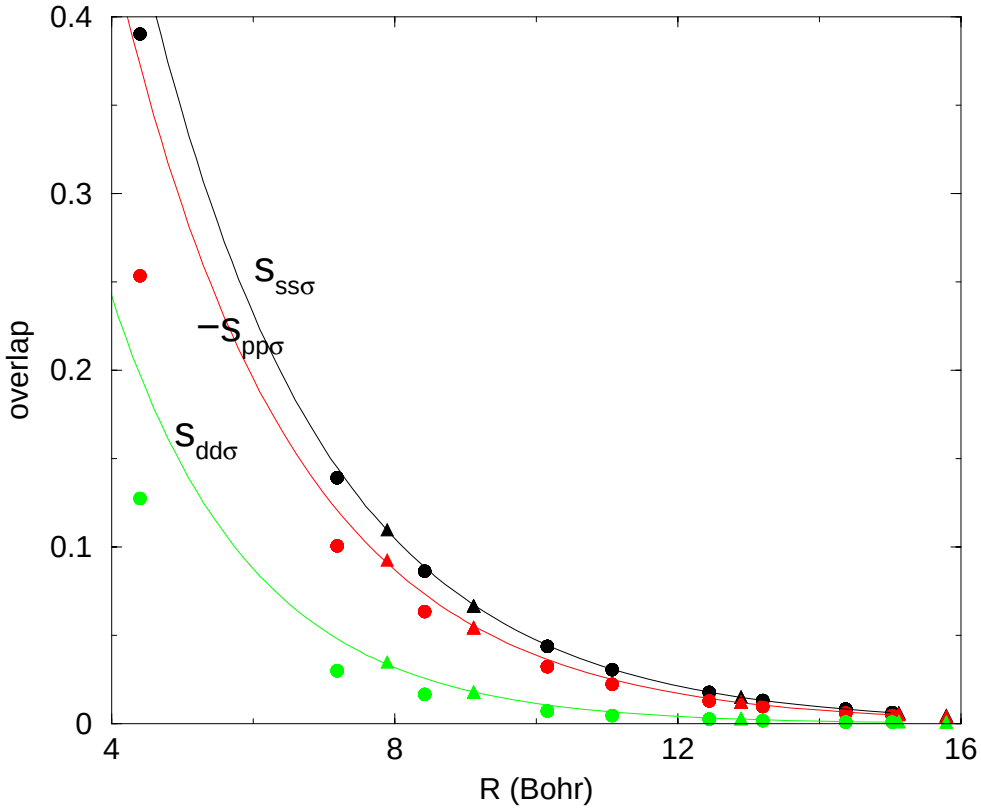

Figure 4.11: The comparison of two sets of parameters for Si. The circles are obtained for A15 Mo_3Si, and the triangles are obtained for c.d. Si.

4.1.4 Monte Carlo simulation

In this subsection, we discuss MC simulation based on the TB total energy method we have developed. Our goal is to predict CTEs for Mo_3Si at various elevated temperatures.

The system simulated consists of 216 atoms ($3\times3\times3$ supercell). We start 13 systems at temperatures ranging from 1200K through 2000K, incremented by 100K. At each MC step, we attempt to either displace a randomly chosen atom's position or change the lattice constant. After 10,000 MC steps, when all systems have achieved thermal equilibrium, lattice constants are sampled at every 20 MC steps. 500 samples are then averaged and their temperature dependence is plotted in Figure 4.12. For the specified temperature range, the material displays a fairly linear thermal expansion. The CTEs can be easily read off from the figure, which is roughly about $9.0\times10^{-6}/^{o}K$. We are unaware of any experimental data for Mo_3Si existing at this time.

To relate our theoretical work with experimental results, we have also simulated a

$Mo_{53}Si$ system (i.e., one out of 54 Mo atoms in a b.c.c. Mo is replaced by a Si atom), using the same set of parameters. Figure 4.13 shows the sampled average lattice constants at 8 different temperature points. The data are compared with the experiment measurements, which were performed on a $Mo_{39}Si$ alloy (containing 2.5 at.% of Si). Our theoretic prediction of CTE for $Mo_{53}Si$ is about $5.0\times10^{-6}/^{o}K$, while the experimental CTE for $Mo_{39}Si$ is about $6.5\times10^{-6}/^{o}K$. Comparing to the published CTE result for pure Mo, which is $4.8\times10^{-6}/^{o}K$, we thus predict the trend that Si-rich compound yields larger CTE. Considering the error range associated with a typical electronic method, the agreement of our theoretical prediction and experiment work is satisfactory.

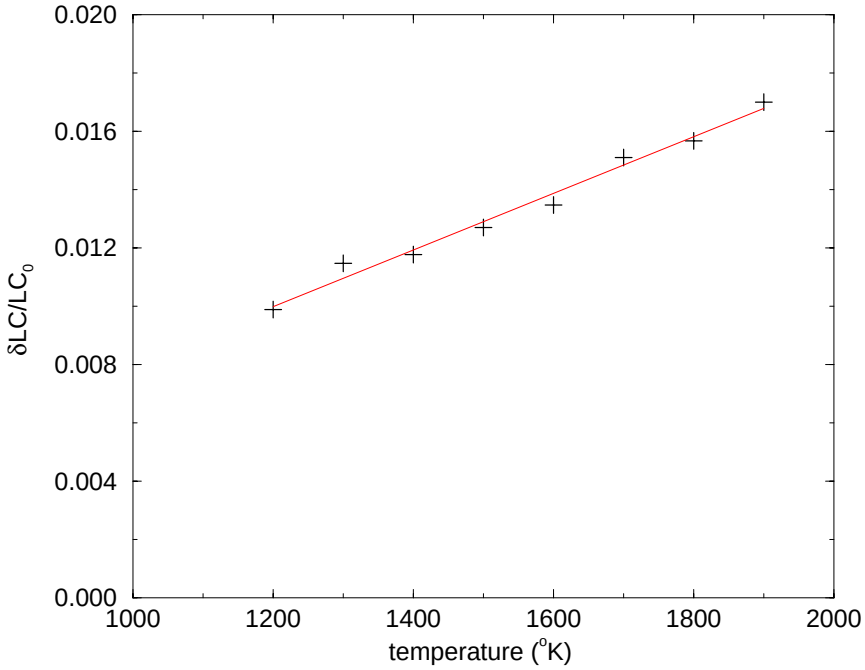

Figure 4.12: The averaged change in lattice constants for Mo_3Si at 13 temperature points. Data obtained from MC simulation.

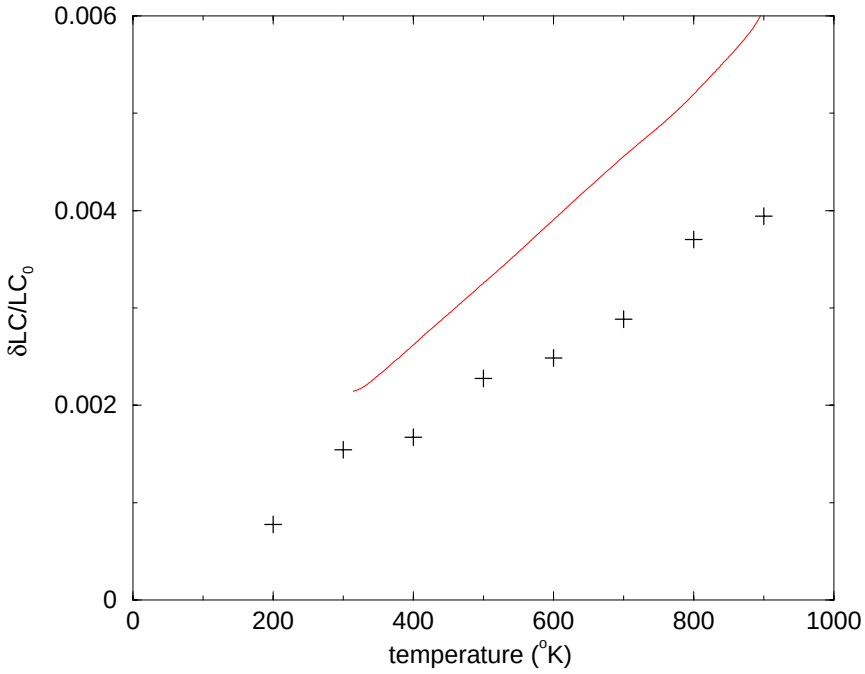

Figure 4.13: Pluses: the averaged change in lattice constant for $Mo_{53}Si$ at various temperature points, data obtained by MC simulation; solid curve: change of linear size for $Mo_{39}Si$, data obtained from experiments.

4.1.5 Summary

We have modified McMahan's scheme of obtaining TB parameters directly from FP-LMTO calculations, and developed a set of TB parameters for Mo-Si systems. The major difficulties of the fitting procedures are thus avoided. We find that additional calibration of energy is crucial in improving the transferability of these parameters. Using a simplifying assumption about the crystal fields, we obtain on-site SK parameters. Finally, we augment the band energy with a repulsive contribution to account for the difference of the total energy and TB energy. Our parameters are reasonably accurate for computing various static properties, and quite transferable if the near neighbor distance is varied by not more than 10%. We used these parameters in MC simulation to compute the CTEs of Mo_3Si and $Mo_{53}Si$. The results together with experimental measurements indicate a clear increasing tendency of CTEs when Si concentration is increased.

4.2 Ab-initio studies of impurity effects on structural material's mechanical properties

4.2.1 Effects of grain boundary oxygen impurities in molybdenum

Another important issue in designing Mo-Si-B alloy system is to inhibit intergranular fracture of Mo phase and increase its toughness. Experiments have found the intergranular fracture of Mo is mostly caused by oxygen impurities segregated in the vicinity of Mo grain boundary. The fact that the grain boundary segregation of impurity elements like oxygen and others can strongly affects the mechanical properties of structural materials has been very well known, however, the detailed fundamental mechanisms depend on specific impurity elements and the hosting material, and the same impurity elements can be beneficial for some hosting materials while detrimental for others.

To understand these mechanisms, we carried out atomistic simulations using full potential linear muffin tin orbital (FP-LMTO) techniques [67]. The supercell of the simulated system consists of six molybdenum atoms and two oxygen atoms (Figure 4.14a). The molybdenum atoms were initially put on a body centered cubic (b.c.c.) lattice, while the two oxygen atoms were then introduced as interstitial impurities at the octahedral centers. As the supercell repeats itself to fill up the space, the oxygen impurities will actually form a double layer, representing an idealized case of segregation near the molybdenum grain boundary. The atoms were then allowed to relax their position to minimize the total energy of the system.

After equilibrium was reached, we calculated the charge distribution of the system. Figure 4.14b shows the contour plot of the calculated charge distribution on Mo's (1,1,0) cross section plane. Note that the superpositioned charge distribution of the corresponding free atom species has been subtracted, i.e.,

$$\tilde{\rho}(\vec{R}) = \rho(\vec{R}) - \sum_i \rho^0(\vec{R} - \vec{R}_i) \qquad (4\text{-}13)$$

where, ρ^0 is the charge density of a corresponding free atom, ρ and $\tilde{\rho}$ are the calculated and plotted charge density, respectively. For convenience, we will call $\tilde{\rho}$ "bonding charge density". Therefore, the red (or blue) area in the plot indicates a region where the electron charge density has increased (or decreased) due to the formation of solid. For comparison, the similarly prepared bonding charge contour plot of a pure b.c.c. Mo system is displayed in Figure 4.14c.

Apart from the apparent lattice relaxation (which clearly indicates a stretch and weakening of Mo bonds), we see a number of changes in the electronic structure features:

- The oxygen core area is marked red since it withdraws charges from surrounding and other areas and becomes ionized. In response, the surrounding areas try to screen the extra charges in the core by forming a blue shell with decreased electron density.
- The ionic oxygen induces severe charge density fluctuations among the adjacent Mo atoms. For the immediate neighboring Mo atom (denoted by Mo^{1}), even in the core area, charge distribution is being significantly altered compared with the pure Mo atom (displayed on right panel): more blue areas appear, meaning that some core electrons have leaked out to the surrounding electron clouds, thus making Mo^{1} partially ionized. The partially ionized Mo^{1} then forms strong ionic bonds with the ionic oxygen.
- When we looked at the second nearest Mo atom (denoted by Mo^{2}), it is not as partially ionized as the Mo^{1}. However, affected by the presence of the nearby oxygen, there is a net increase of charge in their surrounding electron clouds. This induced charge must have come from other regions of the system, i.e., from nearby third layer Mo (denoted by Mo^{3}), or from interstitial free electrons that are responsible for the metallic bonding. In either case, since electrons are asymmetrically localized (as being captured by the Mo^{2} core), the Mo^{2}-Mo^{3} bond is weakened.

Overall, we have seen that the introduction of oxygen impurity has induced significant electronic charge redistribution in its nearby regions. Some interstitial free electrons originally responsible for Mo-Mo metallic bonding are either withdrawn by oxygen to form ionic bonds, or swallowed by the first or second layer Mo's electron clouds to become more localized. Therefore, the characteristic of bonding changes from metallic to partial ionic. Since the original metallic bonds are crucial to hold the solid flexible upon deformation and to resist cracking, we conclude that the mechanical property is compromised, i.e. trace amount of residual oxygen at grain boundary promotes intergranular fracture. The fracture is most likely mediated through broken

bonds between the second and third layer Mo, since the chemical bonding is significantly weakened there as indicated in our simulation.

This helps to explain some of the experimental observations. We see the unalloyed Mo with grain boundary oxygen impurities suffers from low fracture toughness. The observed failure type is mostly intergrannular fracture. When Si and B are included in the alloy system, they tend to form protective silica glass scale to prevent further oxidation [11,17,21,33,35,59-61]. Therefore, depending on the microstructural morphology, the grain boundary oxygen impurity level will decrease, yielding a much tougher Mo phase. However, as the applied load ultimately exceeds the strength of Mo_3Si and Mo_5Si_2B, catastrophic failure (i.e. transgrannular fracture) occurs due to the brittleness of the ceramic phases.

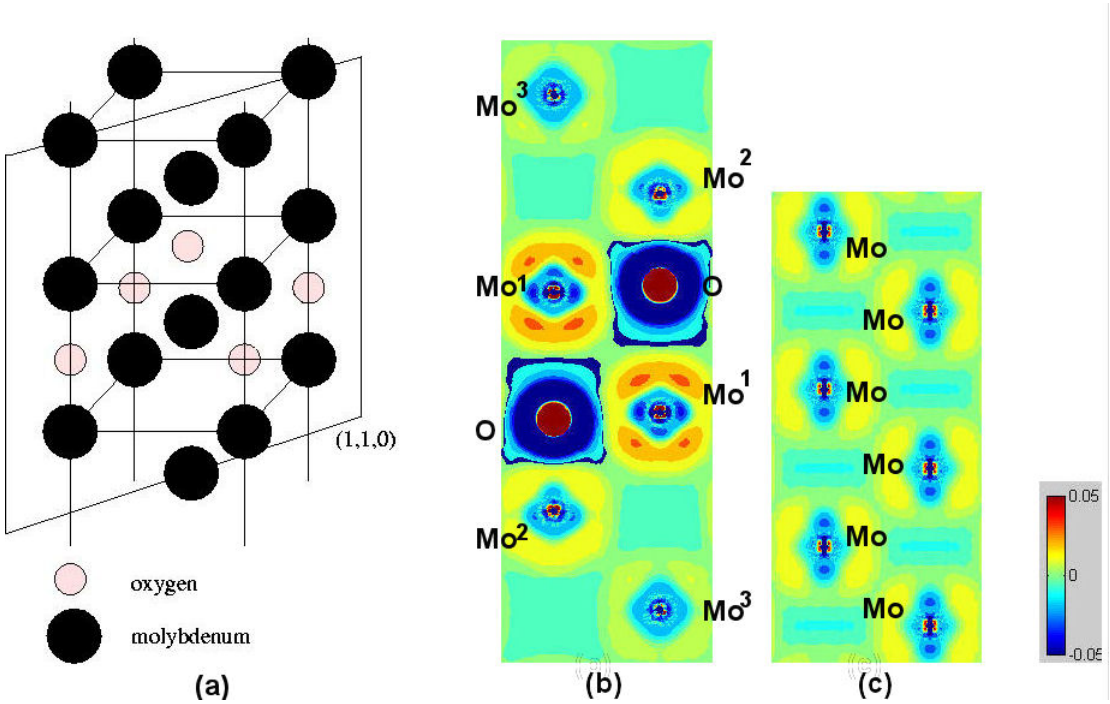

Figure 4.14: (a) the unit cell of simulated Mo system with oxygen impurities, (b) bonding charge density contour plot, and (c) bonding charge density contour plot for a pure Mo system. The colorbar scale is in unit of $bohr^{-2}$.

4.2.2 The inclusion of MgO to control nitrogen impurities effects in chromium

Having seen the detrimental effects of segregated impurities, we seek for solutions to counteract the impurity effects, or at least to control the damage. The inclusion of metal oxide dispersions has proven to provide an effective way to manipulate the impurity segregation at grain boundaries. In a recent experiment, Brady and

coworkers [9] has demonstrated nicely that tiny dispersions of MgO can improve the ductility of Cr. Through microstructural analysis, they found nitrogen impurities appears to be mostly segregated to the vicinity of oxide-metal interface. Therefore, they hypotheses that the MgO phase tends to attract nitrogen impurities and thus prevents them from segregating to the Cr grain boundaries and forming brittle nitrides.

To understand the fundamental mechanism responsible for the ductility enhancement, we performed a comparative study about the MgO effects on Cr with N impurities. Shown in Figure 4.15a and Figure 4.16a are system I and II we have studied, respectively. Both systems consist of four Cr, two N, two Mg, and two O atoms. The difference is that in system I, the N atoms are placed at the center between the 4 Cr layers (notice the periodic boundary conditions imposed in z-direction), whereas in system II, they are placed in between the Cr-MgO interface. Therefore, system I represents a Cr-MgO system with N impurities segregated at the Cr grain boundary, whereas system II represents a system with impurities attracted by MgO and thus a clean Cr grain boundary. Both systems were relaxed from their initial configuration, until an equilibrium configuration is reached.

At equilibrium, system I is 18eV/atom less stable than system II. This shows that nitrogen impurities are stabilized by MgO-Cr interface, supporting the impurity management conclusion from experiment. Fig.15b and 16b show the corresponding bonding charge density contour plot at equilibrium. Comparing the two systems, we found the following common features:

- In both cases, the nitrogen core is marked red and surrounded by a blue shell: just like the case of oxygen in molybdenum, nitrogen will withdraw some charges from other atoms and becomes ionized, and the blue shell comes from the induced screening effects.
- Interestingly, the oxygen atoms, whose cores are also marked red, are not surrounded by blue shells. The electric field due to their excessive charge must have been screened very well by the nearby Mg ions, and thus no additional interstitial screening is necessary.
- In both cases, the charge density distribution near Cr atoms is significantly altered. More localized charge around Cr, and less interstitial charge to form metallic bonds.

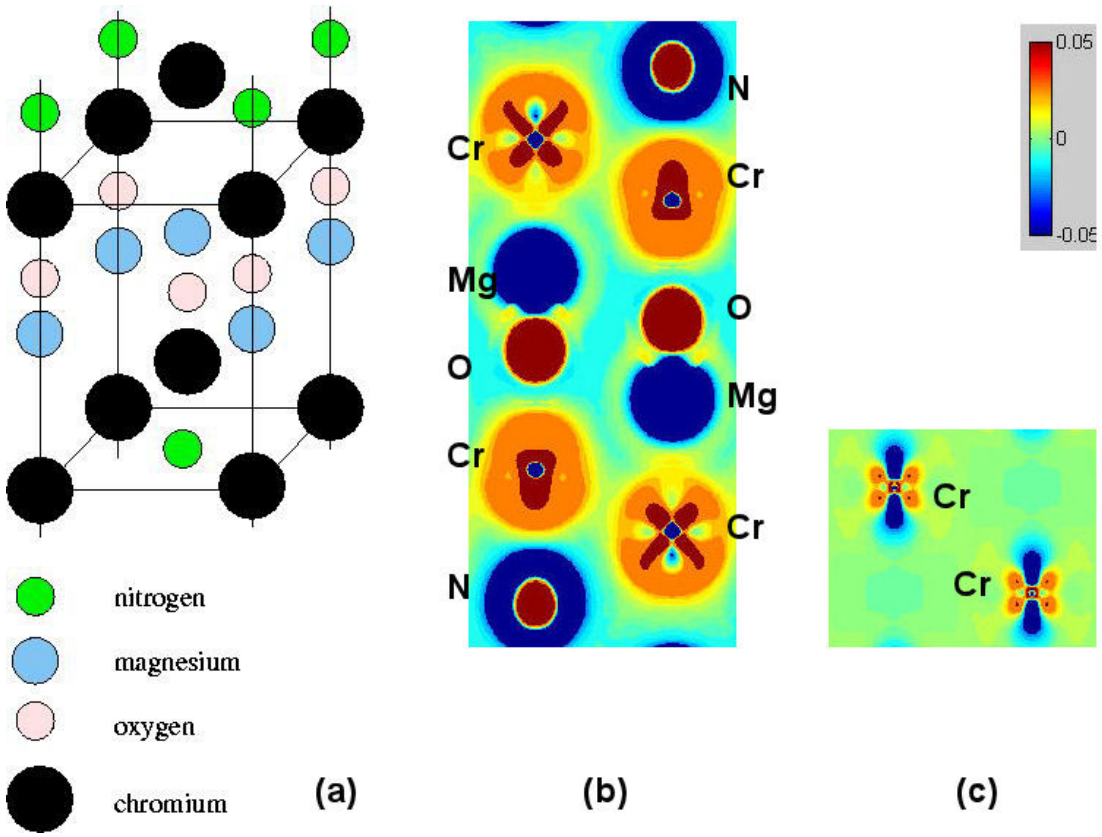

Figure 4.15: (a) the unit cell of simulated MgO-Cr system with nitrogen impurities at the Cr boundary, (b) bonding charge density contour plot, and (c) bonding charge density contour plot for a pure Cr system. The colorbar scale is in unit of $bohr^{-2}$.

However, with nitrogen placed near the MgO-Cr interfacial boundary, system II displays some important new features:

- The nitrogen ion's excessive charge is partially screened by the nearby Mg atom. This is reflected by the fact that the blue areas overlap in Figure 4.16b.
- Because of Mg's partial screening, the detrimental effects due to nitrogen are not as severe as in system I. For example, the charge distribution near the Cr atoms is mildly red in system II. The charge density in the interstitial area is also a little bit higher (green as compared to blue) than system I, indicating better metallic bonding.
- Also if we look at the Mg-O ionic bonding, due to the Mg's partial screening for ionic nitrogen, the screening of ionic oxygen is less perfect, as manifested by a light blue shell around oxygen core. This indicates that the Mg-O ionic bond is weakened.

In summary, we found that the Mg ion in MgO will stabilize a nearby negatively charged nitrogen impurity by providing partial screening, therefore neutralizing the

detrimental effects of nitrogen on Cr-Cr metallic bonds. This conclusion is in agreement with the experiment. Essentially, the detrimental impurities create charge redistribution and change the nature of the chemical bonding from metallic to partially ionic. The inclusion of MgO counteracts the above effects by protecting the metallic bonds. It does so at the cost of weakened Mg-O ionic bonds.

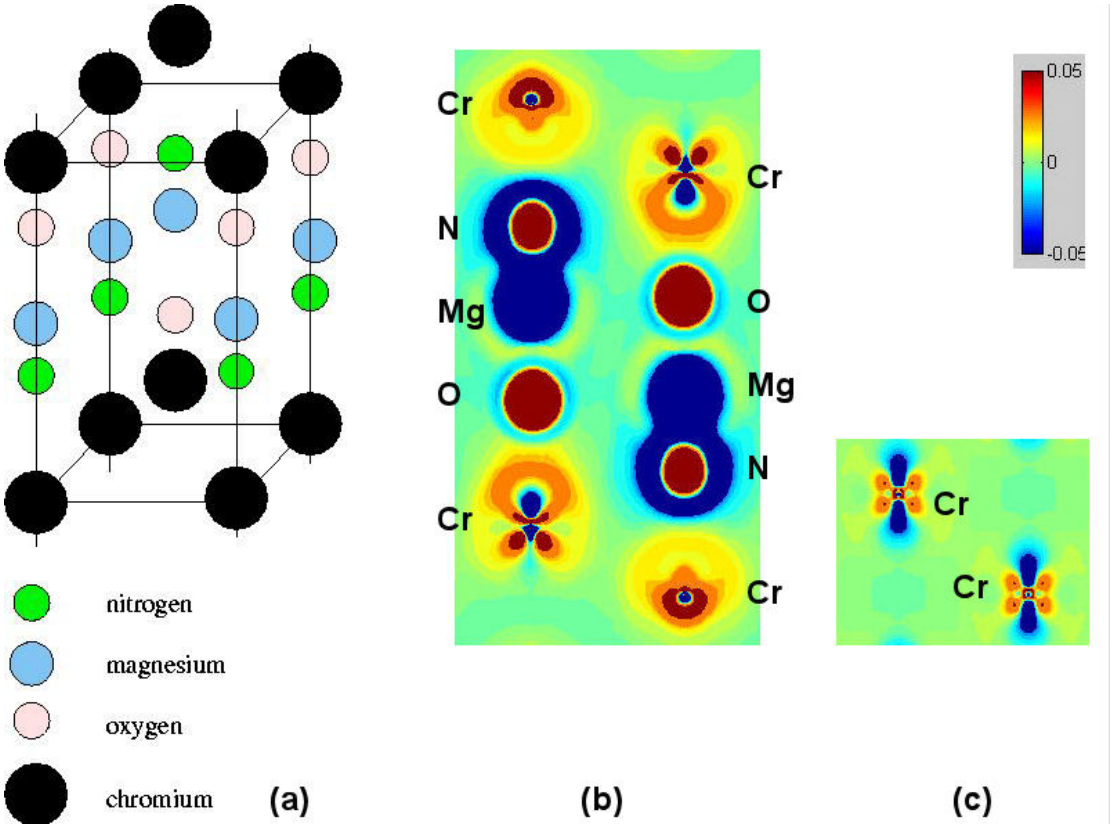

Figure 4.16: (a) the unit cell of simulated MgO-Cr system with nitrogen impurities near the interface, (b) bonding charge density contour plot, and (c) bonding charge density contour plot for a pure Cr system. The colorbar scale is in unit of $bohr^{-2}$.

4.2.3 The effects of the inclusion of TiO2

An interesting discovery of Brady's experiment is that the ductility enhancement by metal oxide dispersion appears to be unique. Some other types of metal oxides, including TiO_2, La_2O_3, and ZrO_2, have been used in replacement for MgO to investigate the ductility enhancement mechanism. Although microstructural analysis has revealed similar impurity stabilization effects by these oxides (i.e., the impurity will tend to segregate near the oxide-Cr interface), none has displayed the corresponding dustily enhancement. In some case the sample even became brittle. Therefore, mechanisms

based solely on microstructual analysis, such as the grain boundary impurity management, are not adequate to explain the ductility enhancement. Here, we attempt to solve the problem base on an electronic structural point of view.

As in the case of MgO, we set up a model system of TiO_2-Cr-N as shown in Figure 4.17a. Since we are not going to reinvestigate the impurity stabilization mechanism, we place the N directly near the interface of TiO_2 and Cr.

At equilibrium, the bonding charge density is plotted in Figure 4.17b. There are a number of clear differences compared the case of MgO in Figure 4.16b:

- The ionic nitrogen charge does not seem to be screened by Ti. In fact, the nitrogen goes closer to the Cr side rather than sticking with Ti. (Note the system starts with N placed at the center line between Cr and TiO_2). Therefore, its detrimental effects are not alleviated by the inclusion of TiO_2.
- In addition, the oxygen atom now is surrounded by a screening blue shell. Such blue shell was not present in the Cr-MgO system. This clearly demonstrates that Ti, unlike Mg, lacks the capability of helping to screen ionic oxygen or nitrogen nearby. This capability has been found crucial to explain the stabilization for charged impurities and the alleviation of their detrimental effects.
- As expected, the charge redistribution of nearby Cr is much more significant compared to the MgO case, due to the combined detrimental effects of both oxygen and nitrogen.

In closing, we found the ionic Ti does not possess the capability to screen nearby negatively charged ions. In consequence, the detrimental effects of both oxygen and nitrogen combined to undermine Cr metallic bonds. This may help to explain the none-ductility enhancement results seen in the experiment.

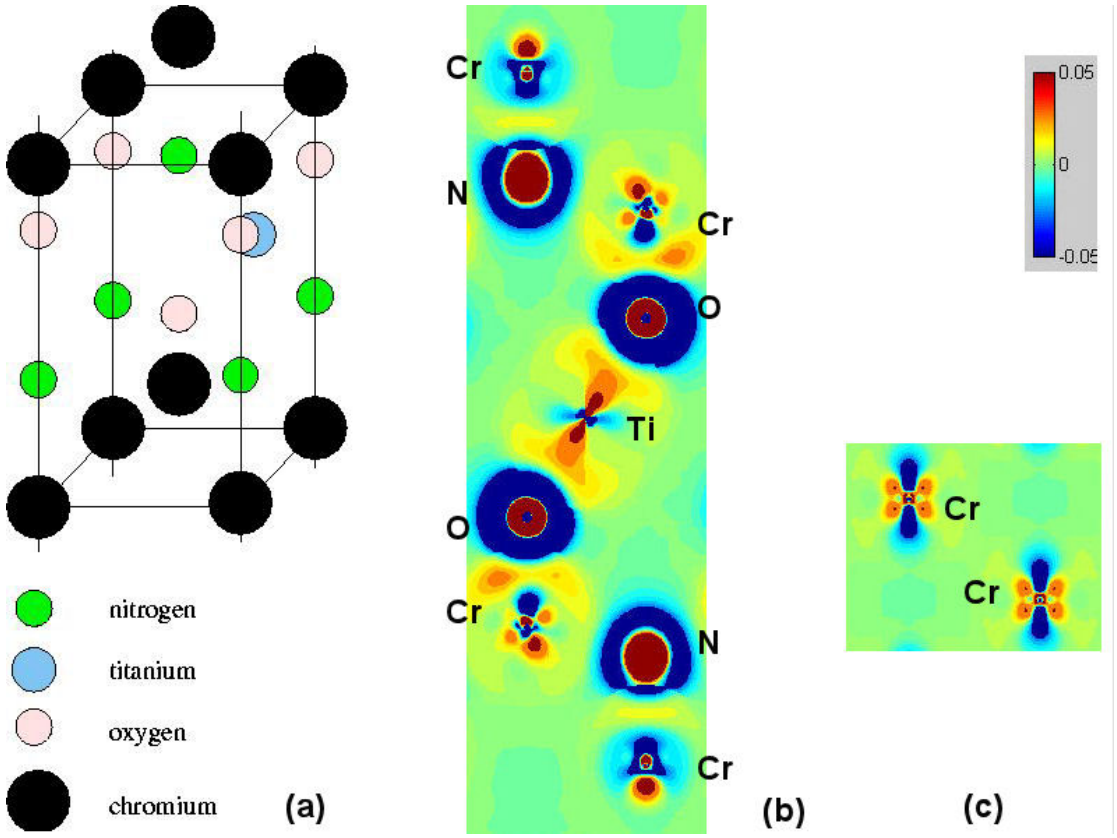

Figure 4.17: (a) the unit cell of simulated TiO_2-Cr system with nitrogen impurities near the interface, (b) bonding charge density contour plot, and (c) bonding charge density contour plot for a pure Cr system. The colorbar scale is in unit of $bohr^{-2}$.

CHAPTER 5 RESULTS AND DISCUSSIONS

5.1 Three-point-bending tests and microstructure analysis

5.1.1 Fracture toughness

It was observed that both Mo and MoSi showed brittle failure at room temperature. However, MoSi showed higher fracture toughness but more brittle behavior at 550°C while Mo showed substantial ductile failure at 550°C.

Table 5.1 Results of fracture toughness

CONDITION / MATERIAL	26ºC, ROOM TEMPERATURE	550ºC
Mo	14.97 *	10.46 **
MoSi	8.33 *	21.52 *

Unit: $MPa\sqrt{m}$

*Brittle Failure

**Large damage zone were observed at crack-tip region, crack growth initiated at $K_I = 10.46\, MPa\sqrt{m}$

5.1.2 Thermal expansion measurement

Figure 5.1 shows comparison of thermal strain measurement between moiré interferometry and TMA on the same material. Good agreement is noted. Using least square linear curve fitting, the CTE values are, 8.16×10^{-6} for Mo and 7.77×10^{-6} for MoSi.

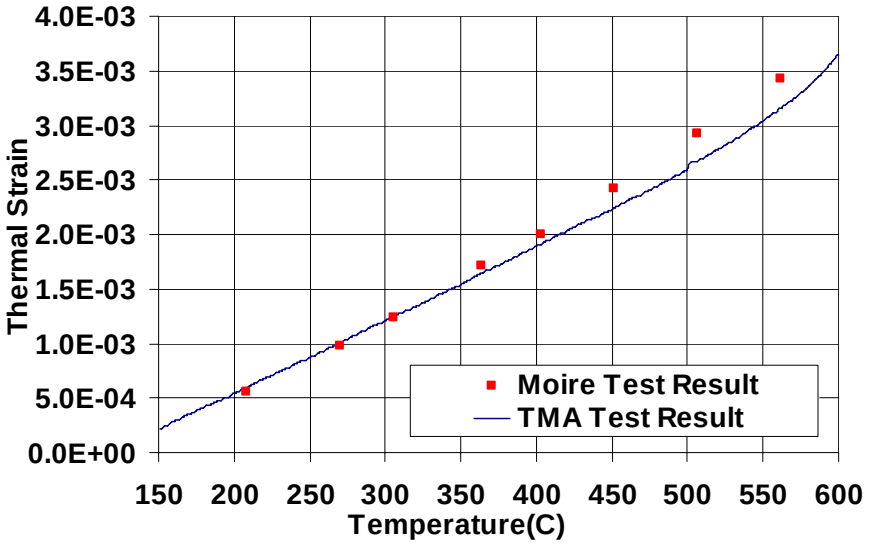

(a) Mo

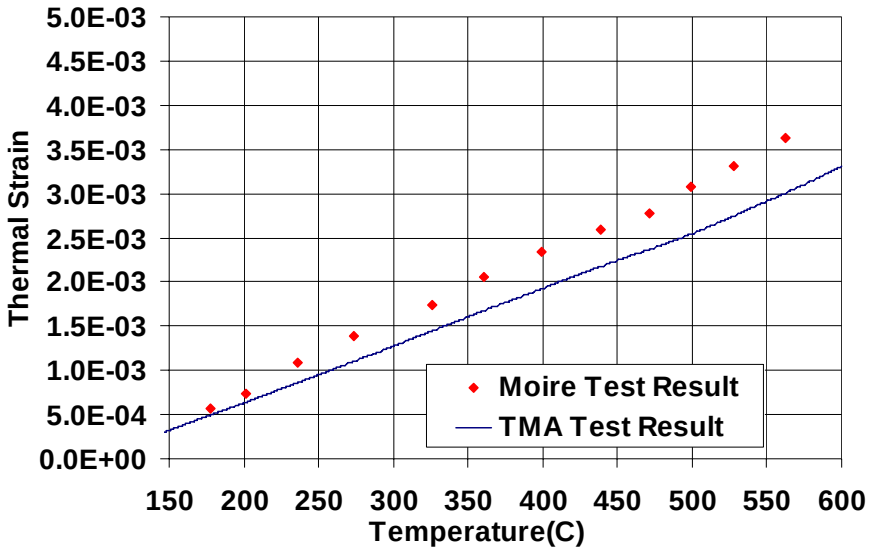

(b) MoSi

Figure 5.1 Results of thermal strain measurement

5.1.3 Crack tip deformation measurement results

Figure 5.2 shows typical in-plane u and v deformation fields obtained from moiré interferometry and corresponding phase maps for Mo at room temperature. The dotted line represents grain boundaries identified from the deformation fringe pattern and microstructural observation. From the deformation fields, it clearly shows grain boundary sliding, especially near crack tip region. Figure 5.3 shows the unwrapped fields from corresponding phase map. As shown, large shear deformation was clearly observed, aided by pseudo colors.

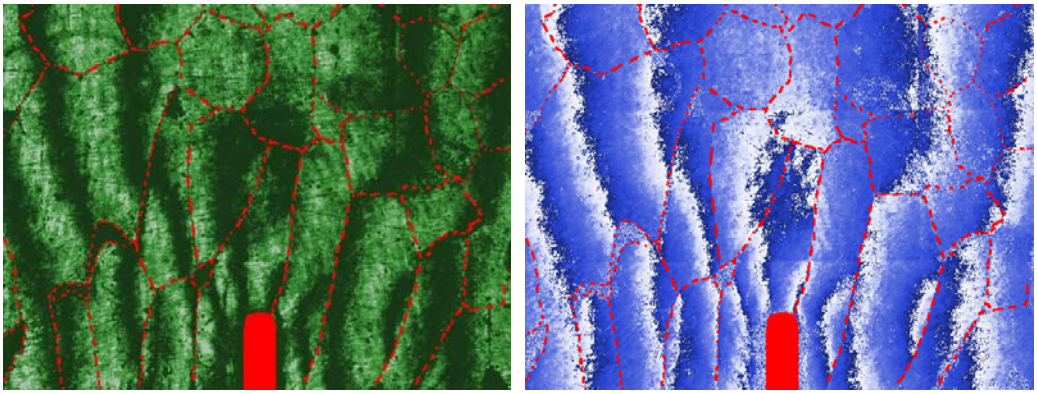

(a) *u* field *u* phase map

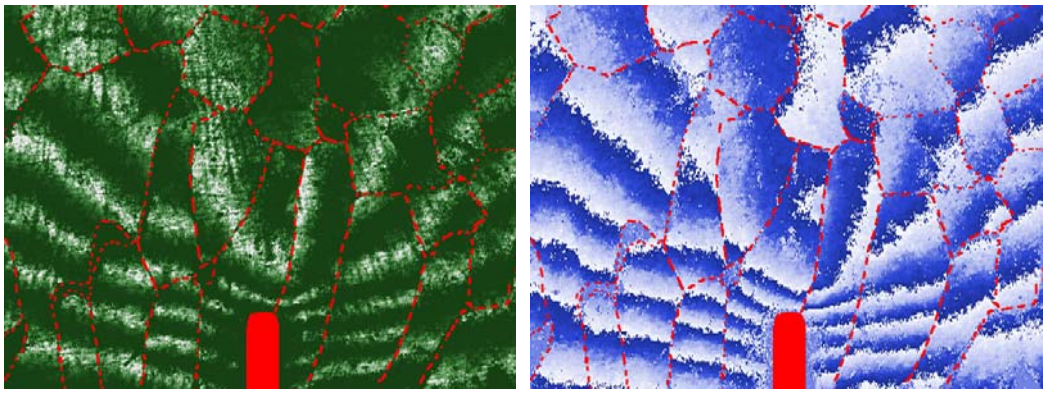

(b) *v* field *v* phase map

Figure 5.2 Mo at room temperature, in-plane *u* and *v* field, $K_I = 14.21 MPa\sqrt{m}$

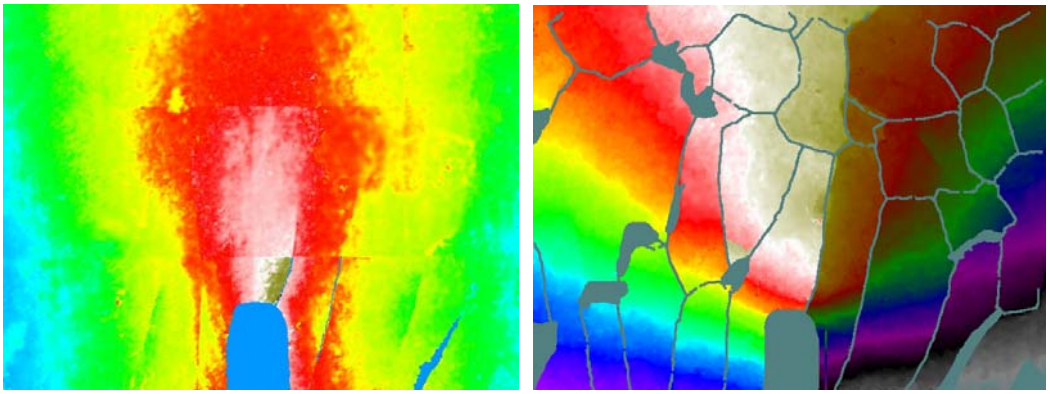

(a) *u* field (b) *v* field

Figure 5.3 Pseudo-color displacement fields

At elevated temperature (550°C), ductile crack tip deformation of Mo was observed with a smaller K_I value as shown in Figure 5.4.

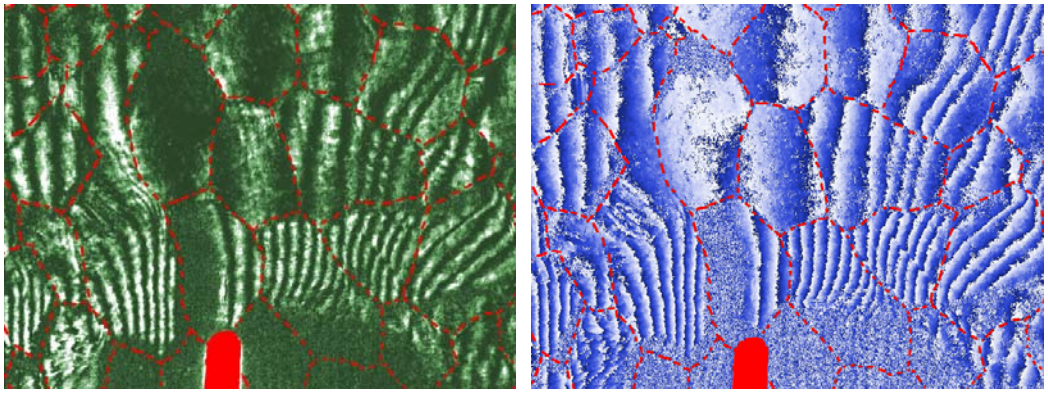

(a) *u* field *u* phase map

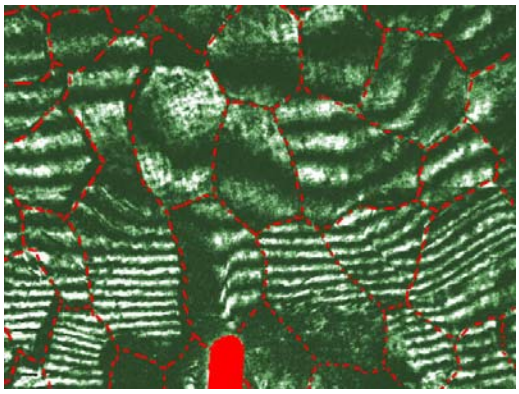
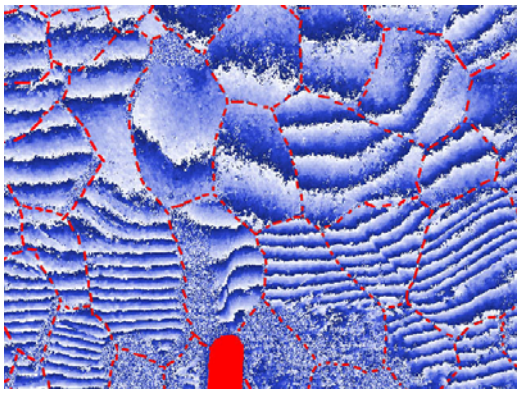

(b) *v* field *v* phase map

Figure 5.4. Mo at 550°C, in-plane *u* and *v* field, $K_I = 7.66MPa\sqrt{m}$

However, for MoSi with only 0.745wt% silicon addition, the deformation pattern changed dramatically as shown in Figures 5.5 and 5.6. For both room temperature and elevated temperature (550°C), brittle failure was observed without apparent grain boundary sliding.

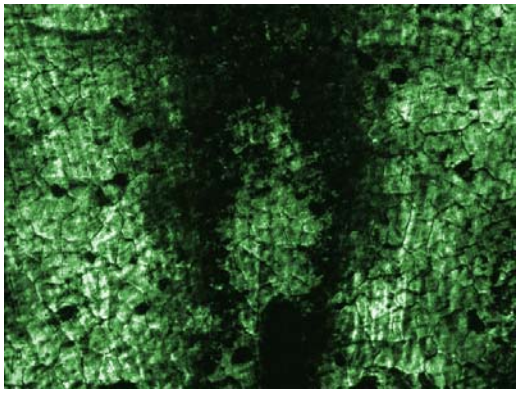
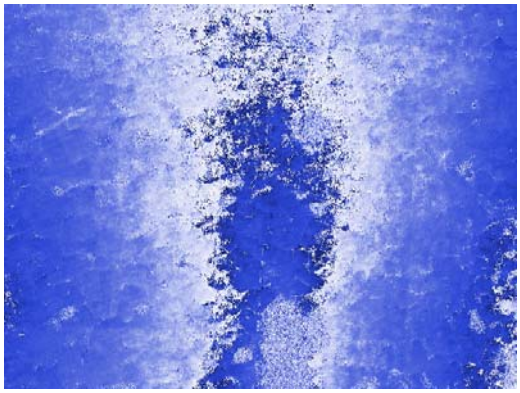

(a) *u* field *u* phase map

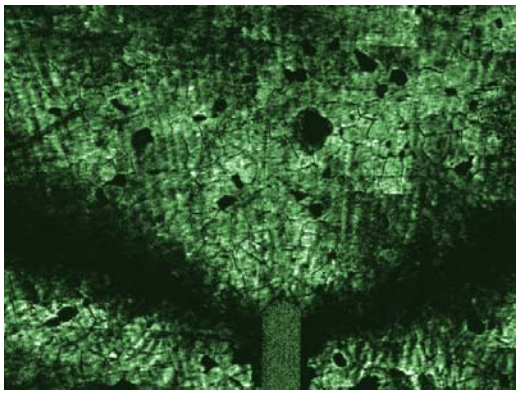
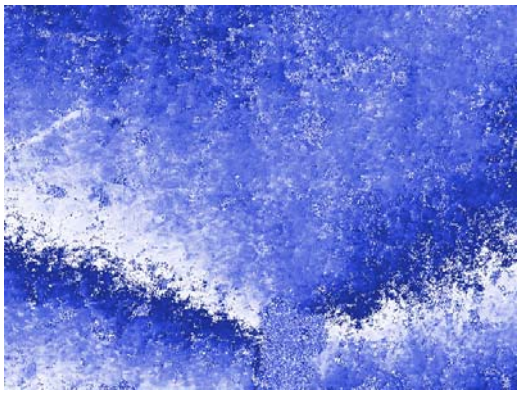

(b) *v* field *v* phase map

Figure 5.5 MoSi at room temperature, in-plane *u* and *v* field, $K_I = 7.54MPa\sqrt{m}$

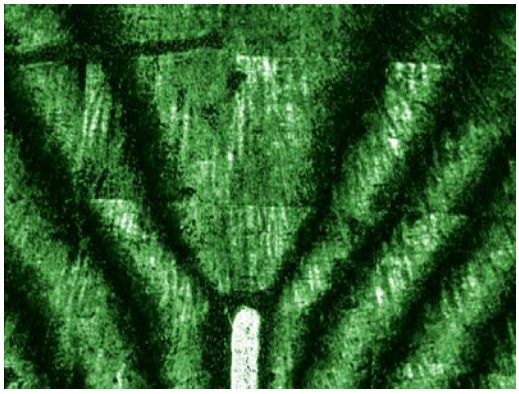

(a) *u* field

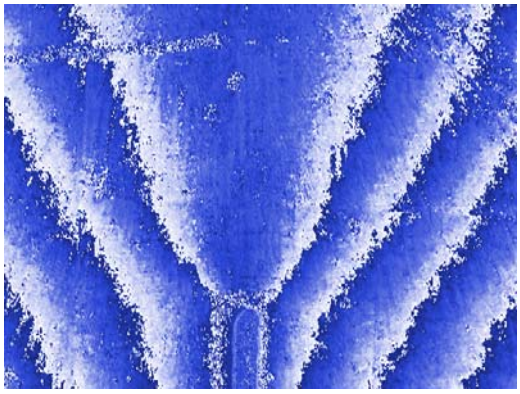

u phase map

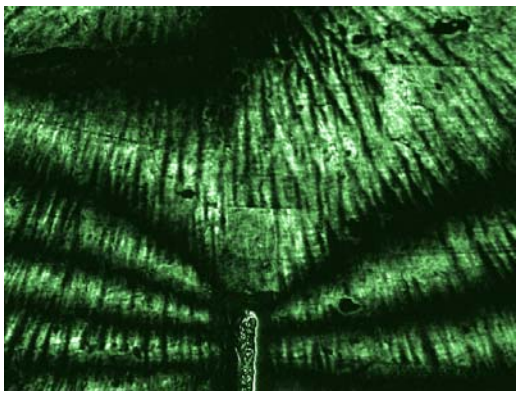

(b) *v* field

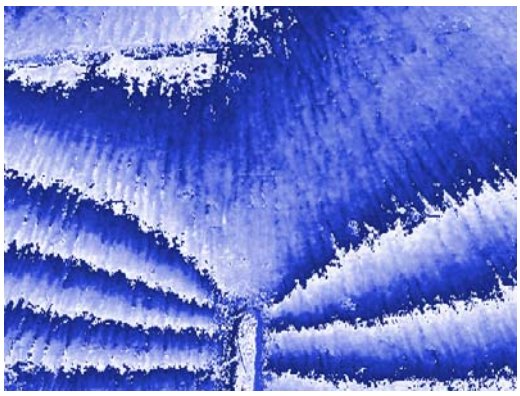

v phase map

Figure 5.6 MoSi at 550°C, in-plane *u* and *v* field,
$K_I = 19.80 MPa\sqrt{m}$

5.1.4 Post-mortem fractography

Figure 5.7 shows corresponding fractographic analyses. Failure modes are different for Mo and MoSi alloys. At the initial stage (near the notch), intergranular failure is dominant for Mo alloy. However, for MoSi alloy, transgranular is the dominated failure mode. This also confirmed the observation from moiré interferometry. Due to the addition of silicon, the grain boundary is strengthened for MoSi alloy.

Notch

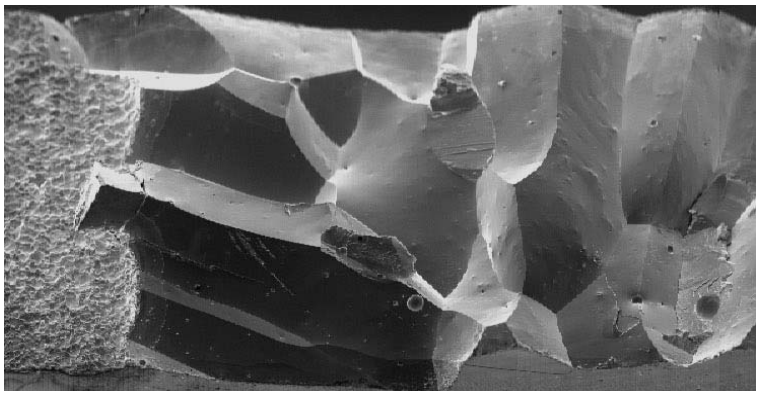

(a) SEM fractography of Mo alloy tested at room temperature

Notch

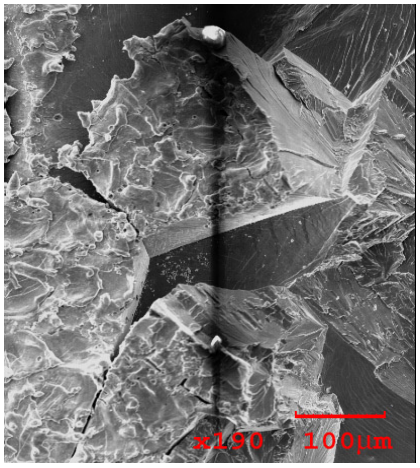

(b) SEM fractography of Mo alloy tested at 550ºC

Notch

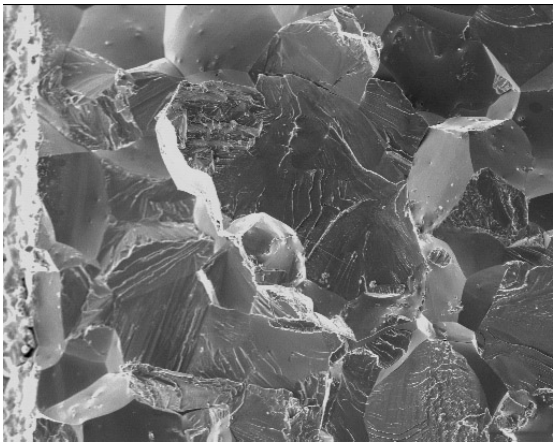

(c) SEM fractography of MoSi alloy tested at room temperature

Notch

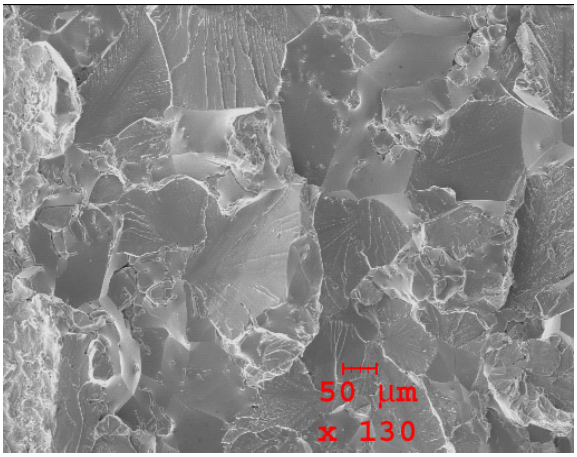

(d) SEM fractography of MoSi alloy tested at 550ºC
Figure 5.7. Fractographic analyses

5.2 Uniaxial tensile tests and microstructural analyses

Tensile test results of alloy #695, #697 & #698 are discussed in this chapter. Post-mortem fractography analysis were conducted and correlated to the stress-strain curves. For each alloy, room temperature and high temperature (650°C) stress-strain curves were obtained with two different displacement loading rates.

5.2.1 Alloy #695

Figure 5.8 shows the stress-strain curves at room temperature and 650°C.

As shown in Figure 5.8Figure (a), at room temperature and under fast displacement rate, alloy #695 showed brittle behavior. At a much slower displacement rate, alloy #695 showed substantial ductility that extends over 10% strain before failure. At higher temperature (650°C) and under fast displacement rate, alloy #695 showed ductile behavior that extends over 30% strain as shown in Figure 5.8 (b).

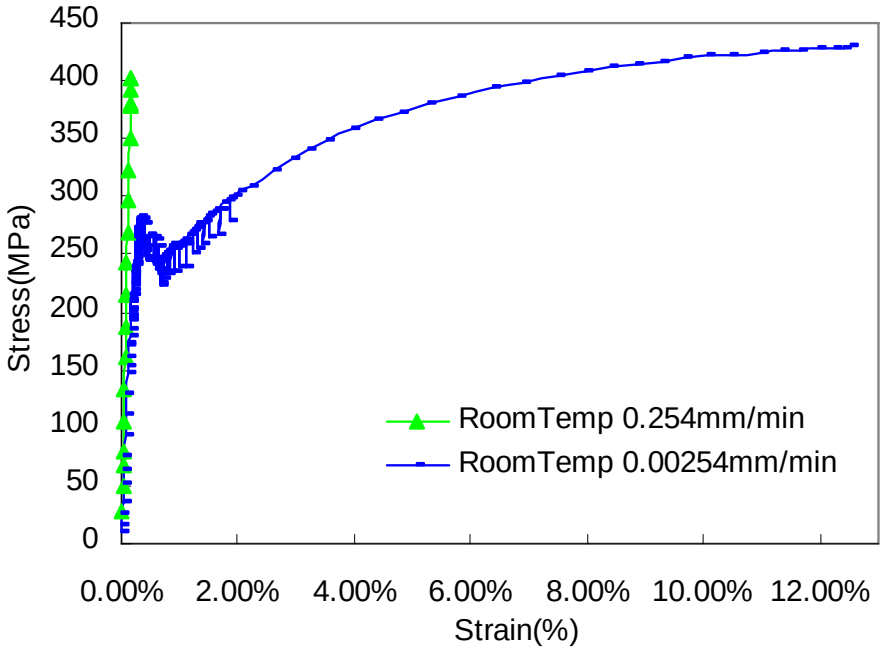

a. Room temperature

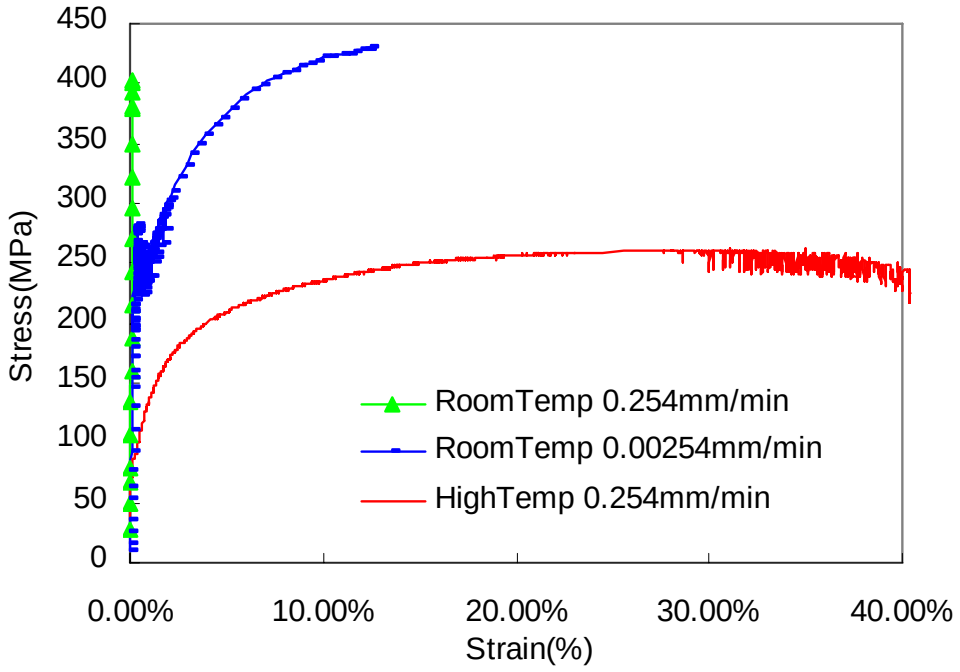

b. Room temperature and 650°C

Figure 5.8 Engineering stress-strain curves of alloy #695

And also for alloy #695 under slow displacement rate at room temperature, interesting phenomenon showed up around yielding point. In Figure 5.8a, it is obvious

that slow displacement rate stress strain curve showed a lot of jitters before and after yield. We have checked the machine carefully, this cannot be from the noise, and also the magnitude of the jitters can also not be noises. From broken specimen, we carefully inspected the specimen surface and fresh fracture surface, as shown in Figure 5.9 and Figure 5.10, we found out that this may due to the poor grain bonding of the alloy, which has only 1 processing hours. At room temperature, under slow displacement rate, the alloy may have time to develop the microcracks as shown in Figure 5.10; under fast displacement rate, no surface microcracks have been found.

Figure 5.9 to Figure 5.11 showed typical tensile test specimens with optical and SEM pictures. SEM facture surface pictures showed that at room temperature intergranular fracture occurred when the specimen failed (Figure 5.9(c) and Figure 5.10(c)). Most brittle fractures occur in a transgranular manner. However, if the grain boundaries contain a film of brittle constituent, as in sensitized austenitic stainless steel or molybdenum alloys containing oxygen, nitrogen, or carbon, the fracture will occur in an intergranular manner [22]. At high temperature, the micro-voids in fracture surface showed clearly that the specimen broke in a ductile manner (Figure 5.11(b)). Due to the oxidation, post-mortem surface condition is not available at higher temperature.

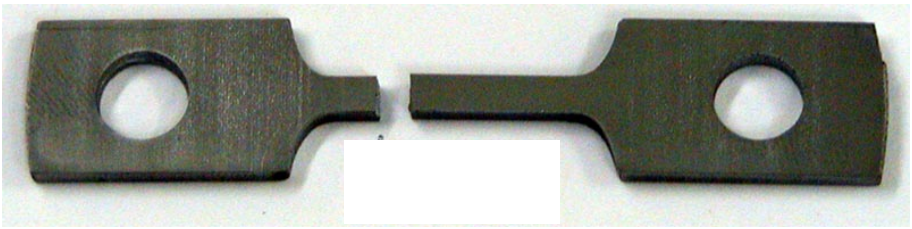

a. tested specimen

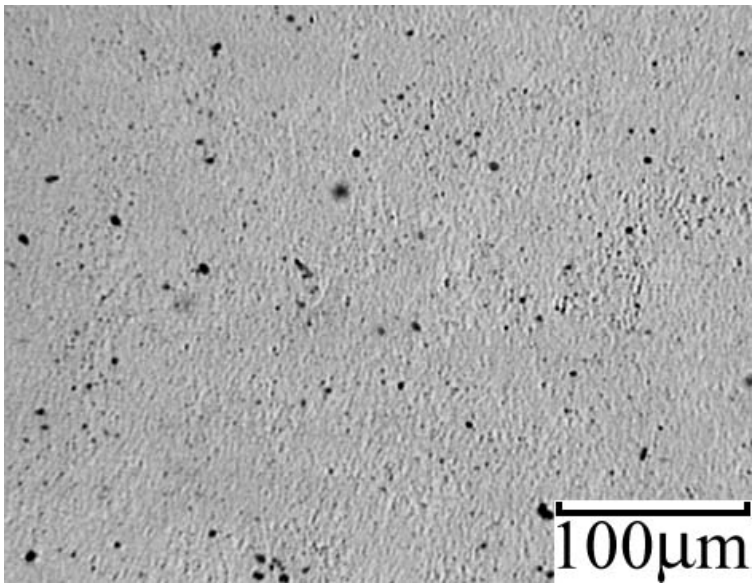

b. Surface condition

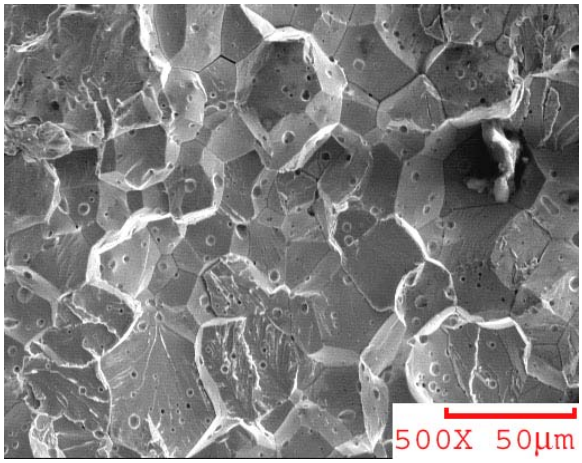

Near Edge

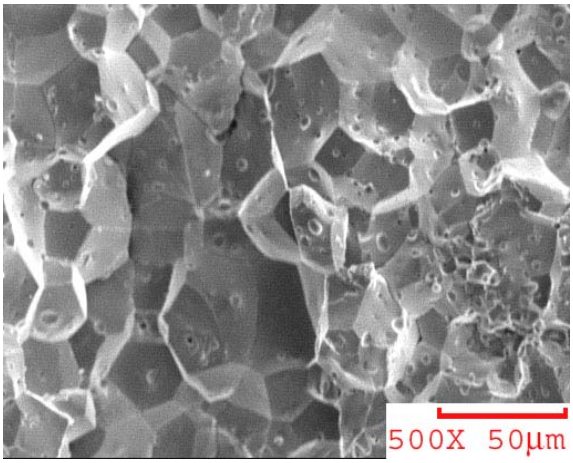

Near Center

c. SEM fracture surface

Figure 5.9 Room temperature fast displacement rate broken specimen

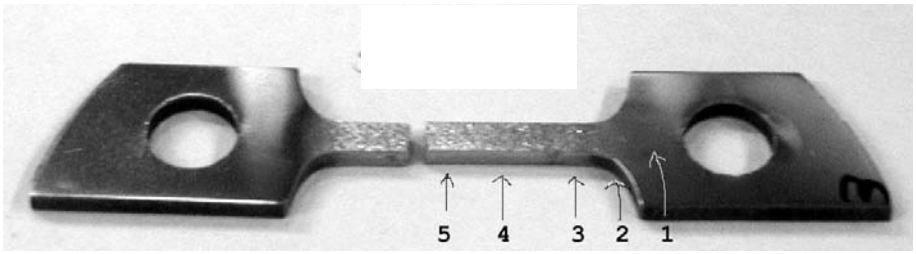

a. tested specimen

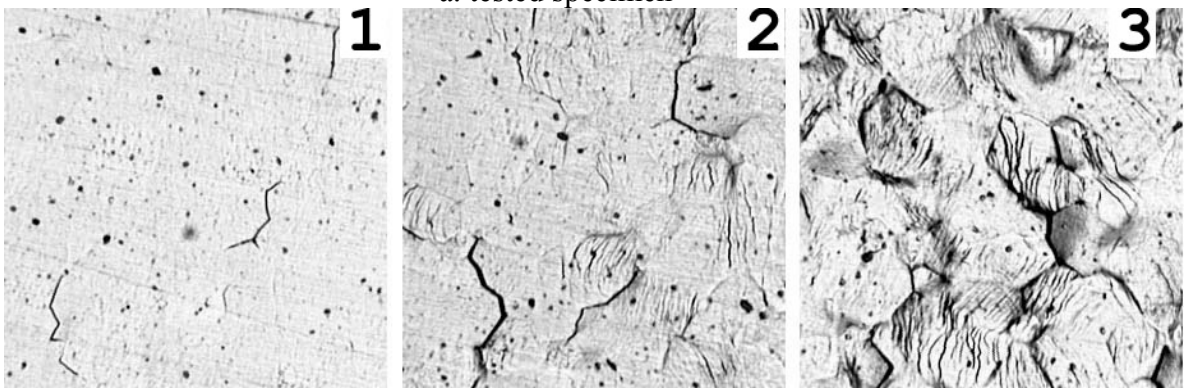

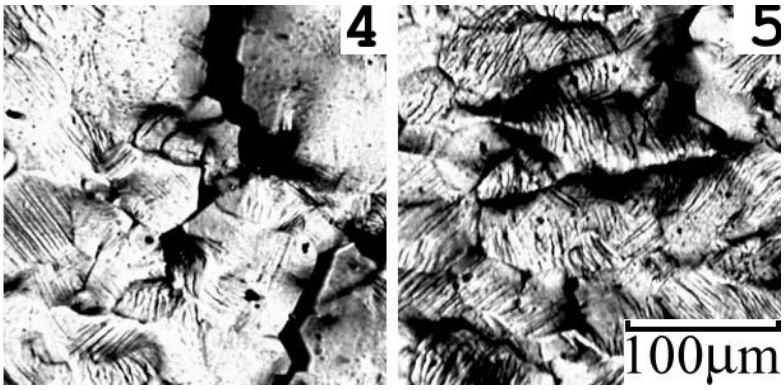

b. Surface condition: correspond to label 1-5 on broken piece

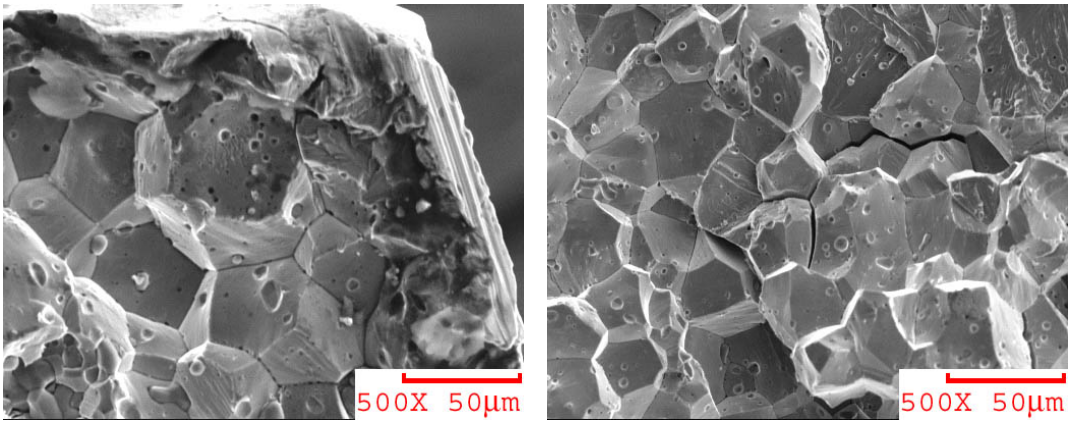

Near Edge Near Center

c. SEM fracture surface

Figure 5.10 Room temperature slow displacement rate broken specimen

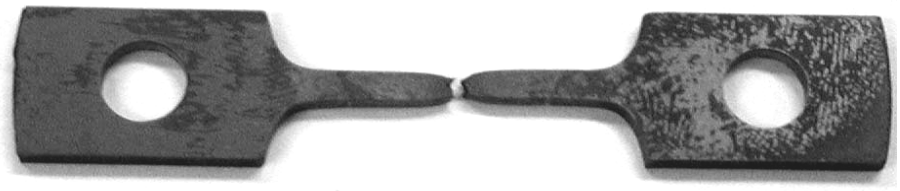

a. tested specimen

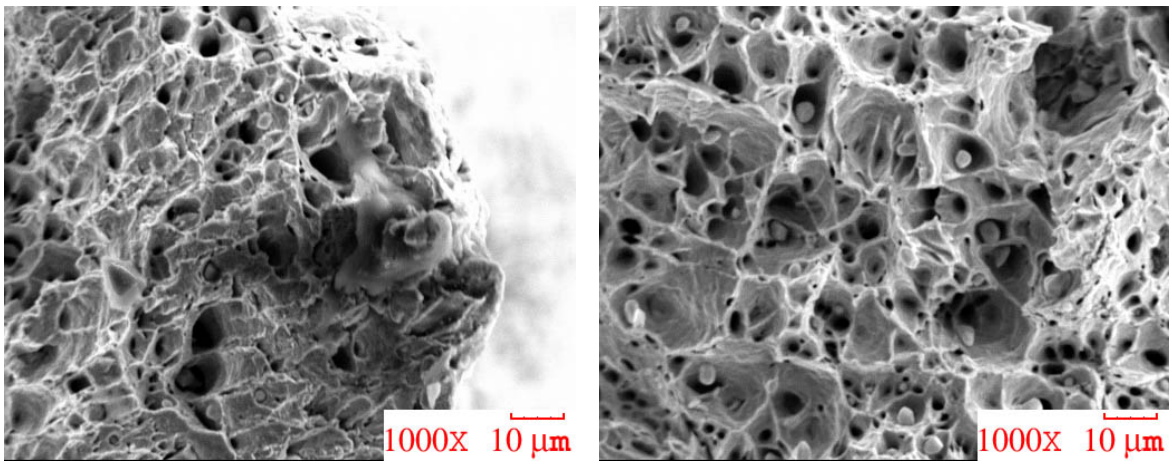

b. SEM fracture surface

Figure 5.11 High temperature fast displacement rate broken specimen

5.2.2 Alloy #697

Figure 5.12 showed the stress-strain curves at room temperature and 650°C.

At room temperature as shown in Figure 5.12(a), under fast displacement rate, alloy #697 failed in a brittle manner, and under slow displacement rate, it showed more ductile. At slow displacement rate, it also showed a lot of jitters, the same interesting phenomenon as alloy #695, and these jitters also may be due to microcracks. The micro-cracking effect could result in the room temperature ductility increase. Under fast displacement rate, no surface microcracks have been observed on failed specimen.

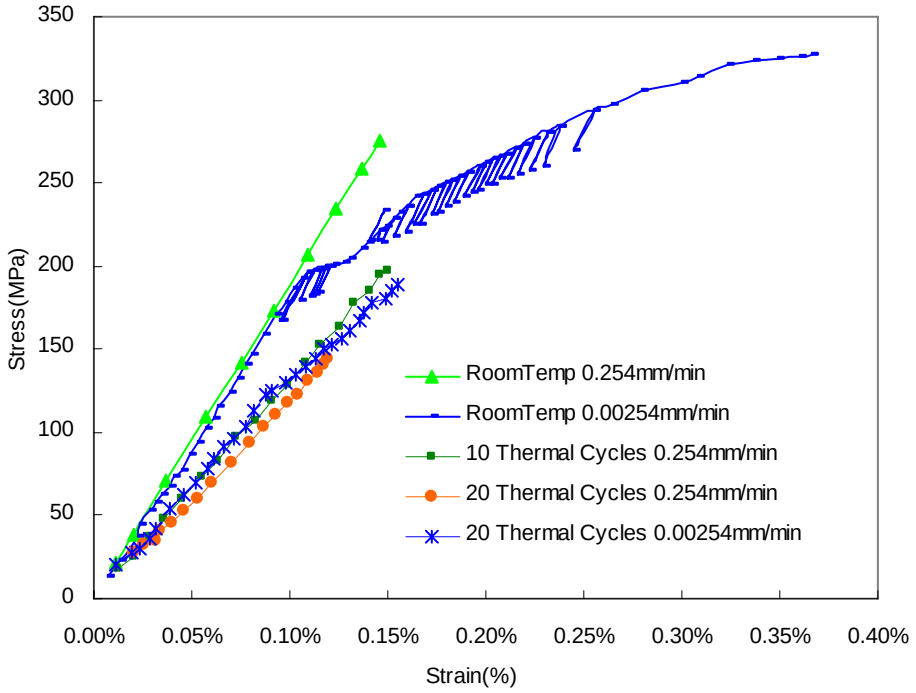

a. At room temperature

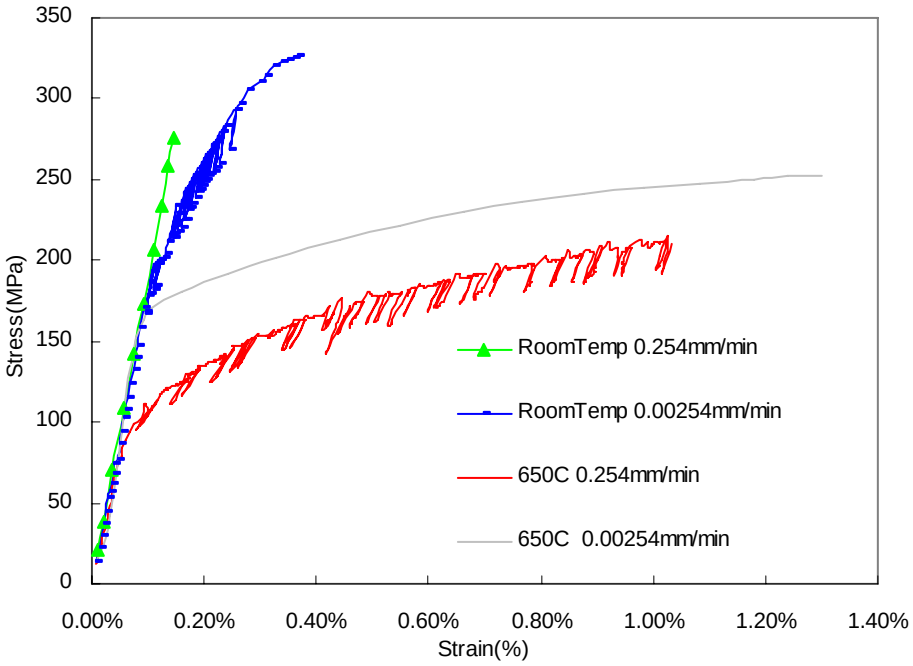

b. At room temperature and 650°C

Figure 5.12 Engineering stress-strain curves of alloy #697

At elevated temperature, the spinel dispersed Mo alloy showed different behavior: fast displacement rate tests showed a lot of jitters while slow displacement rate tests showed smooth stress-strain curve. This result may be correlated to the particle size and distribution of this alloy. One possible interpretation could be as follows.

As shown in Figure 5.13, the spinel particle picture is obtained from the backscattered electron image (BSE), and the plot shows particle size vs. the area probability (see microstructure analysis for detail about this plot). Bigger particles occupied about half of the total particles. At high temperature, the CTE mismatch may cause internal localized tensile stress concentration. This superimposed stress field of localized tensile stress and applied stress at large particle sites may rapid crack under fast displacement rate. Due to strain rate sensitivity, at slower displacement rate this may not happen.

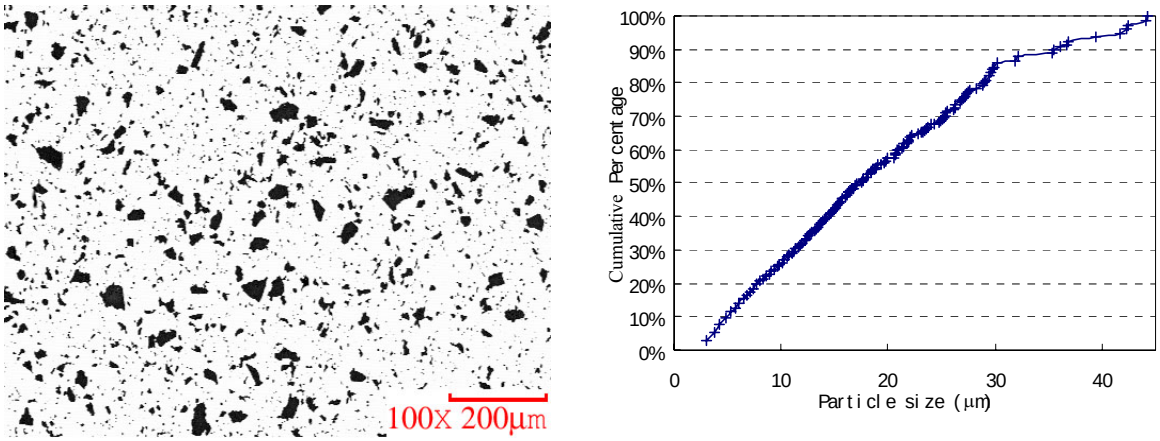

Figure 5.13 Typical spinel particle size and distribution, alloy #697

From Figure 5.12(a), it clearly shows that after thermal cycle(s) (TC), the material has been degraded. Immediately after applied load the material is damaged, and that is why we see a smaller slope in Figure 5.12(a). No matter how many cycles we applied, the material showed similar mechanical properties as in Figure 5.12(a), which means that the first thermal cycle may already cause internal damage. The cracking may be not big enough to be viewable, that is why surface microcracks were not observed under microscopy on the one thermal cycle specimen as shown in Figure 5.26. Figure 5.18 showed the surface microcracks of the tested tensile specimen undergone thermal cycles.

Wide spread microcracks were observed and could be traced to the site of larger spinel particles.

Figures 5.12 to 5.18 showed typical tensile test specimens with optical and SEM pictures. In the SEM fracture surface pictures, light particles are the spinel phase. From Figure 5.17(b), one could clearly observe the pull out of the spinel inclusions.

a. tested specimen

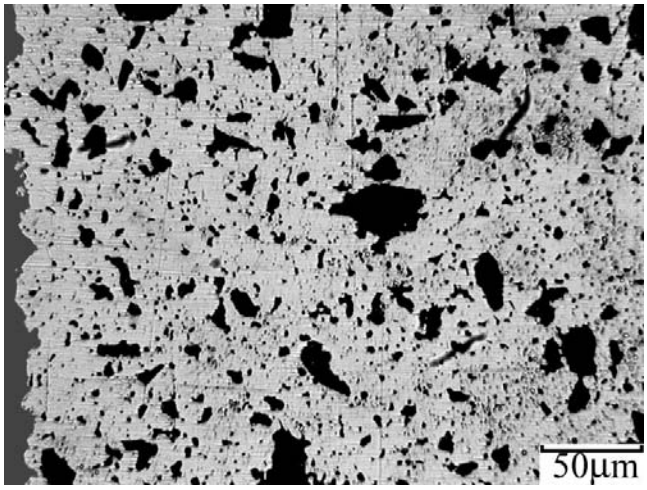

b. surface condition (No microcracks)

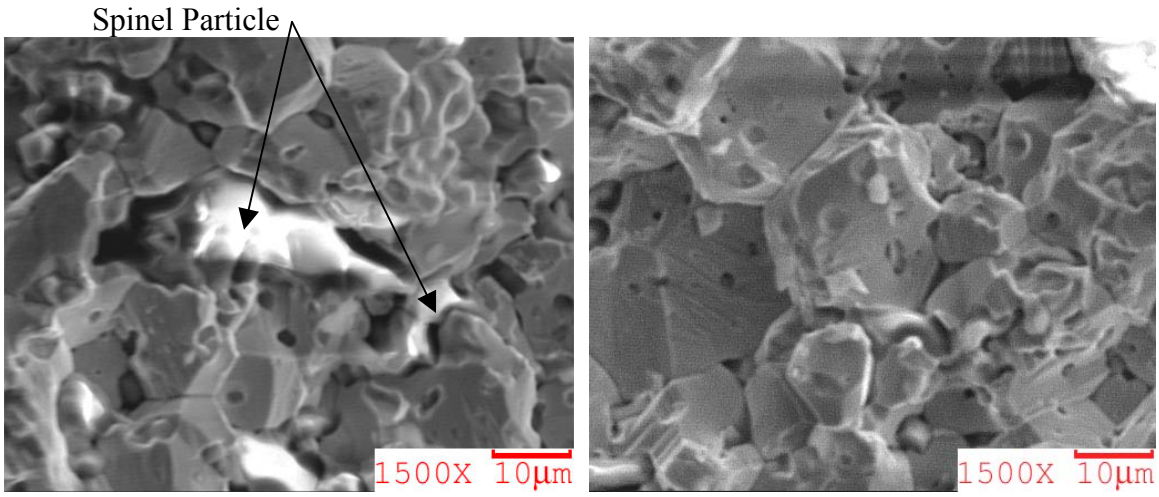

Near Edge Near Center

c. SEM fracture surface

Figure 5.14 Room temperature fast displacement rate broken specimen

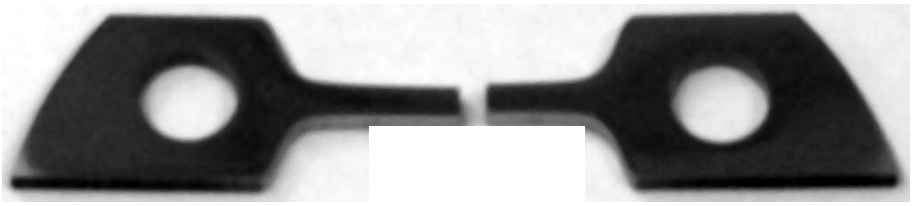

a. tested specimen

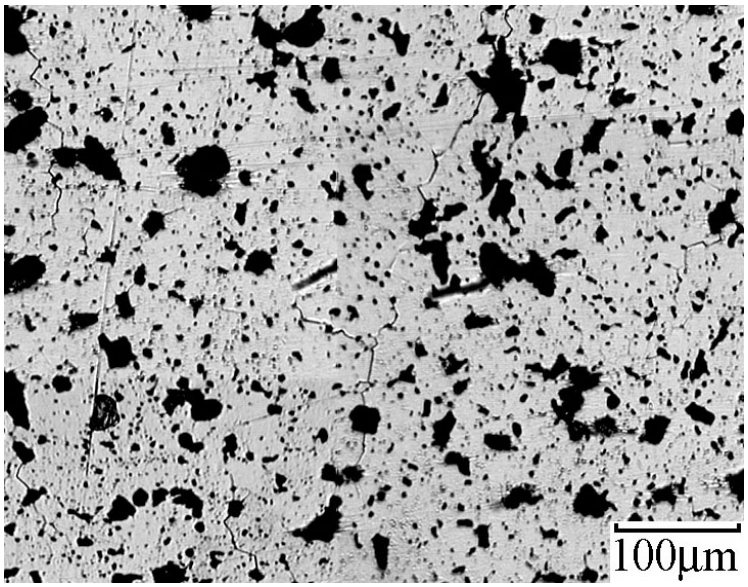

b. surface microcracks

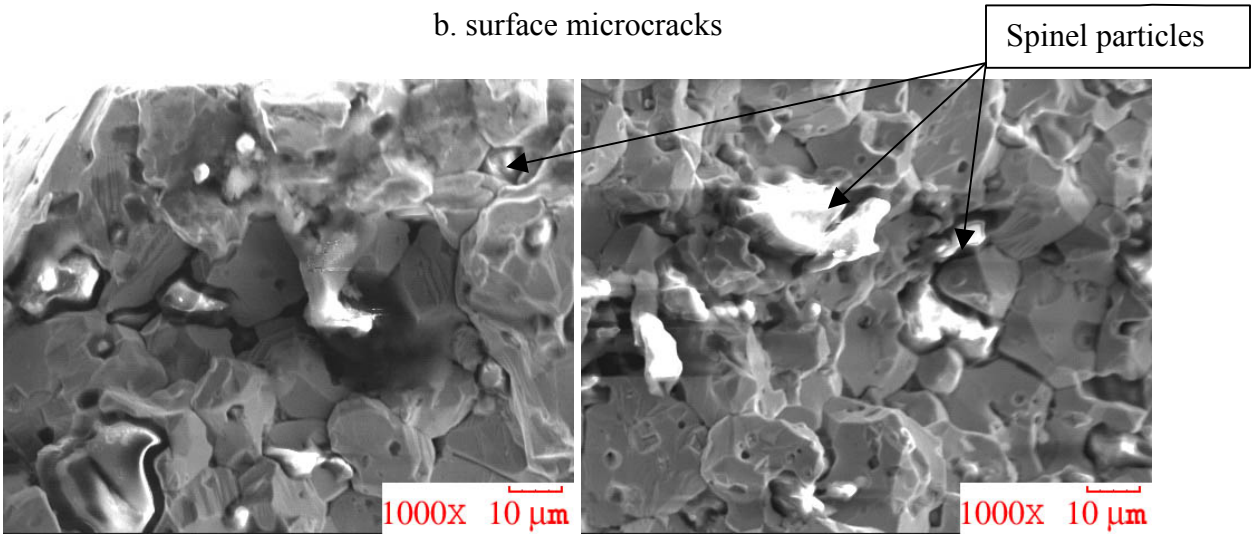

Near Edge Near Center

c. SEM fracture surface

Figure 5.15 Room temperature slow displacement rate broken specimen

a. tested specimen

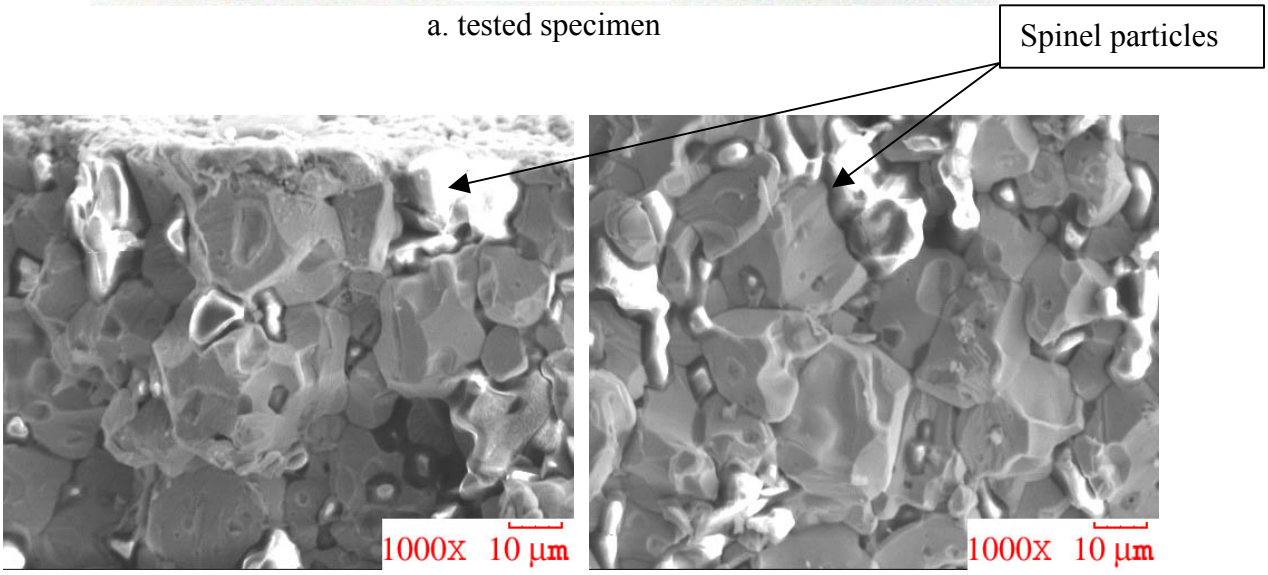

Near Edge Near Center

b. SEM fracture surface

Figure 5.16 High temperature fast displacement rate broken specimen

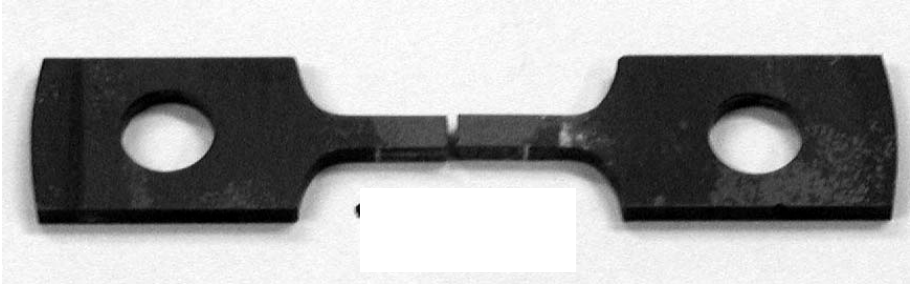

a. tested specimen

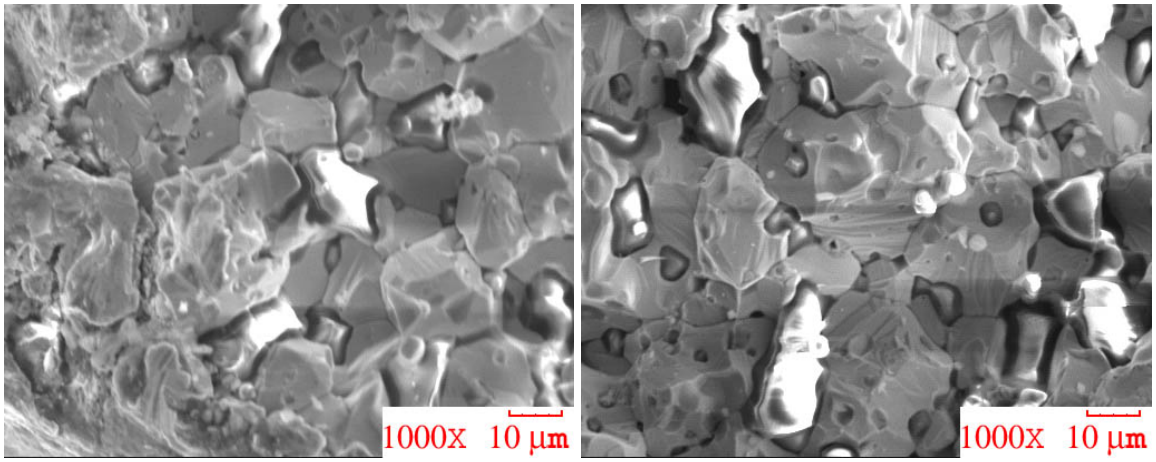

Near Edge Near Center

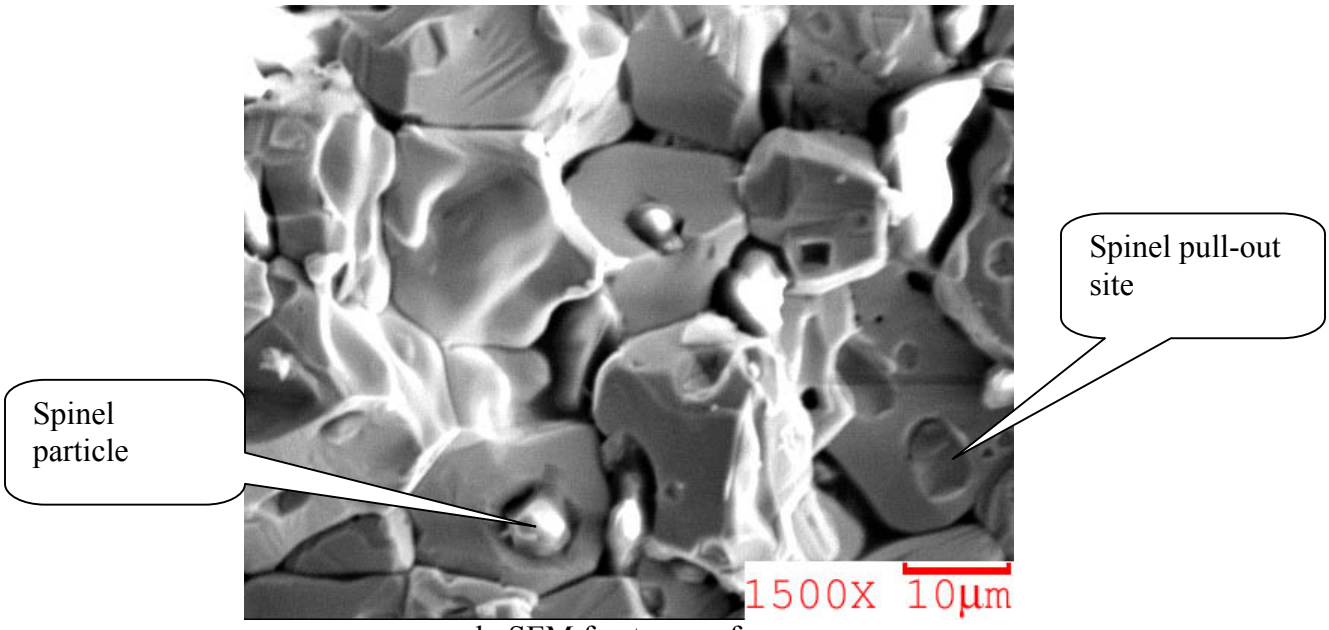

b. SEM fracture surface

Figure 5.17 High temperature slow displacement rate broken specimen

a. tested specimen

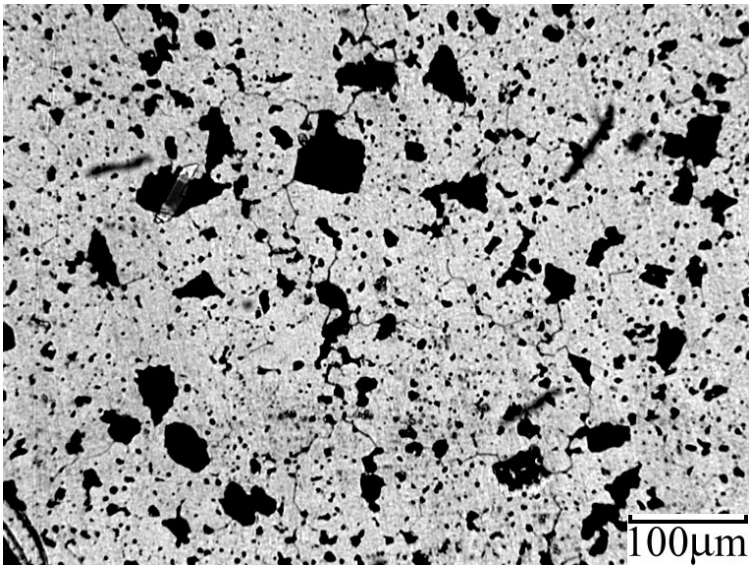

b. surface condition(after test)

Figure 5.18 Thermal cycled slow displacement rate broken specimen (20TC)

5.2.3 Alloy #698

As shown in Figure 5.19, the MgO dispersed Mo alloy clearly exhibited the classic strain rate sensitivity typically for BCC metals such as Mo. For fast displacement rate test, the alloy showed brittle behavior and the tensile elongation is less than 0.1%. But at slow displacement rate, it can reach up to 0.5%. At slow displacement rate, same as alloy #695 and alloy #697, it also showed a lot of jitters after certain level of loading. This may also due to the internal micro-cracks. Under a lower displacement rate, it has time to develop internal micro-cracks, which could severely degrade the material and lead to a lower slope as in Figure 5.19(a). Due to the sensitive of the tensile test measuring system, it is difficult to get the Young's modulus accurately. An estimated value has been given for this test.

At elevated temperature, the MgO dispersed Mo alloy behaved different compared with alloy #697. It showed no jitters at high temperature. At fast displacement rate test the alloy showed high strength and slow displacement rate test showed lower strength, as would be expected consisting with the behavior at room temperature.

Typical tensile test specimens with optical and SEM pictures were shown from Figure 5.20 to Figure 5.23. SEM pictures showed a lot of round and small MgO particle sites, in which the MgO particles were pull out. No wide spread of microcracks were observed at the slower displacement rate. The microcracks were all located near the failure section as shown in Figure 5.21.

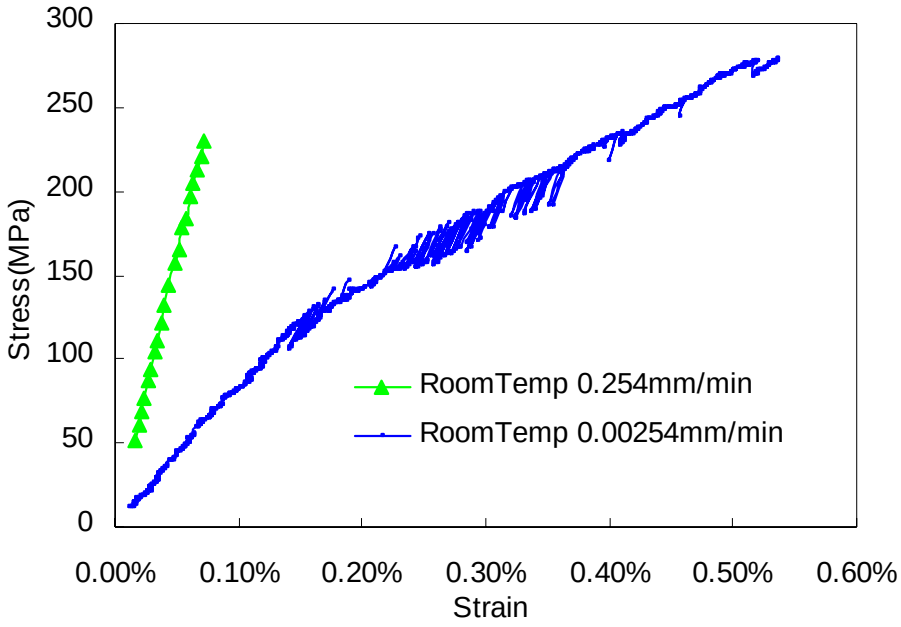

a. At room temperature

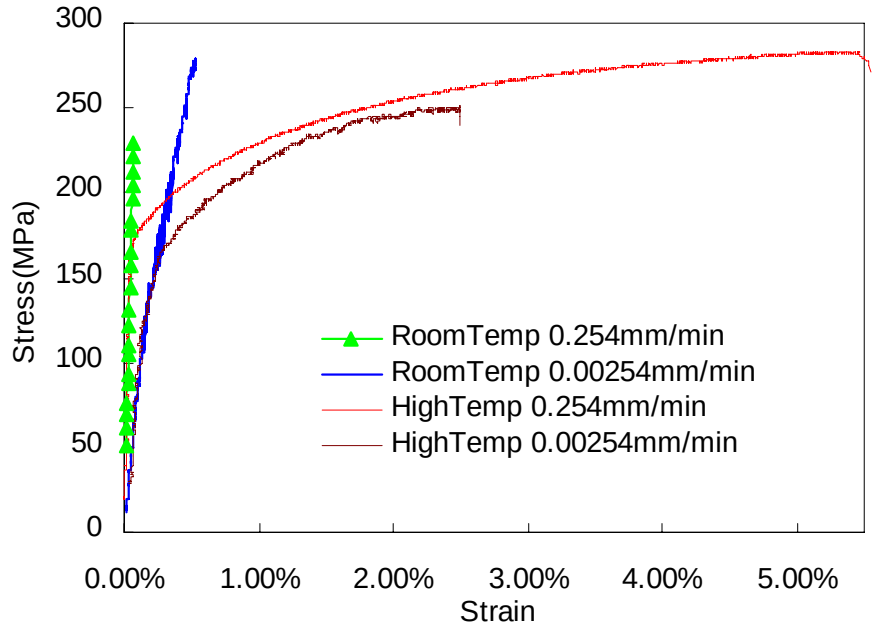

b. At room temperature and 650°C

Figure 5.19 Engineering stress-strain curves of alloy #698

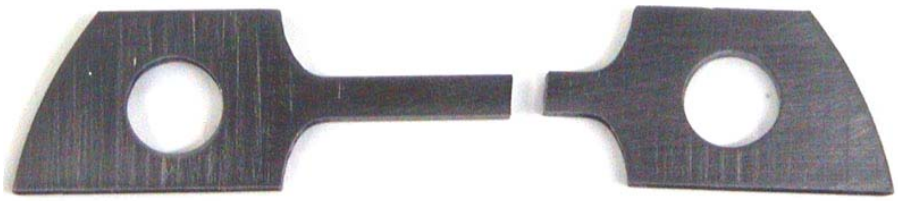

a. tested specimen

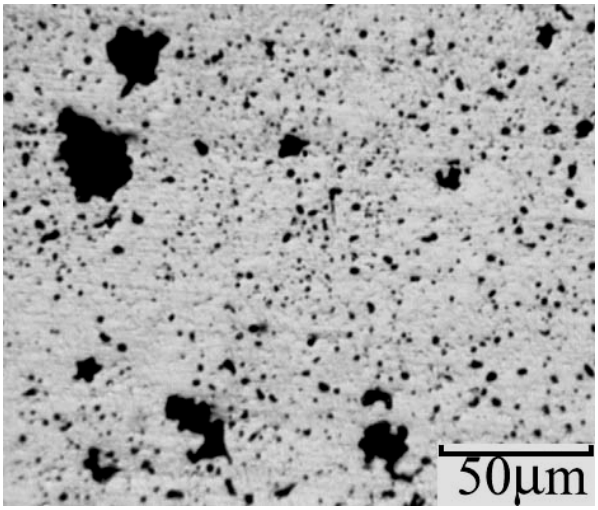

b. surface condition

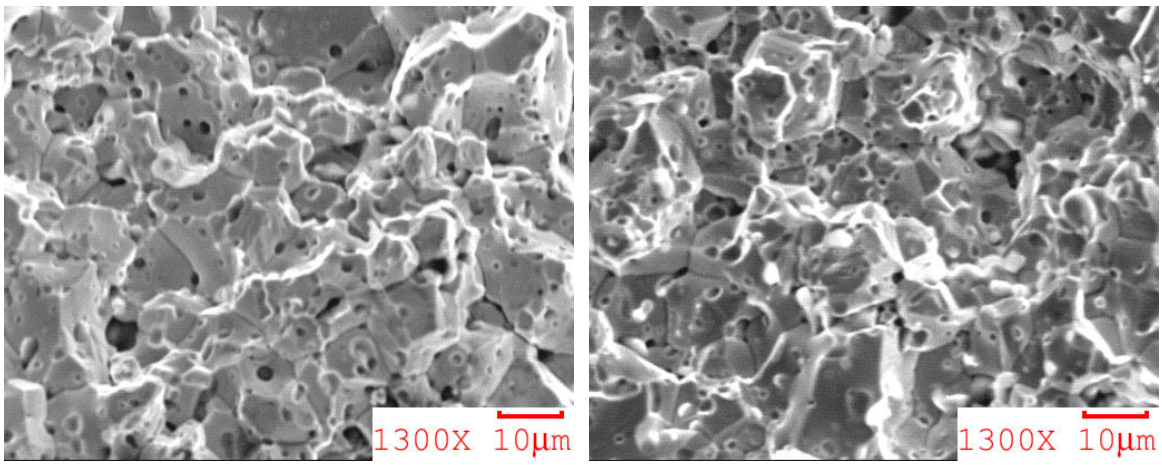

Near Edge Near Center

c. SEM fracture surface

Figure 5.20 Room temperature fast displacement rate broken specimen

a. tested specimen

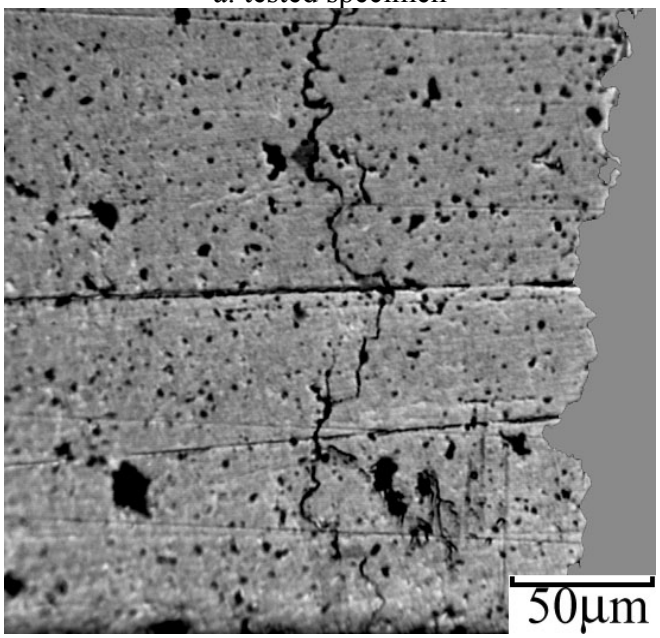

b. surface condition: Microcracks found near the failure section

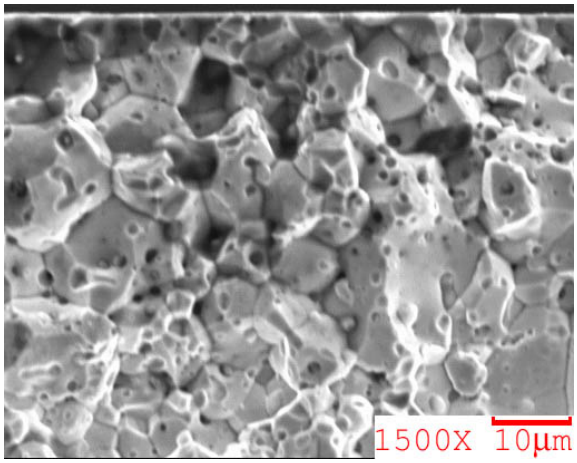

Near Edge

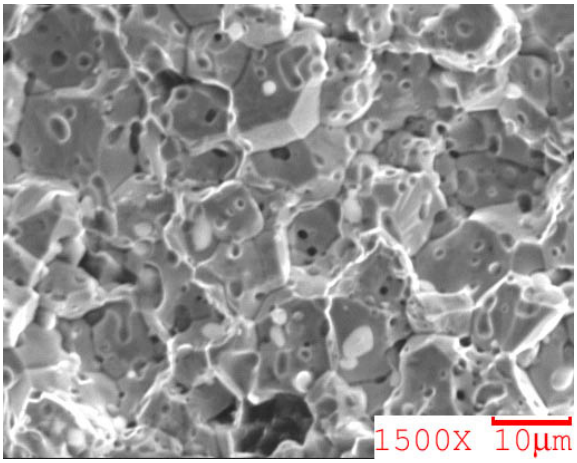

Near Center

c. SEM fracture surface

Figure 5.21 Room temperature slow displacement rate broken specimen

a. tested specimen

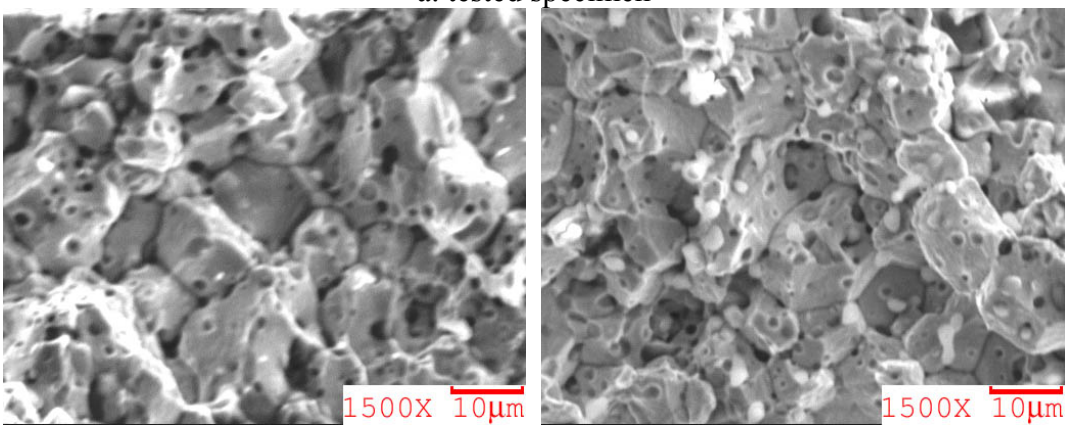

b. SEM fracture surface

Figure 5.22 High temperature fast displacement rate broken specimen

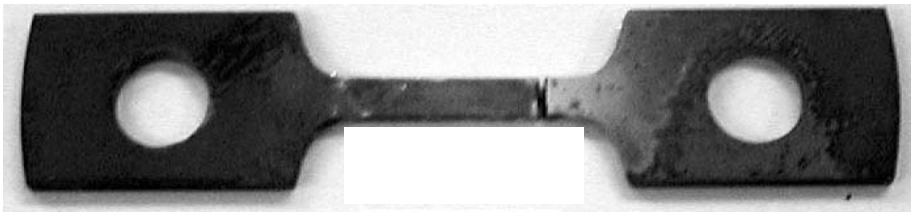

a. tested specimen

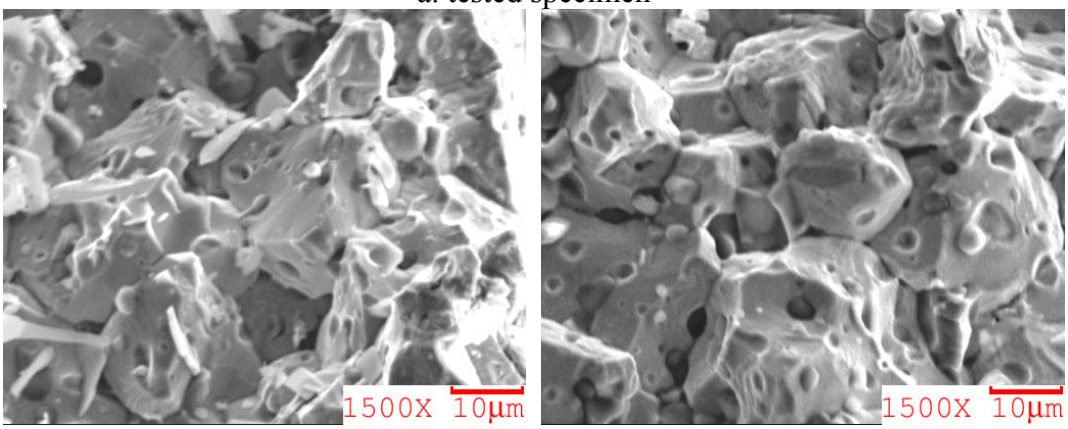

Near Edge Near Center

b. SEM fracture surface

Figure 5.23 High temperature slow displacement rate broken specimen

5.2.4 Results of thermo-mechanical properties

Table 5.2 showed the measured material thermo-mechanical properties. The test results showed a negative effect of the large spinel particles on the Mo alloys. However, as shown in Figure 5.24, drastic room temperature ductility was found on alloy #678 which has similar volume fraction of spinel particles as that of alloy #696 but with longer processing time (hot pressed for 4 hours). We also conducted room temperature bending tests of alloys #696 and #697 and the test results showed brittle failure characteristics, similar to the tension test results.

Table 5.2 Thermomechanical properties
(TC = Thermal Cycle, RM= Room Temperature)

ID	**0.254mm/min**				**0.00254mm/min**			
	Young's Modulus (GPa)		Ultimate Strength (MPa)		**Young's Modulus** (GPa)		**Ultimate Strength** (MPa)	
	RM	650°C	RM	650°C	RM	650°C	RM	650°C
#695	243	260	402	263	210*	-----	430	-----
#697	189	139	276	212	184	200	327	252
	120** (TC)	-----	150-197 (TC)	-----	120** (TC)	-----	150-197 (TC)	-----
#698	317	317	230	283	115	112	278	251

*Estimated value
**After thermal cycles, material has been damaged.

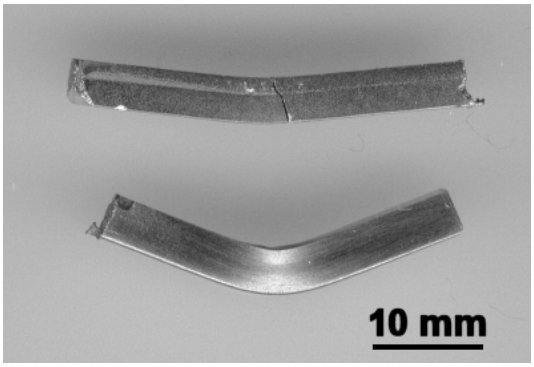

Top: Mo Bottom: Mo-3.4 wt% $MgAl_2O_4$
Figure 5.24 Comparison of the bending ductility[11]

5.2.5 Thermal cycle effects on tensile testing results

Thermal cycling effects were studied for alloys #697 and #678. For each alloy, three small pieces were prepared with 1, 10 and 20 thermal cycles respectively. As shown in

Figure 5.25, specimens were first heated to 650°C with a 250°C/min heating rate, held for 5 minutes at 650°C and then air cooled to room temperature.

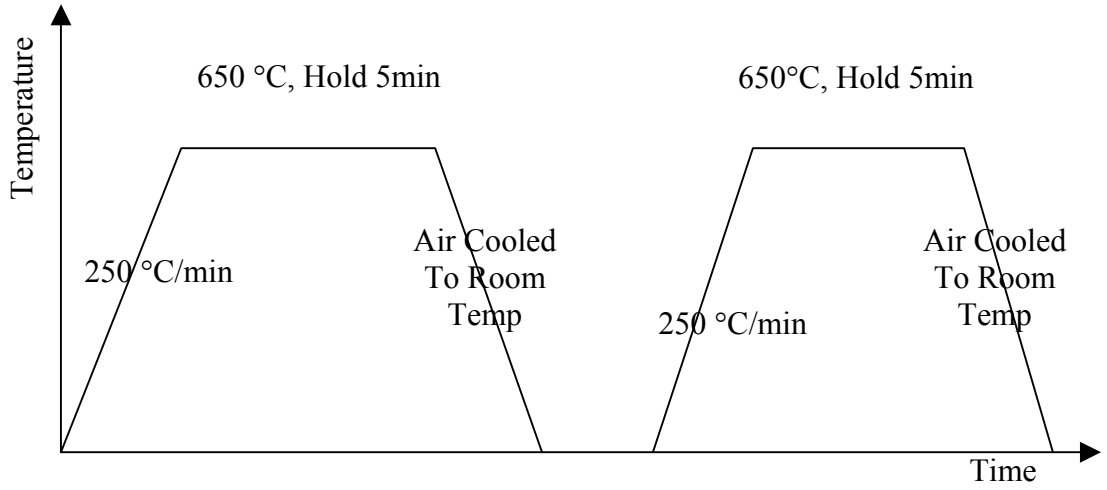

Figure 5.25 Thermal cycle scheme

A significant amount of thermally induced microcracks was observed in alloy #697 after 20 thermal cycles and these microcracks are all generated at the sites of larger spinel particles, as typically shown in Figure 5.26. However, no thermally induced microcracks have been found in alloy #678, as shown in Figure 5.27. Furthermore, as shown in Figure 5.12(a), three #697 specimens were first subjected to thermal cycles prior to tensile tests. As shown in Figure 5.12(a) and Table 5.2, specimens with thermal cycles showed lower failure strength, irrespective of the displacement rates.

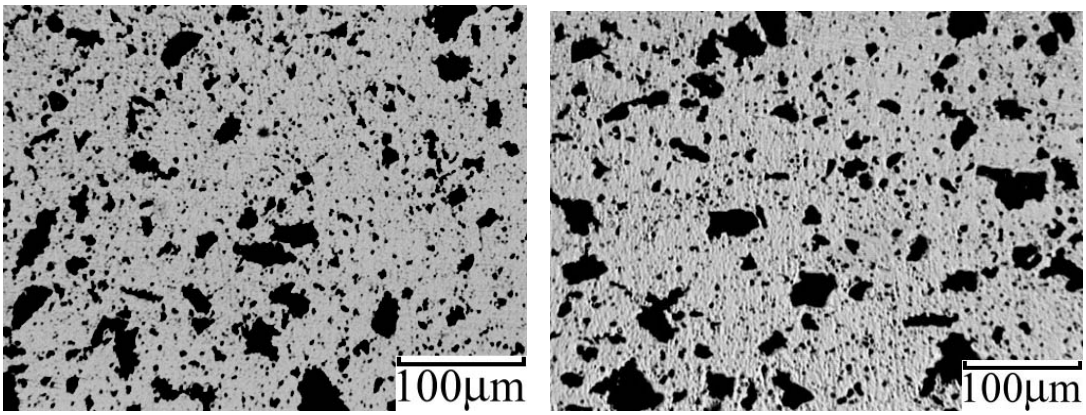

Before TC 1 TC

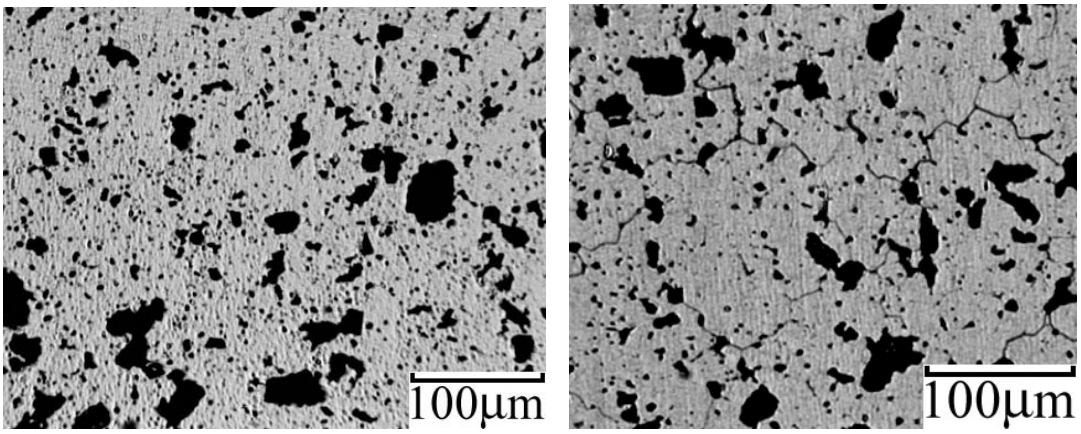

10 TC 20TC

Figure 5.26 Alloy #697: thermal cycle induced micro-cracks

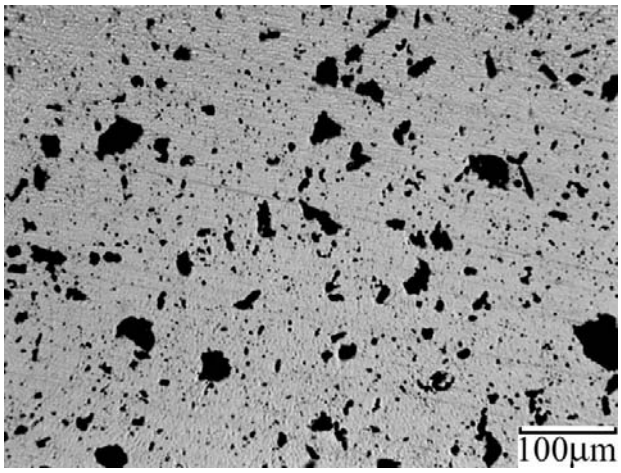

1, 10 and 20 thermal cycle: No microcracks observed

Figure 5.27 Alloy #678 thermal cycle effect

5.2.6 Microstructure analysis

Mechanical properties, thermal cycle effects are all related to the microstructure of these alloys, which includes grain structure and size, dispersed particle size and distribution. For each alloy, a sample of R & Z series were prepared to study the grain structure and particle distribution.

5.2.6.1 Microstructure evaluation

Microstructural examination was carried out by optical microscopy as well as scanning electron microscopy. In comparing these pictures, it should be kept in mind that their scale markers may be different. The phases (MgO and Spinel particles) were identified by a combination of energy dispersive spectroscopy(EDS) equipped with the

SEM. Images were typically obtained in the backscattered electron (BSE) mode in order to get particle distribution analysis.

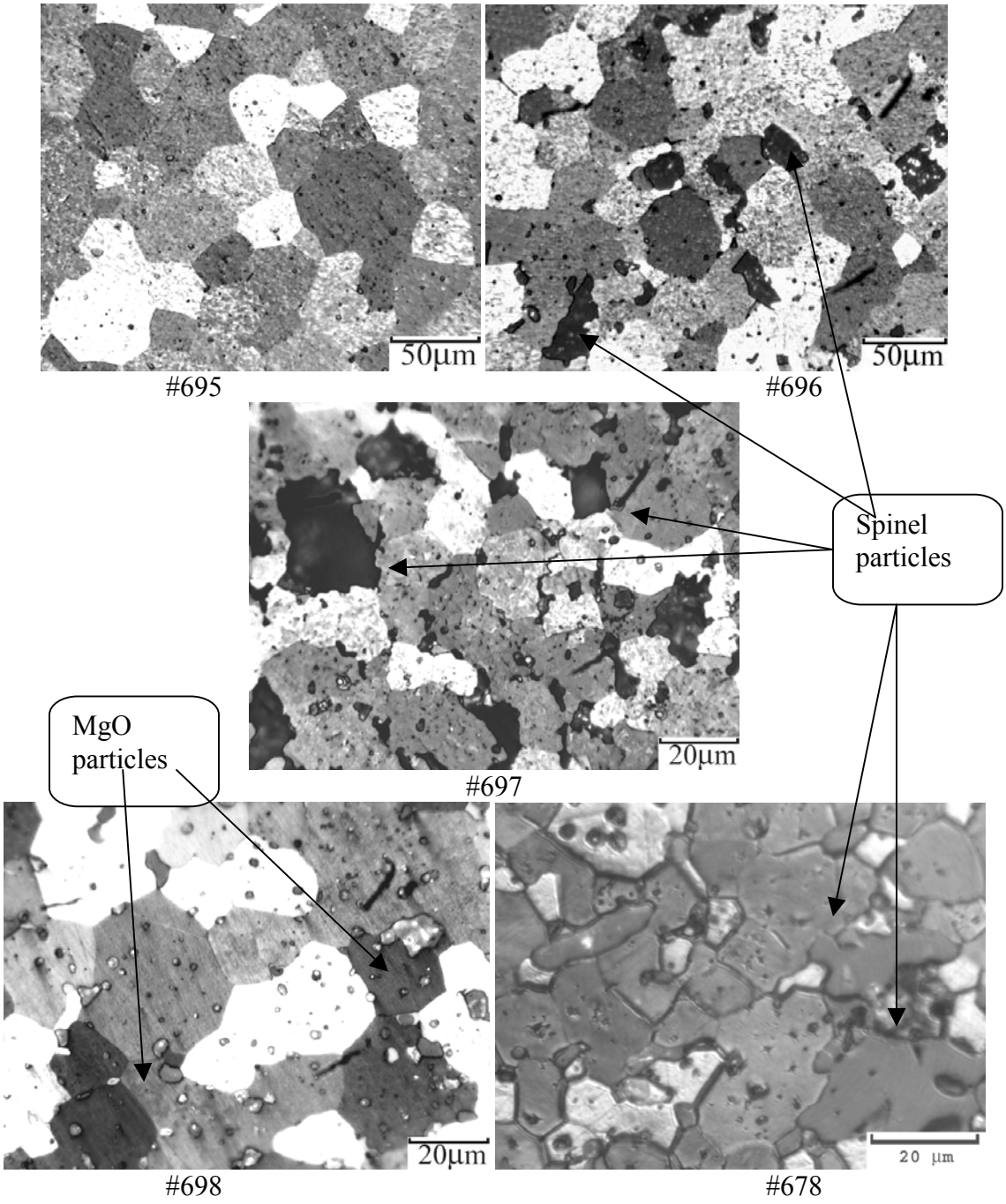

Figure 5.28 Optical Micrograph

5.2.6.2 Particle distribution

For particle distribution analysis, backscattered electron (BSE) images were used. Re-write Eq. (3-5) here, for each particle, square root of the area were used as the characteristic particle size. Figure 5.29 to Figure 5.32 show the particle picture and particle size distribution.

$$p(x) = \frac{Total\_number\_of\_particle\_size \le x}{Total\_number\_of\_particles} \qquad (5\text{-}2) \quad / (5\text{-}5)$$

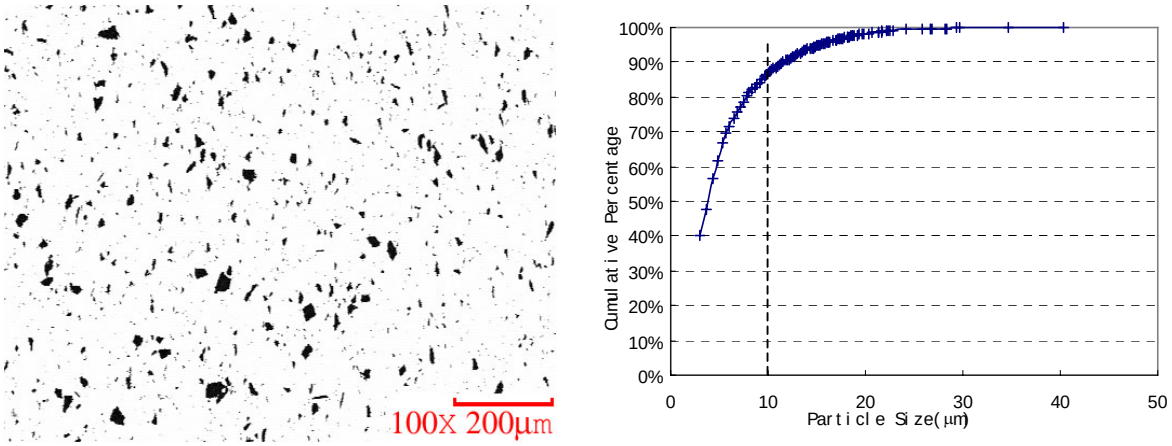

Figure 5.29 Typical spinel particle size and distribution for alloy #696

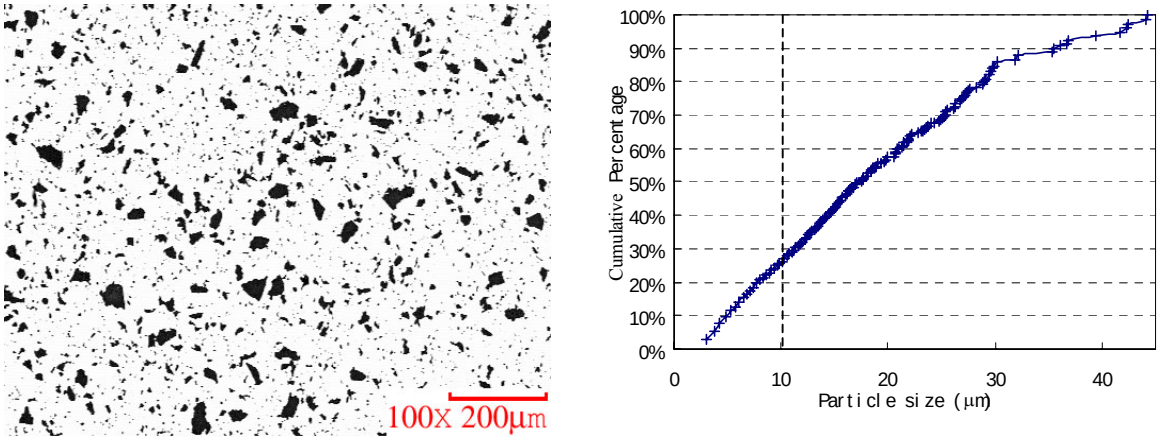

Figure 5.30 Typical spinel particle size and distribution for alloy #697

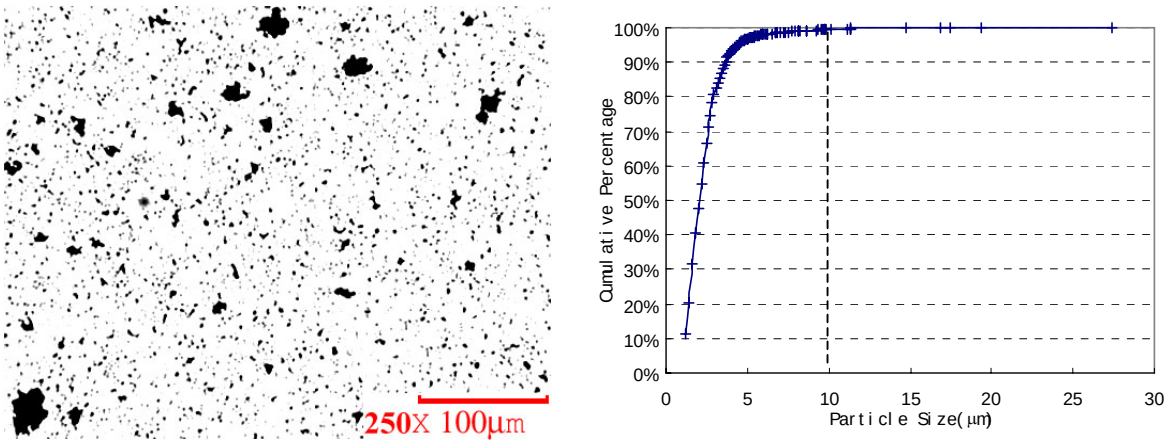

Figure 5.31 Typical spinel particle size and distribution for alloy #698

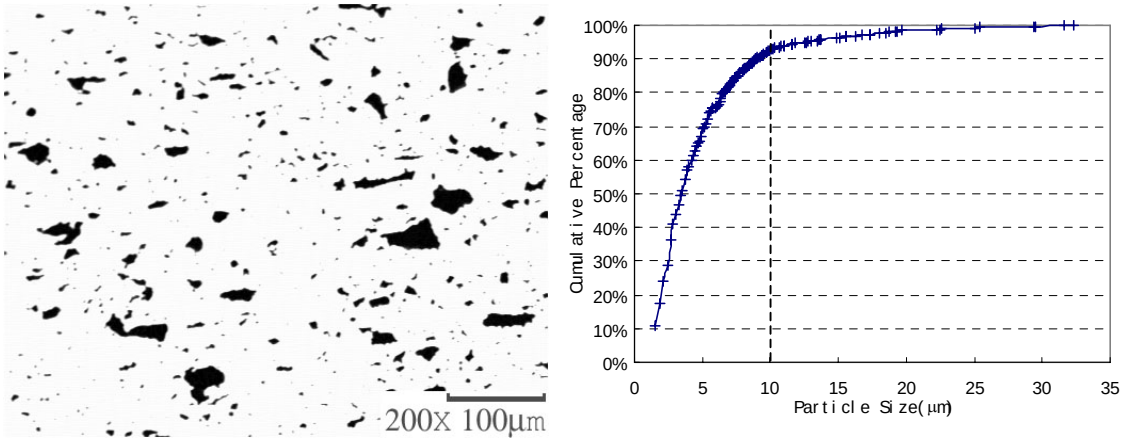

Figure 5.32 Typical spinel particle size and distribution for alloy #678

As shown in Figure 5.29 to Figure 5.32, alloy #696 has 85% spinel particles no larger than 10 µm, alloy #697 has 25% and alloy #678 has over 90%. It clearly showed #678 has finest particle, and #697 is the worst. Detailed inspection for alloy #696, it was found that some area of this alloy has large particle in the order of millimeter scale and that make this material not comparable with alloy #678. And also the processing time is different for these two alloys. It could be concluded that longer processing time and finer particle distribution may give better alloy performance if correlated these factors to the tensile test results.

Figure 5.31 showed alloy #698 (Mo-3%MgO) has uniform particle distribution and fine particles except for very few larger particles. Detailed microscopic study revealed that it has smaller and rounder particles compared to alloys #697 and #678. No

wide spread of microcracks were observed at the slower loading rate. The microcracks were all located near the failure section, as shown in room temperature slow displacement rate tensile test (Figure 5.21(b)). This should explain why alloy #698 showed more ductility.

5.3 Thermal expansion tests and microstructural analysis

The molybdenum base alloys which were subjected to coefficient of thermal expansion test and thermo-cycling tests were polished to study the metallographic changes after the tests, by which a suitable alloy can be developed which has good thermo-mechanical properties and long work life in the use of high temperature applications.

5.3.1 Coefficient of Thermal Expansion Using TMA 2940

The coefficient of thermal expansion (CTE) is one of the most important thermal property of the material, which is used in high temperature application, as the material must have low value of thermal expansion, because as the temperature increases the material must not expand on a large scale as it will hinder the long term usage of the material, where the dimensions of the material are important. The molybdenum base alloys were tested for the coefficient of thermal expansion (CTE). The working conditions and results are discussed. For the use of TMA in measuring the CTE value, the test specimen should be between 2 and 10 mm in length and shall not exceed 10 mm in lateral dimension and the specimen must be flat on both ends. The specimens were prepared using Electrical Discharge Machining (EDM) CNC-10A, as the alloys have metallic nature of bonding. After the machining was done the specimens were cleaned in acetone and then air dried before conducting the tests. After the tests [26], the specimens were polished again for post mortem microstructure analysis.

The following shows the typical testing conditions:

Universal Analysis
TA Instruments Thermal Analysis -- TMA Standard
Force 0.050 N
Equilibrate at 30.00 ^{o}C
Ramp 10.00 ^{o}C/min to 250.00 ^{o}C

Ramp 10.00 ^{o}C/min to 500.00 ^{o}C
Ramp 10.00 ^{o}C/min to 750.00 ^{o}C
Ramp 10.00 ^{o}C/min to 1000.00 ^{o}C

5.3.2 Thermal expansion test for alloy # 648

Due to the constraint in availability of this material only three tests were carried out, thus forming a standard test pattern to maintain consistency for all the other alloys.

Table 5.3 Parameters of the CTE test on Molybdenum #648

	TEST 1*	TEST 2	TEST 3
SAMPLE	MO	MO	MO
SIZE	2.7862mm	3.3185mm	2.9220mm
CELL CONSTANT	1.0000	1.0000	1.0000
METHOD	MOTEST	MOTEST	MOTEST

* Flow rate of argon was 100cc/min.

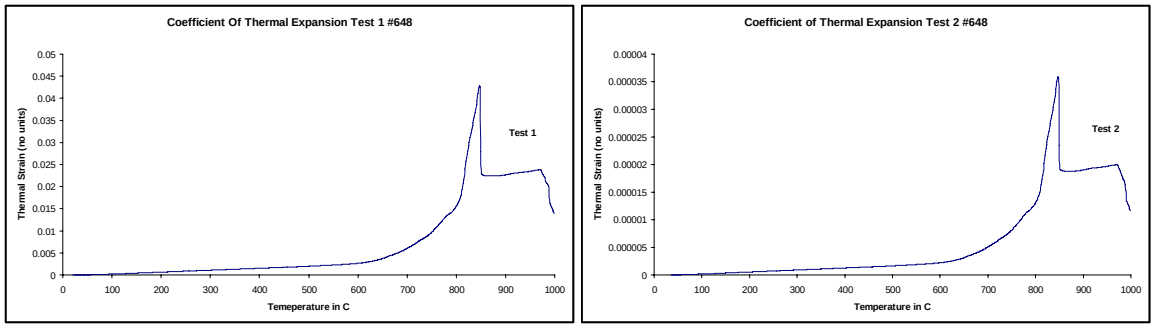

(a) Test 1 (b) Test 2

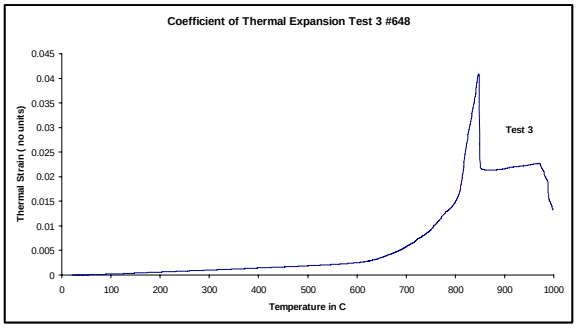

(c) Test 3

Figure 5.33 Coefficient of thermal expansion of molybdenum #648

5.3.3 Thermal expansion test for alloy # 649

Table 5.4 Parameters of the CTE test on Molybdenum Silicide 649

	TEST 1	TEST 2	TEST 3
SAMPLE	MOSI	MOSI	MOSI
SIZE	4.1036	3.6092	4.7702
CELL CONSTANT	1.0000	1.0000	1.0000
METHOD	MOSITEST	MOSITEST	MOSITEST

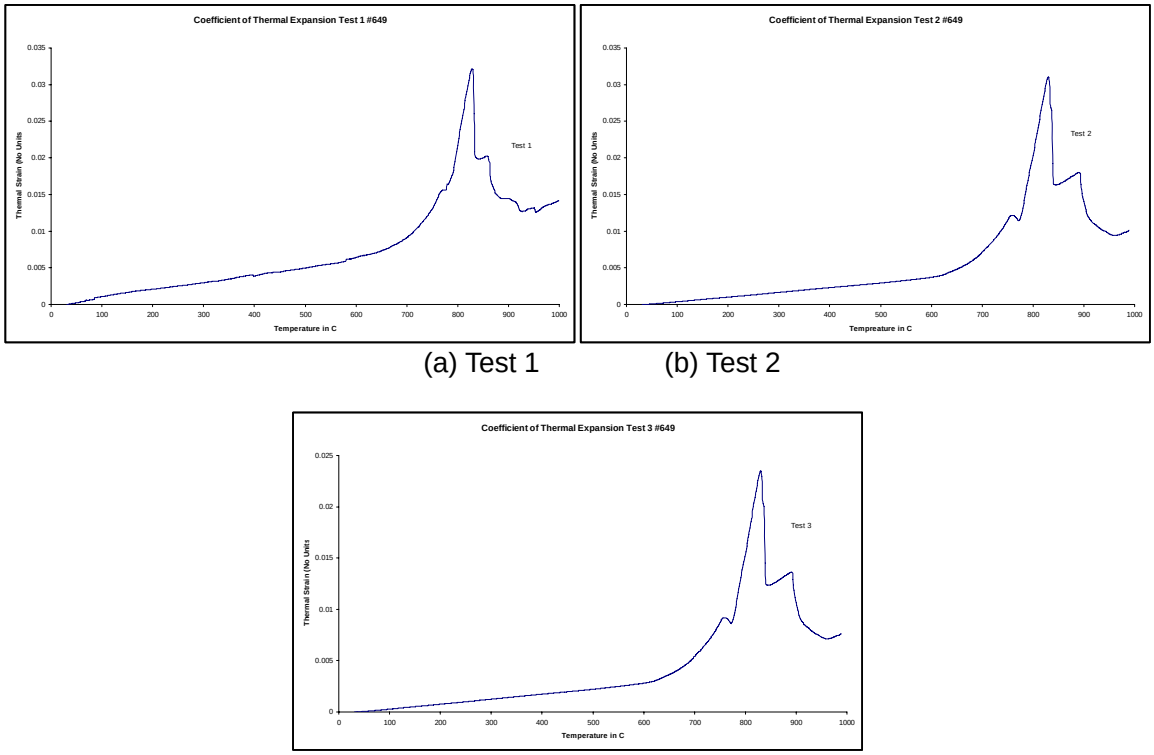

(a) Test 1 (b) Test 2

(c) Test 3

Figure 5.34 Coefficient of thermal expansion of molybdenum silicide #649

5.3.4 Thermal expansion test for alloy # 677

Table 5.5 Parameters of the CTE test on Molybdenum 677

	TEST 1	TEST 2	TEST 3
SAMPLE	MO	MO	MO
SIZE	3.5742	2.9840	3.5210
CELL CONSTANT	1.0000	1.0000	1.0000
METHOD	MOTEST	MOTEST	MOTEST

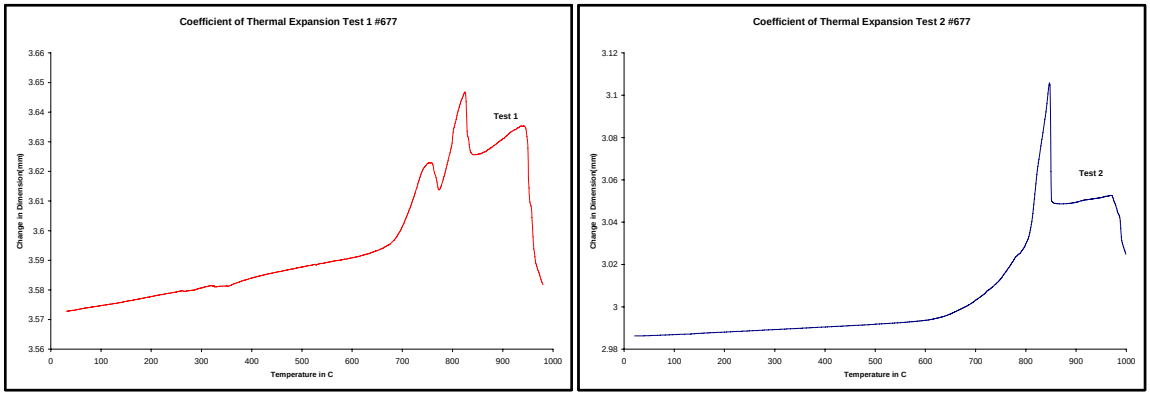

(a) Test 1 (b) Test 2

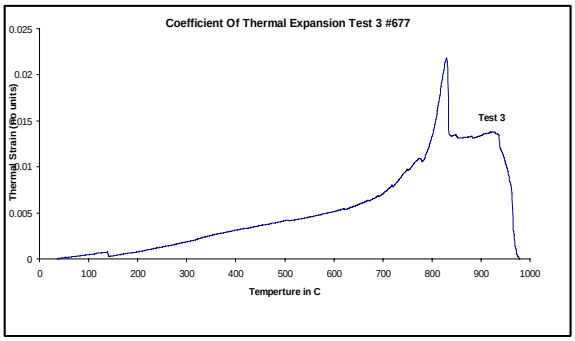

(c) Test 3

Figure 5.35 Coefficient of thermal expansion of molybdenum #677

5.3.5 Thermal expansion test for alloy # 678

Table 5.6 Parameters of the CTE test on Molybdenum-Spinel 678

	TEST 1	TEST 2	TEST 3
SAMPLE	MO-MgAl2O4	MO-MgAl2O4	MO-MgAl2O4
SIZE	3.8366	2.8429	4.0121
CELL CONSTANT	1.0000	1.0000	1.0000
METHOD	MoSpinel	MoSpinel	MoSpinel

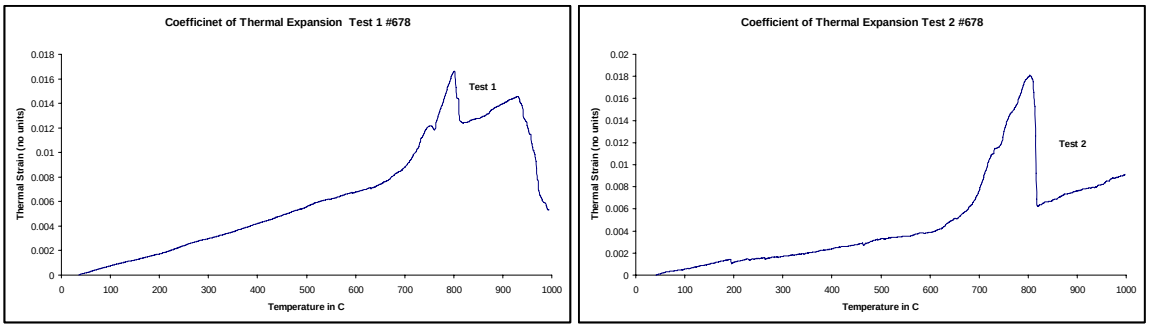

(a) Test 1 (b) Test 2

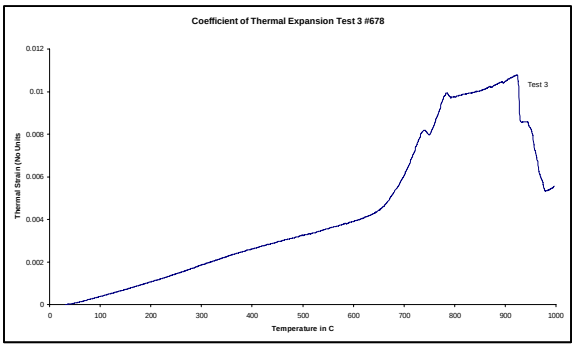

(c) Test 3

Figure 5.36 Coefficient of thermal expansion of molybdenum-spinel #678

5.3.6 Thermal expansion test for alloy # 697

Only one test was done on #697, the parameters were listed below:

Sample: Spinel
Size: 3.8366 mm
Cell Constant: 1.0000

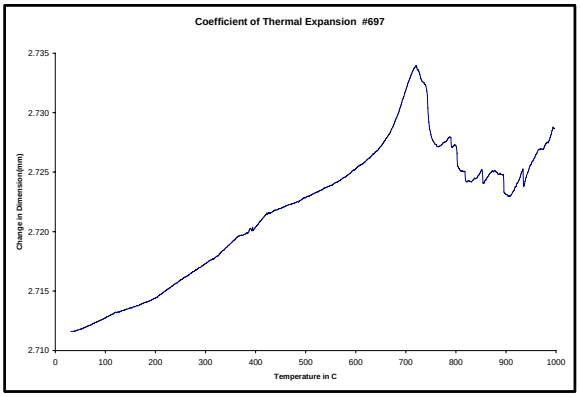

Figure 5.37 Coefficient of thermal expansion of molybdenum-spinel #697

Table 5.7 Coefficient of thermal expansion values of alloys Using TMA

Condition (Temperature)	COEFFICIENT OF THERMAL EXPANSION (µm/m^{o}C)				
	Molybdenum #648	**Moly Silicide #649**	**Molybdenum #677**	**Molybdenum-Spinel #678**	**Molybdenum-Spinel #697**
50	4.93	3.16	4.55	4.88	5.78
100	5.56	6.23	4.83	6.55	8.25
150	7.98	6.24	6.41	6.94	5.08
200	6.683	6.28	6.541	7.22	9.19
250	6.65	6.34	6.58	7.77	10.9
300	6.63	6.63	6.2	7.97	10.9
350	7.04	6.66	6.69	8.17	14.5
400	6.60	6.41	6.7	6.42	13.8
450	7.10	6.02	6.875	6.81	6.16
500	9.88	6.58	9.54	5.64	7.83
550	9.49	7.56	9.65	7.24	7.84
600	9.82	8.82	10.0	7.11	12.3
650	14.5*	28.9*	18.5*	17.2*	20.0*
700	35.78*	60.1*	104.0*	47.8*	46.5*
750	49.26*	106.0*	35.8*	10.5*	-95.5**
800	178.3*	359*	262.0*	4.51*	-52.2**
850	248.5*	-892.0**	9.36*	6.71*	-6.08**
900	79.73*	-242.1**	37.5*	10.3*	-36.3**
950	-349.82**	-38.2**	-613.0**	-77.3**	34.3**
1000		2.03*	-166.0**	15.9*	30.3**

***** Due to the formation of molybdenum oxide (MoO_2) which accumulates over the specimen surface thereby increasing the CTE value drastically [16].
****** Around a temperature range of 750-850^{o}C formation of molybdenum oxide (MoO_3) which is very volatile in nature reduces the specimen thickness thus we have negative CTE value [16].

5.3.7 Discussion of the TMA testing results

5.3.7.1 Alloy #648

Using the TMA 2940 tests, the CTE values of all the alloys under consideration were determined. The first and the foremost question which arises is that, the coefficient of thermal expansion appeared to be nonlinear, i.e. the data and graphs obtained from the tests don't resemble any linearity after certain temperature. The nonlinearity may be due to the oxidation process of Molybdenum, silicon and spinel materials [16]. The molybdenum, around 700-800^{o}C oxidizes to form molybdenum oxide (MoO_2), which is stable and accumulates over the parent material at around 700-800^{o}C, hence the sudden peak i.e., the sudden increase of the TMA data as shown in Figures 5.33 to Figure 5.37. Furthermore, as the temperature crosses 850^{o}C the molybdenum oxide (MoO_2) oxidizes changed to MoO_3 [16], which is volatile in nature and thus it evaporates and leaves the substrate molybdenum surface exposed to the environment, this causes the sudden drop in the curve i.e., the dimension of the specimen decreases abruptly. Now, another layer of molybdenum oxide (first MoO_2 and then quickly changed to MoO_3) is gradually building up as temperature continued to increase and hence the second peak observed. It should be noted that although Argon gas was supplied through the furnace to maintain an oxidizing-free atmosphere during the TMA test. The flow which was maintained around 100 cc/min for the first test may not be able to prevent the presence of residual oxygen in the test chamber. The maximum flow of 150 cc/min, which can be provided with the equipment, was tried out and similar results were obtained.

5.3.7.2 Alloy #649

The CTE graph of molybdenum silicide shows the similar pattern as that of the molybdenum around the same temperature range, but small peak was observed, which is caused by the oxidization of the silicon particle present in the alloy. First the silicon particle gets oxidized to form silicon oxide (SiO) subsequently forming SiO_2. The oxide which is formed is gaseous in nature thus forming a non-protective smoke rather than a continuous and protective SiO_2 film. The subsequent temperature increase temperature starts the oxidizing of molybdenum substrate. Thus the formation of silicon oxide reduces the thermal expansion coefficient of the alloy.

5.3.7.3 Alloy #677

The Thermal expansion coefficient value of the pure molybdenum #677 has the same peak around 700-800^{o}C was because of the oxidation of molybdenum forming molybdenum oxide. But the value of thermal expansion coefficient between them differs because of the method of processing the material. The #648 was cast whereas the #677 was hot pressed from the molybdenum powder and followed by heat treatment. The casting has some voids and porosity as shown in the Figure 5.38, causes the change in the CTE value.

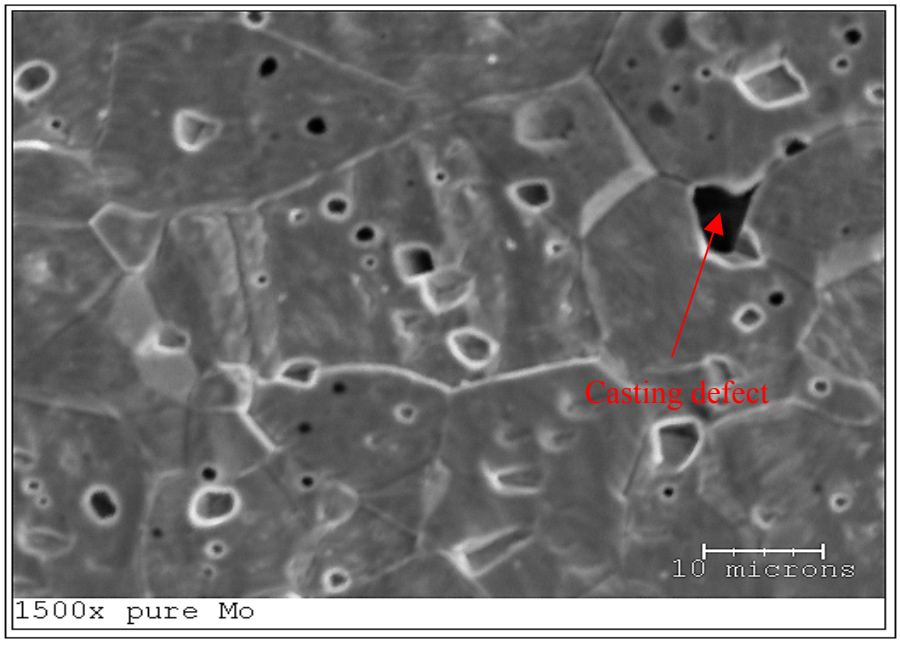

Figure 5.38 Micrograph of #648 showing defects due to casting

5.3.7.4 Alloy #678

The thermal expansion of the molybdenum spinel follows the same pattern like other alloys considered, whereas many small peaks were observed. This can be well explained by considering the alloying agent in this material like molybdenum as the base with aluminum, magnesium and oxygen as the alloying agent. The spinel ($MgAl_2O_4$) particle which has a high thermal coefficient expands depending upon the particle size since they are distributed in the same volume fraction and size. Temperature reaching around 700-800^{o}C, the molybdenum starts oxidizing. The importance of adding the spinel particle can be seen when the temperature is around 400^{o}C as they tend to decrease the

value of the expansion coefficient of the material because of the utilization of increase in temperature by them.

5.3.7.5 Alloy #697

Due to problems in machining of this material, the test was concluded with only one successful completion. In this particular material, lots of peaks was observed after 750^{o}C because the material while processing by hot pressing process was maintained at 1800^{o}C for only 1 hour, thus leaving only very less time for tight bonding between the alloying agents, hence the temperature increases the reaction between the alloying agents starts especially between the bigger spinel particle and the base material.

Comparing the two molybdenum-spinel alloys (#678 and #697) for their thermal expansion values. The Figure 5.39 shows that #678 has higher CTE value than the #697, which may because of two reasons (i) the composition of spinel ($MgAl_2O_4$) particle is more in #697 than #678 and (ii) the processing time for them is also different.

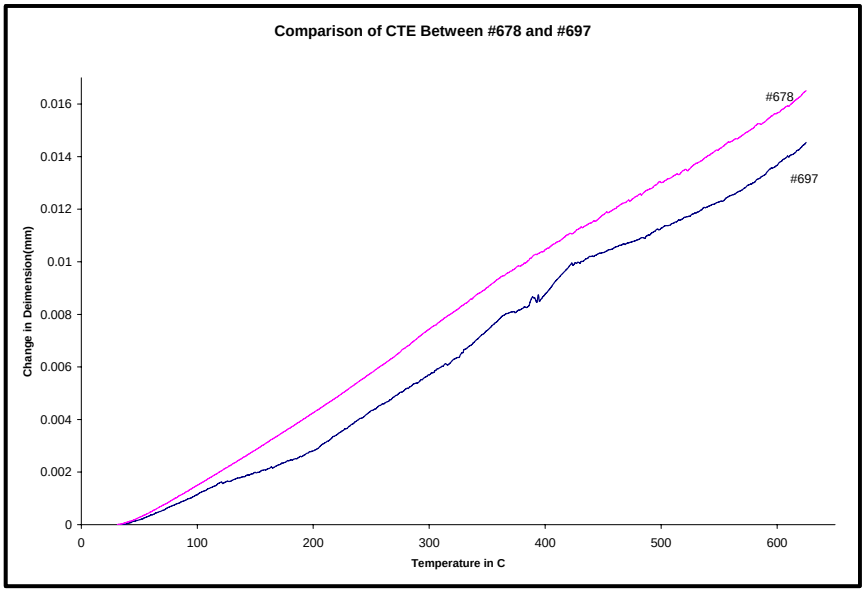

Figure 5.39 Comparison of coefficient of thermal expansion between #678 and #697

5.3.8 Thermo-Cycling Tests

The thermo cycling tests were conducted to determine if failure by thermal stresses may occur. Alloy #678 and #697 were considered in this investigation. Three specimens of each molybdenum-spinel material were considered. Each specimen was cut

using the EDM CNC 10-A. for each thermal cycle, the specimen was heated in a furnace up to 650°C, maintained at 650°C for 5 minutes, and then allowed to air cooled. For each alloy, three specimens were used to conduct 1, 10 and 20 cycles [20]. After the tests, the specimens were ground using SiC papers and polished down to 0.5 microns using diamond suspension polishing agent. Post mortem microstructural analyses were investigated using Scanning Electron Microscope (SEM) and Energy Dispersive Spectroscopy (EDS).

5.3.8.1 Alloy #678

After the end of the thermo-cycling cycling tests the molybdenum-spinel (#678) showed some characteristics, which are explained with the help of the SEM micrographs shown below. At the end of the first cycle, due to the energy supplied, spinel particles in the molybdenum matrix were expanded and then contracted and thus may form a small interfacial gap between the spinel and molybdenum matrix as shown in Figure 5.40. Gap formation at different locations was observed.

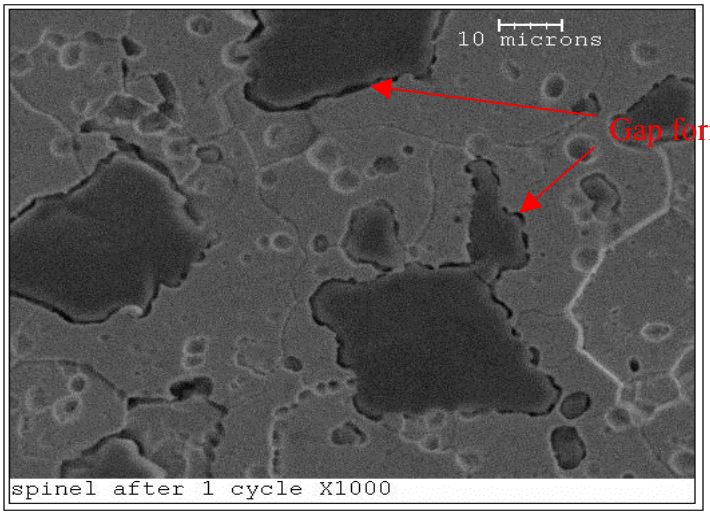

Figure 5.40 The SEM picture showing the gaps created after 1 thermo-cycle in Mo-$MgAl_2O_4$ between the Molybdenum and the Spinel particle

After ten thermal cycles, the spinel particles, which were expanded and contracted repeatedly, may generate microcracks originated from the interfacial gap as shown in Figures 5.41. These microcracks are generally seen near the larger spinel particles.

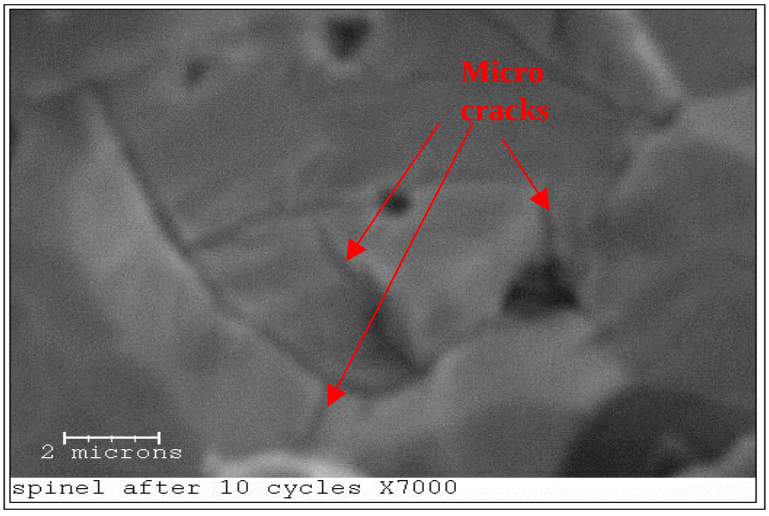

Figure 5.41 Micro-cracks and its propagation from MgAl2O4 towards the Mo

After twenty thermal cycles, spinel particles induced more stress on the molybdenum matrix and due to the mismatch of coefficient of thermal expansion, more interfacial microcracks as shown in Figure 5.42 were observed. However, the opposite was observed, i.e. the interfacial microcracks were gone. This phenomenon may be attributed to the repeated thermo cycles such that the molybdenum matrix also expanded and thus closed these interfacial microcracks.

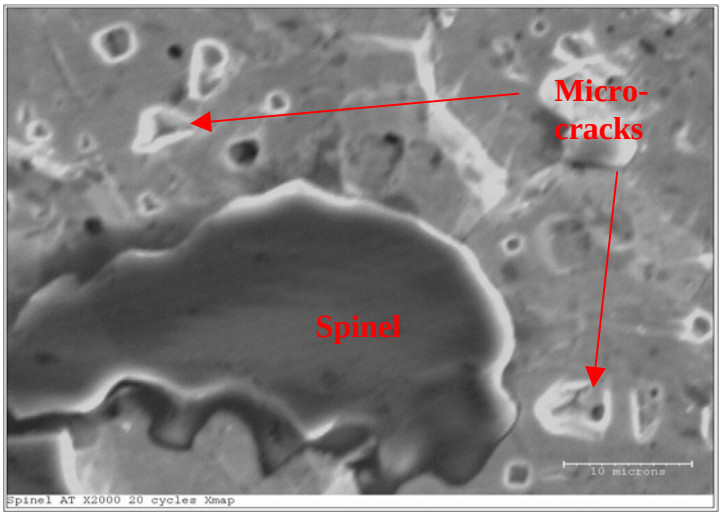

Figure 5.42 Micro-cracks near the big spinel particle

5.3.8.2 Alloy #697

After the first cycle as well as ten cycles, there was not much significant changes seen in the microstructure, whereas after twenty thermal cycles, substantial microcracks were seen starting from the spinel particles, propagating through the molybdenum matrix grain boundaries, and linking one spinel to its neighboring spinel particles. The cracks can be seen very clearly using an optical microscope.

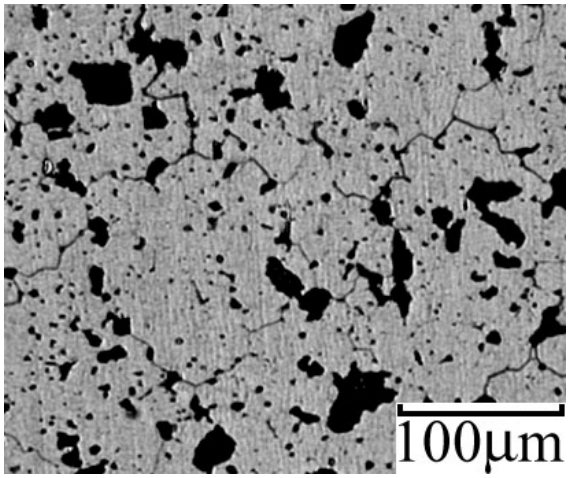

Figure 5.43 Cracks observed using optical microscope after 20 thermal cycles

5.3.8.3 Comparison of Alloy #678 and #697

Comparing #678 and #697, the #678 showed more resistant to thermo-cycling than #697. This is because the spinel particle distribution in #678 is more even when compared to that of #697 and also the hot pressing time of the #678 was maintained at the 1800^{o}C high temperature for four hours while #697 was maintained at 1800^{o}C for only one hour. In summary, processing method and the uniform dispersing of the spinel particle distribution are important factors that correspond to the thermo-mechanical property evaluation.

5.4 Thermal cycling tests and microstructure analysis

For this research, thermal cycling tests at temperature of 650°C and 1000°C were performed. A series of post-mortem microstructure evaluation were conducted using X-ray diffraction (XRD), SEM backscattered electron detection mode, Qualitative Energy Dispersive Spectroscopy techniques on SEM, and Standardless Quantitative Analysis with Phi-Rho-Z method. Microstructure analysis was carried out on all specimens.

5.4.1 Alloy #697 (Mo-6wt% $MgAl_2O_4$)

For alloy #697, X-ray diffraction (XRD) method is first used to verify the MoO_2 and MoO_3 phases. The XRD patterns are shown in Figure 5.44 and Figure 5.45 below.

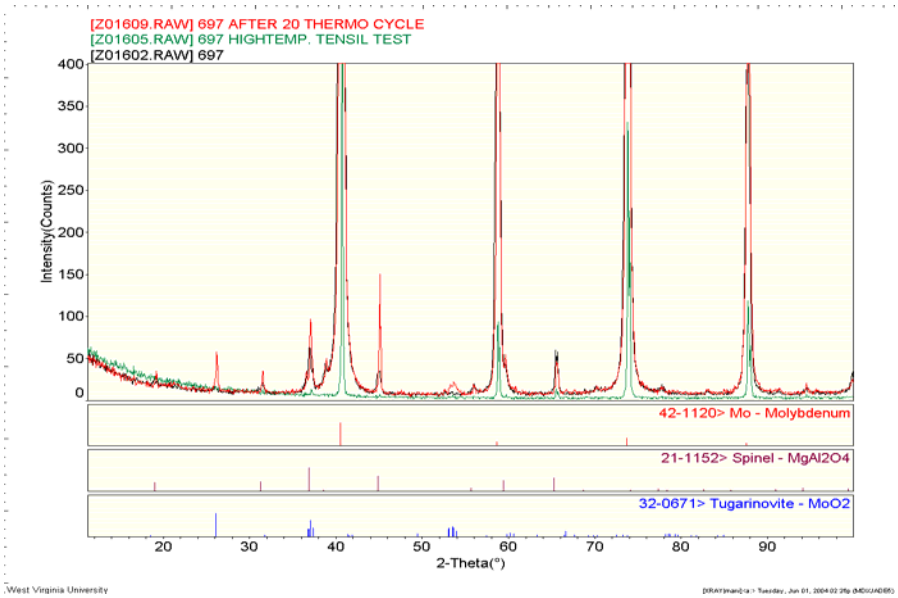

Figure 5.44 XRD patterns (MoO_2 identified)

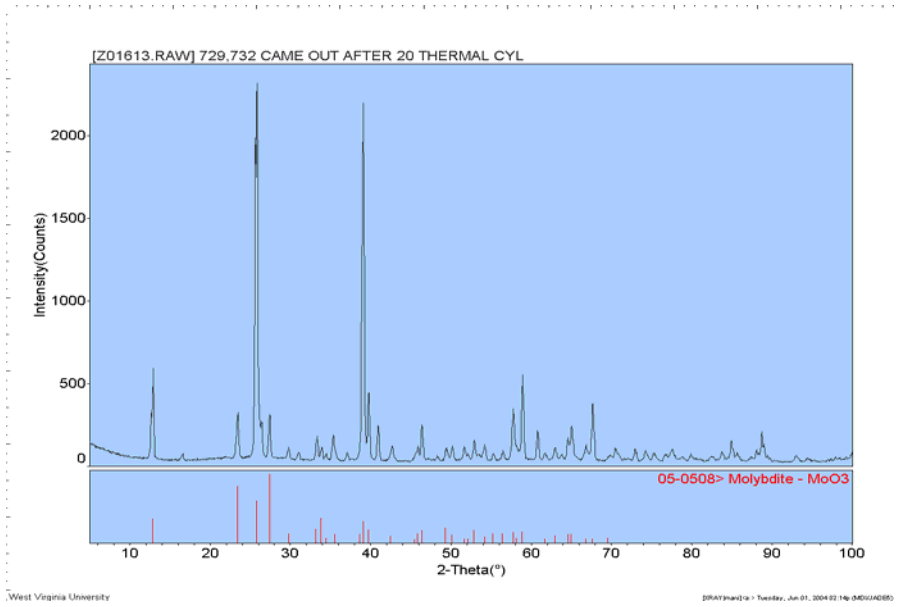

Figure 5.45 XRD patterns (MoO_3 identified)

Micro-cracking was observed for alloy #697. These surface micro-cracks are very obvious and could easily be detected under optical microscope. As shown in Figure 5.46,

further examination using SEM reveals that most surface cracking originated from large spinel site. These cracks eventually extend to another spinel site.

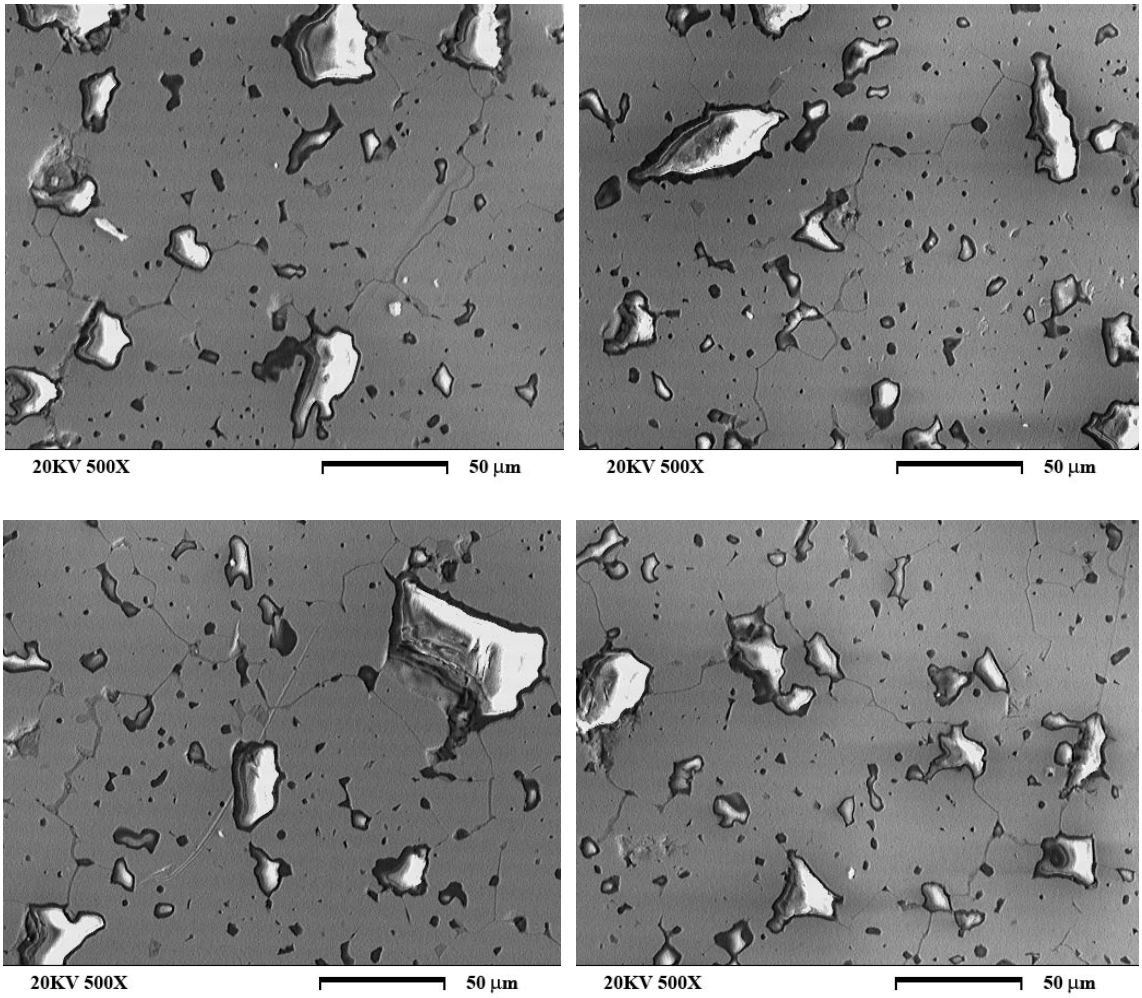

Figure 5.46 Surface micro-crack of Alloy #697.

Due to thermal expansion mismatch between matrix and spinel dispersion, significant levels of residual stresses are induced during thermal cycling. Since the thermal expansion of Molybdenum is less than that of the spinel substrates, degradation of mechanical properties is significant. These local stresses would hinder the dislocation flow, and so decreasing the plactic deformation. Micro-cracking would then be initiated from the spinel inclusion. Crack would like to extend to free surface. Thus extension of micro-cracks from spinel to another spinel particle is observed.

It is also important to note that the formation of gap between spinel particles and the matrix after thermal cycling (Figure 5.47). The spinel as local notches, when expand

would creates gap during thermal treatment with its irragular particle shape. Micro-cracks are further extended due to this mechanism.

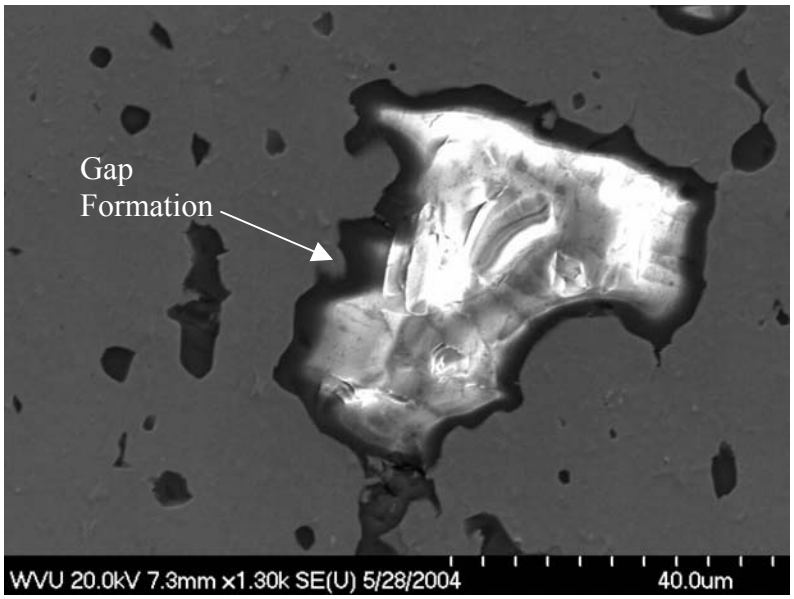

Figure 5.47 Gap formation in Alloy #697.

Suspected oxides sites were then identified using backscattered electron detection mode and Energy Dispersive Spectroscopy techniques on SEM. Standardless Quantitative Analysis with Phi-Rho-Z method was also used to determined the proportions of Molybdenum and Oxygen constituents (Figures 5.48 to 5.51).

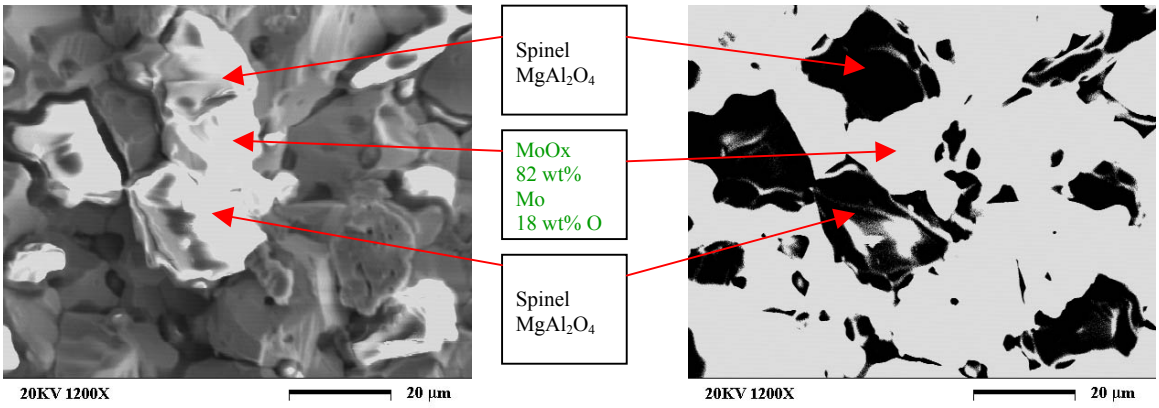

NOTE: Average Mo site contains 92 wt% Mo and 8 wt% O.

Figure 5.48 SE and BE micrographs of alloy #697

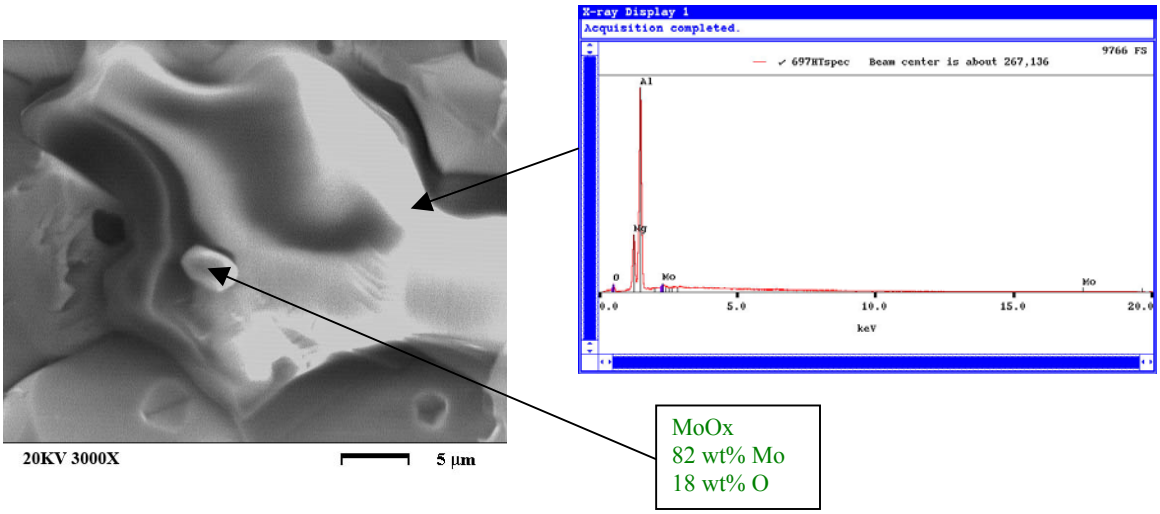

Figure 5.49 SE micrograph and EDS spectrum of alloy #697.

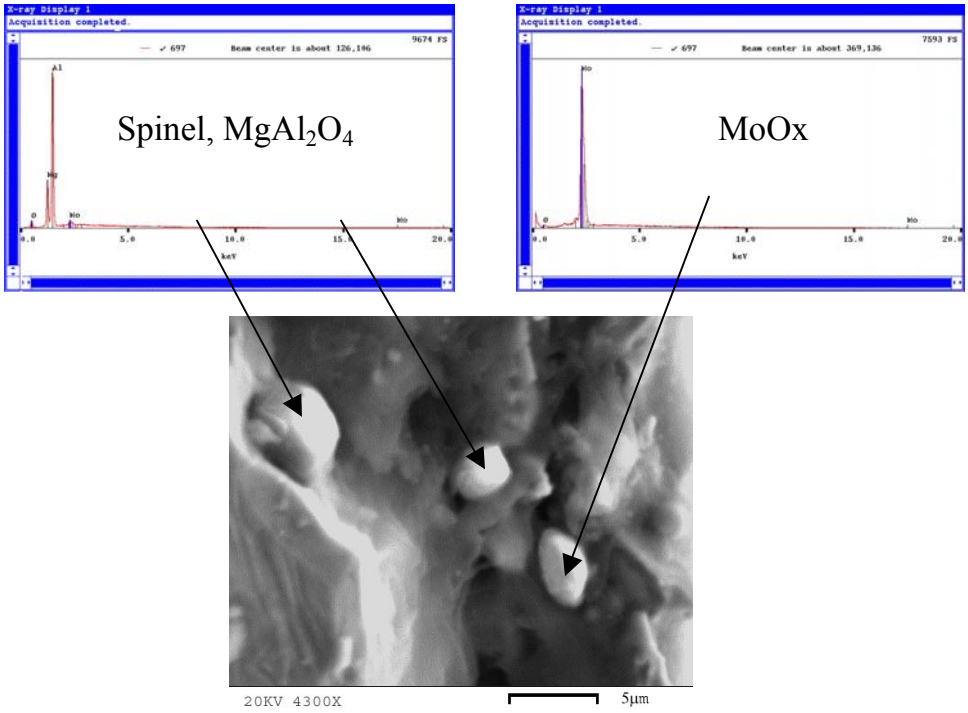

Figure 5.50 Alloy #697 after 20 Thermal Cycles.

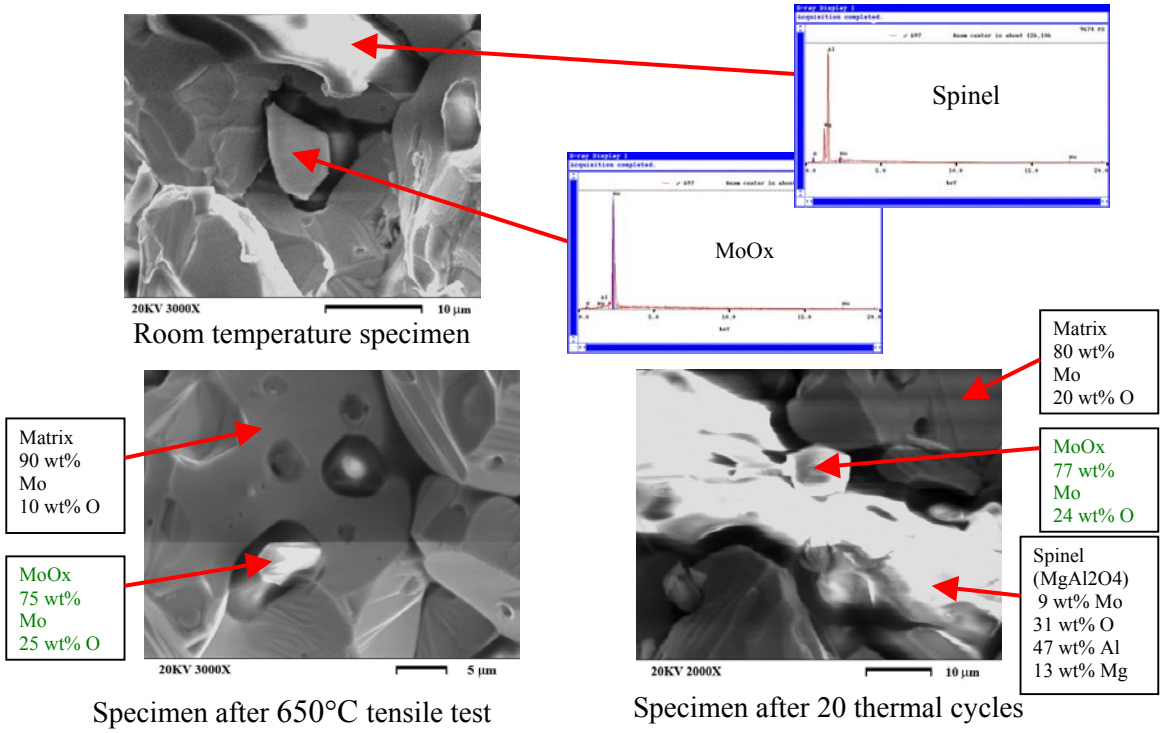

Figure 5.51 Alloy #697 under different testing conditions

The formation of Molybdenum oxide is not that easy to detect. Nevertheless, its formation can be seen mainly around and/or near spinel ($MgAl_2O_4$) particle.

5.4.2 Alloy #678 (Mo-3.4wt% $MgAl_2O_4$)

No surface micro-cracks were observed for all alloy #678 (Figure 5.52) after thermal cycling.

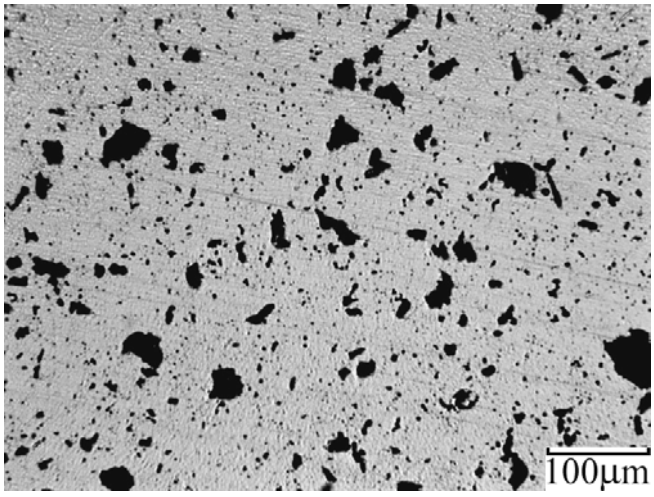

Figure 5.52 Alloy #678 under optical microscope showing none surface crack.

Although the formation of MoO_2 and MoO_3 were substantial for both alloys during heating, the formation of oxides for alloy #678 were not observed for all other tests. The finer spinel ($MgAl_2O_4$) particle size and even particle distribution contributed to the lesser formation of oxides. With finer particle, the oxygen getter effect of alloy #678 is not apparent and thus increases the ductility of this alloy.

Hypothetically, the formation of Molybdenum oxide should be observed in the entire tested alloys. From the microstructure standpoint, it's shown otherwise. For alloy #678, the dispersion of spinel particle is evenly distributed, and the particle size is considerably finer than for alloy #697. Thus, it is not possible to detect the present of Molybdenum oxide. Since the present of Molybdenum oxide cannot be detected, much can be said about the impurity precipitate to the matrix/spinel boundaries.

5.4.3 Alloy #732 (Mo-15wt% $MgAl_2O_4$)

Surface cracking of alloy #732 cannot be detected after 20 cycles of thermal cycling. Micro-cracking of alloy #732 is only visible when observed under high magnification SEM (Figures 5.53). Gap formation between spinel and Molybdenum matrix is also noted.

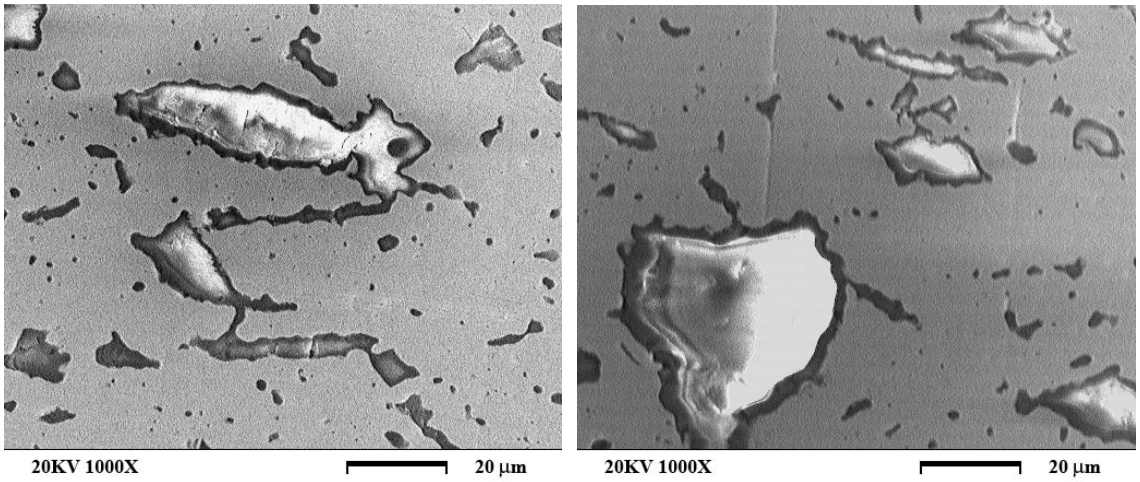

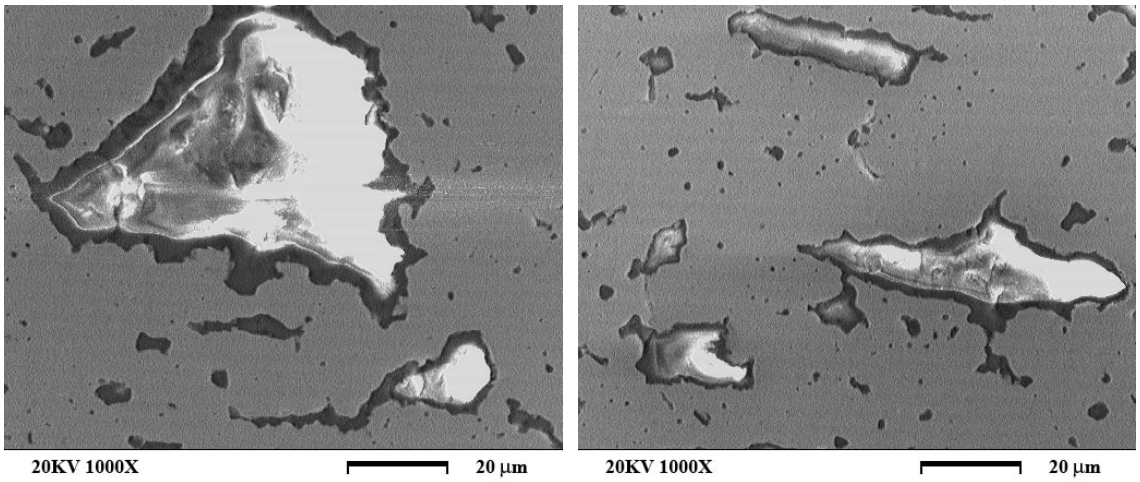

Figure 5.53 Micro-crack of alloy #732.

A possible explanation for this phenomenon is as follow. Although alloy #732 has more weight percentage of spinel particles (about 15wt%), and considerably larger spinel size compare to all the other alloys, alloy #732 has better spinel distribution (See chapter 3). Comparing with #678, one can see that the dispersed spinel distribution charts are almost identical. Therefore, one can say that alloy #732 would shows similar thermal mechanical properties as that of alloy #678. Simple bending test was done on alloy #732 and it did exhibit bend ductility.

Although there are no obvious surface cracking, the detrimental molybdenum oxide can be detected easily.

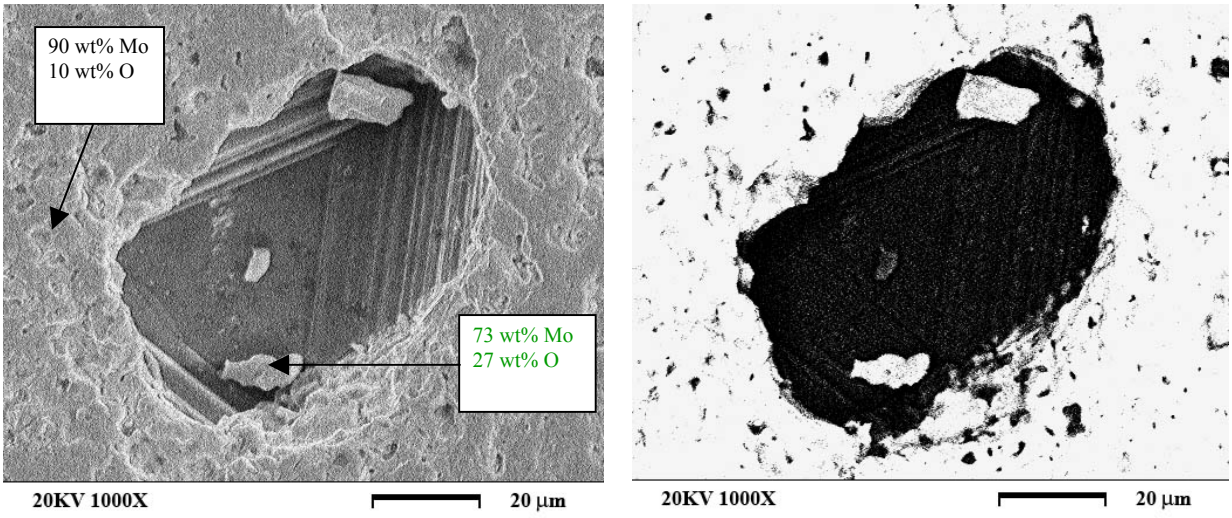

Figure 5.54 SE and BE micrograph of alloy #732.

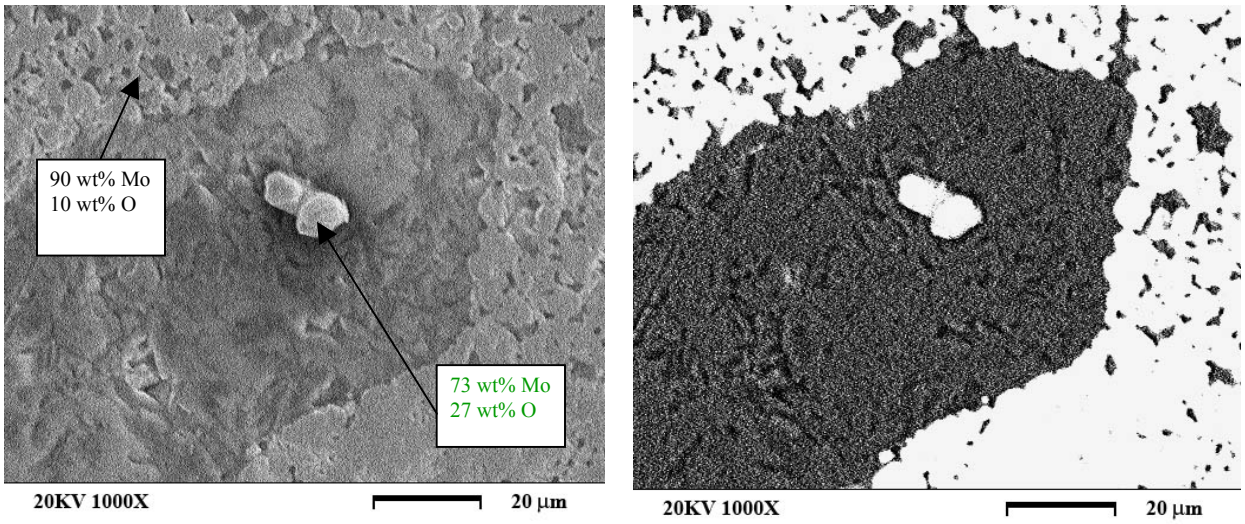

Figure 5.55 SE and BE micrograph of alloy #732.

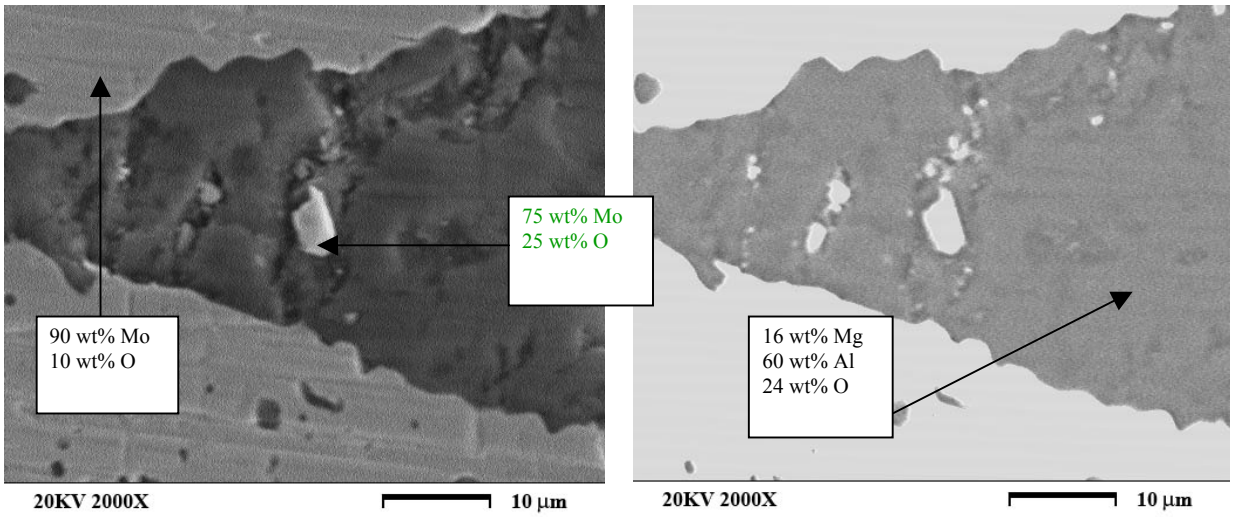

Figure 5.56 SE and BE micrograph of alloy #732.

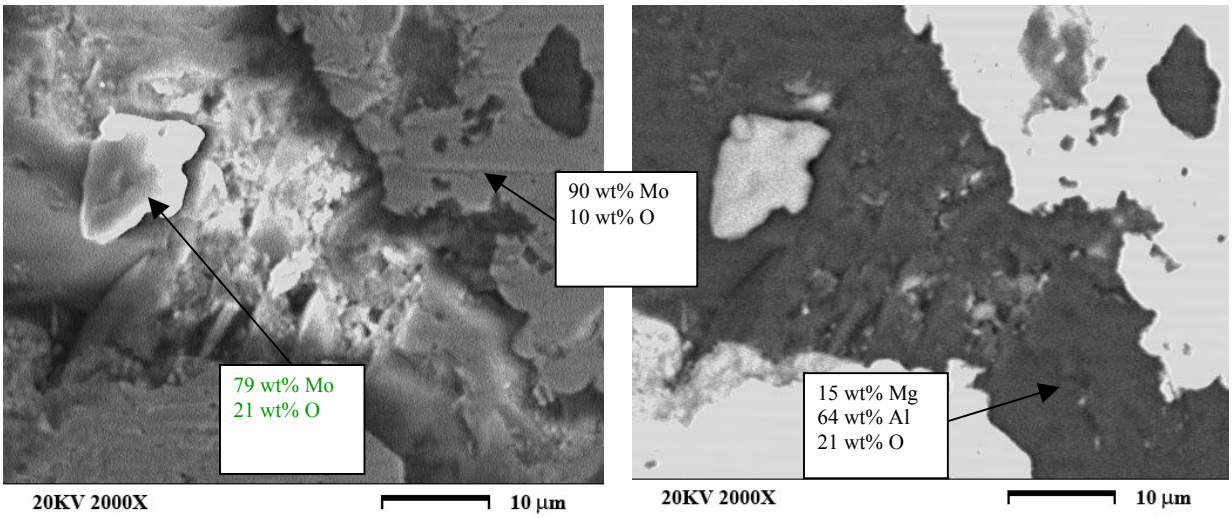

Figure 5.57 SE and BE micrograph of alloy #732.

5.4.4 Further Research Discussion

The process of dispersing spinel particles into Molybdenum alloy itself is already a strengthening mechanism. Still, different mechanical properties are observed even for similar alloys. Since it is an exceedingly complex process for polycrystalline structure, further explanation is needed.

The reduction in grain size can further strengthen the alloy. This is based on the fact that it is difficult for a dislocation to pass into another grain, especially if it is very misaligned. Usually, the yield strength varies with grain size *d* according to the Hall-Petch relationship [47]:

$$\sigma_{yield} = \sigma_o + k_y d^{-1/2}.$$

Thus, fine-grained alloys would have higher yield and tensile strength than large-grained alloys.

With reference to Figures 3.15 to 3.19 which shows typical spinel particle size and distribution for different test alloy, possible explanation can be made related to the mechanical properties of alloys. For alloy #678 and alloy #732, the distributions (Figure 3.15 and Figure 3.17) show that these alloys possessed a relative high amount of finer spinel particles. With smaller grain size, these dispersed particles would create many grain boundaries between matrixes and larger area of grain boundaries that impedes dislocation motion. Grain boundaries are then became barriers to slip, thus hinder the motion of dislocation and the alloys exhibit higher strength.

Vickers Indentation on alloy #732 were preformed and hardness value ranging from 231 HV to 272 HV in Vickers' scale depending on the location of the indenter on the matrix or around spinel particle (Figure 5.58).

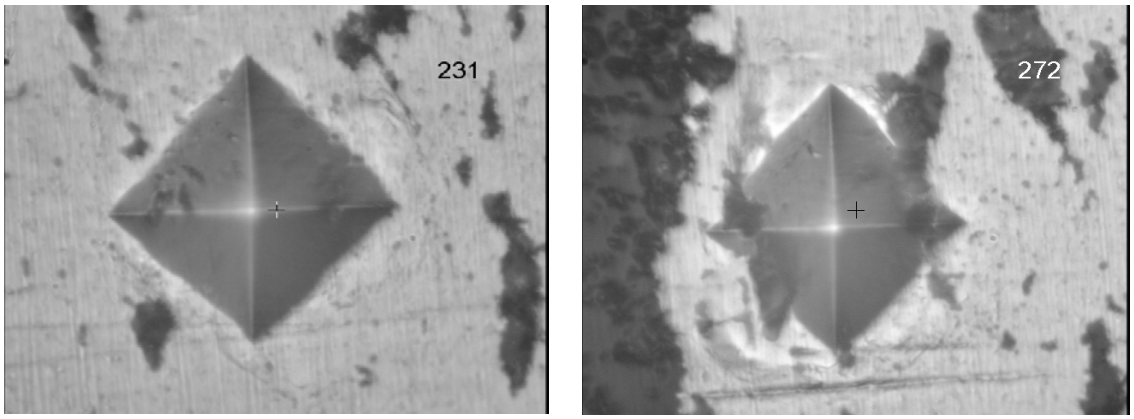

Figure 5.58 Indentation on alloy #732.

These values are much higher than typical metal alloy, which further verified the strength of this alloy.

Alloy #697 would have a linear distribution of dispersed spinel (Figure 3.16). These larger particles, which are half of the total particle distribution, combined with the thermal expansion mismatch between matrix and spinel, rendering the brittle behavior of this alloy.

5.4.4.1 Alloy #697 and Alloy #732

Although cracking and Molybdenum oxide were detected in alloy #697 and alloy #732, both alloys would provide different mechanical properties. The brittle behavior of alloy #697 and the bending ductile behavior of alloy #732, suggested that mechanism of mechanical behavior couldn't be explain in just one single event but contribution from many aspect.

SEM micrographs show evidence of formation of segregated, precipitated Molybdenum oxide near or around spinel dispersion and grain boundaries between metal and spinel oxide. This formation of Molybdenum oxide phase is the result of gettering of oxygen near spinel dispersion thus attract and precipitate volatile MoO_x phase. Every impurity introduced into a metal whether during initial processing or heat treatment has a certain level of solubility. When the process of precipitate is undergoing, the metal will

become supersaturated with that impurity and will seeks and achieves equilibrium by precipitating the excess impurity atoms into another phase of different composition or structure. The form of precipitate can be either coherent or incoherent with the surrounding matrix [48]. The coherent of oxygen impurities with the matrix can be seen from Figures 5.59 and 5.60 below showing X-ray mapping of alloy #697 and #732 after thermal cycling.

One can see that the oxygen is distributed in all matrix and not only on the spinel particle and around precipitate. Alloy #678 would show similar oxygen distribution.

For alloy #697, this Molybdenum oxide formation has large influence on the interface. It may cause the bonding between spinel particle and matrix to be weakened and therefore the alloy will have brittle failure when corresponding to mechanical loading. The larger spinel dispersion size also contributed to this behavior. The frequent spotting of detrimental impurities in alloy #697 suggested that this larger inclusion size would getter too much impurities and further embrittling the alloy.

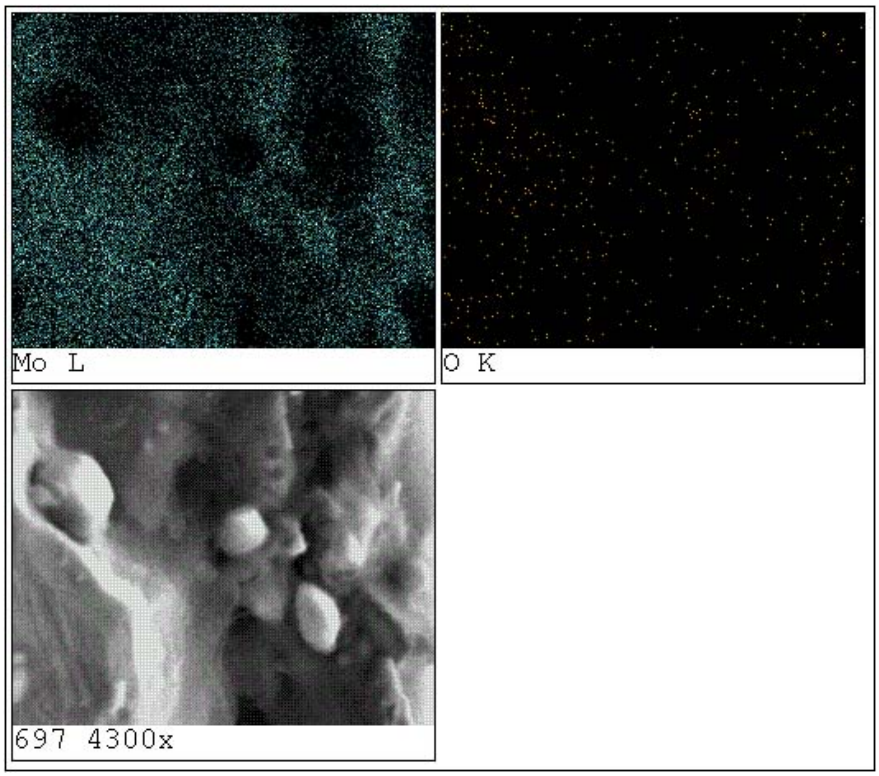

Figure 5.59 X-ray mapping of alloy #697.

Alloy #732 shows otherwise properties. The formation of detrimental impurities in or around spinel particle is much more stabilizing for this alloy. The fact is that alloy #732 shows bending ductility would prompt us to argue that the impurity precipitate for this alloy is much coherent to the matrix. This will in turn strengthen the bonding between matrix and spinel inclusion in stead of debonding it like in the case of alloy #697. Although smaller particle size will hinder dislocation which is necessary for plastic deformation in ductile metal, the better distribution of spinel dispersion would promote ductility than brittleness. With finer distribution of spinel particle in Molybdenum matrix, the obstacle, which is the spinel, on the dislocation would be balanced out by another spinel particle due to their distance apart. It is also suggested that the spinel inclusion would be better mechanically tolerated by alloy #732 than #697. In addition, only microcracks but not surface cracks were observed. This suggested that the propagation of crack is halt by hindering of dislocation flow.

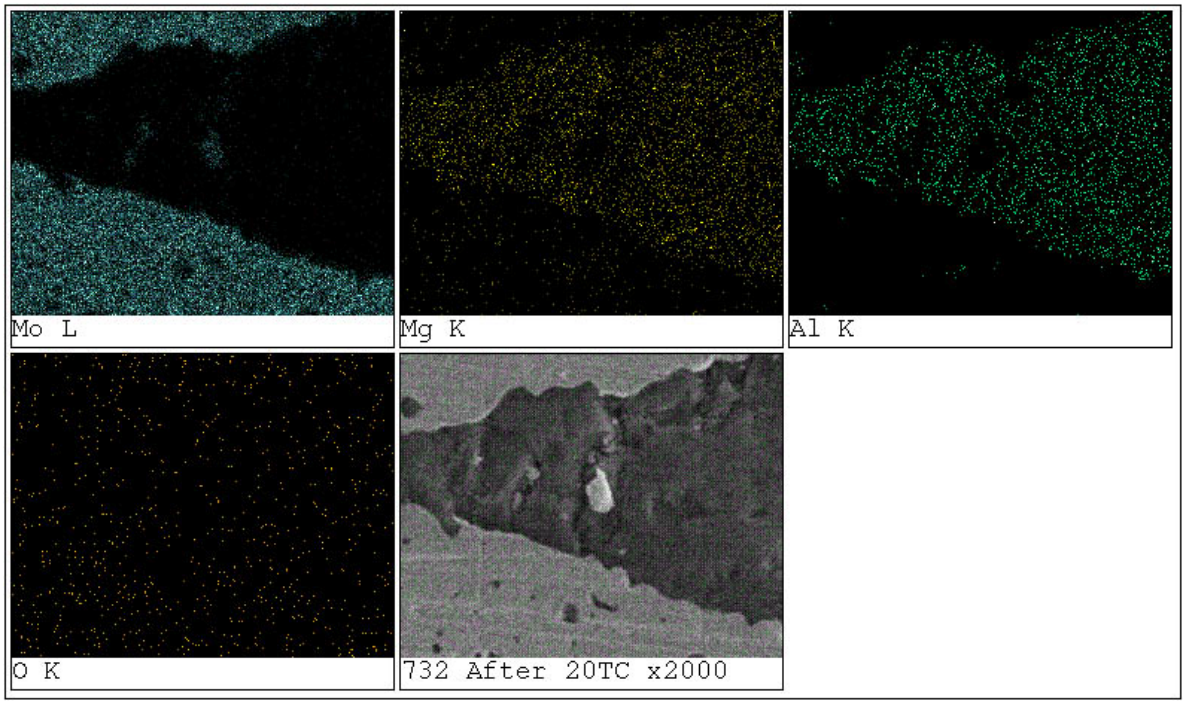

Figure 5.60 X-ray mapping of alloy #732.

5.5 Atomistic simulations

The results of atomistic simulations and discussions were in Chapter 4.

CHAPTER 6 CONCLUSIONS

Through research collaboration between the research team at West Virginia University (WVU) and Dr. J.H. Schneibel at Oak Ridge National Laboratory (ORNL), molybdenum-based alloys with dispersing $MgAl_2O_4$ or MgO spinel particles were developed at ORNL and evaluated at WVU through atomistic modeling analyses, thermo-mechanical tests, and metallurgical studies. Relevant conclusions are presented below.

6.1 Fracture toughness tests

Fracture toughness was evaluated for molybdenum silicide alloys through three-point-bending tests at different testing temperature. Detailed crack tip deformations were evaluated in-situ by applying high temperature moiré interferometry.

Using moiré interferometry, experimental data of crack tip deformation in grain level was observed. It clearly shows the grain boundary sliding for casting Mo, and strengthened grain boundaries for casting MoSi. From the atomistic modeling and simulation, it is confirmed that trace amount of residual oxygen may be responsible for grain boundary sliding in casting Mo alloy.

6.2 Thermo-mechanical tests

Tensile tests of molybdenum alloys with MgO or $MgAl_2O_4$ spinel particles were conducted at room temperature and 650°C and correlated with the material microstructure. Bending test results for alloy #678 showed drastic increase of ductility while other alloys tested did not show substantial ductility improvement. Further improvement of material processing is needed to obtain spinel-dispersed molybdenum alloys with desired ductility.

The coefficient of thermal expansion value changes with the method of processing. By adding 0.745% (wt) of silica to molybdenum, CTE value is less when compared to that of the pure molybdenum. In case of the molybdenum base alloy with spinel

($MgAl_2O_4$) particles at different percentage, as the percentage of the spinel particle increases, the CTE value decreases.

This research work showed that spinel particle size, distribution and processing time may greatly affect the ductility of molybdenum alloy, i.e.

1. Particle size and distribution plays an important role. For alloy #678, which has shown drastic room temperature ductility in bending test, over 90% particle is less than 10μm with fewer large spinel particles. But for alloys with either large particles or less evenly distributed particles, brittle failure is the dominate failure mode. At room temperature and much slower displacement loading rate, alloy #697 showed extensive microcracking before failure, while for alloy #698 , due to its fine particle dispersion in the Mo matrix, the microcracking only showed up near the failure locations.
2. Processing time may be a critical factor. With four hours processing time at 1800°C, the matrix and spinel may have stronger chemical bond. And with a longer processing time at high temperature, diffusion may help to disperse spinel particles evenly. Thermal cycle testing verified that one hour processing time may not be longer enough to generated proper chemical bond in the intermetallic compounds.
3. Microstructure study showed that for thermal cycle cracking, most of the cracks were initiated from the large size spinel particles, and ended in the matrix or connected to other large size spinel particles. The difference of coefficient of thermal expansion (CTE) among the alloys may be correlated to the observed difference of the thermal cycling cracking of the alloys.
4. The tested alloys exhibited strain rate sensitivity. At slower displacement rate, molybdenum alloys showed higher tensile elongation. At high temperature, all tensile tests showed increase of ductility.
5. Volume fraction of dispersed phase may also play an important role. However, more tests are needed to verify this assertion.

6.3 Microstructural analyses

Through thermo-cycle heat treatments of molybdenum base alloy with dispersed spinel ($MgAl_2O_4$) particles at two different temperature, 650°C and 1000°C, testing results were correlated to material microstructures. The following conclusions can be made:

1. Surface micro-cracking always originated from large spinel particle. Due to the fact that the thermal expansion coefficient of the matrix (Mo) and dispersed particles ($MgAl_2O_4$) does not match, and the irregular shape of spinel dispersion, hence under high temperature thermal cycling, stress will concentrate on the boundary between the matrix and the dispersed particles and crack will initiated from the spinel particle. Only micro-cracks is observed in alloy #732 suggested that dislocation flow is hindered by the finer distribution of dispersion.
2. The formation of molybdenum oxide can be seen mainly around and/or near spinel ($MgAl_2O_4$) particle. Large amount of molybdenum oxide was observed in alloy #697 and alloy #732. For alloy #678, the dispersion of spinel particle is evenly distributed, and the particle size is considerably finer than for alloy #697. Thus, it is not possible to detect the present of Molybdenum oxide in alloy #678.
3. It was revealed that further improvement of material processing is needed to obtain spinel-dispersed Mo alloys with high ductility. One can argue that alloy #678 had been hot-pressed for 4 hours compare to an hour for all other alloys, therefore rendering the higher ductility for alloy #678. Many literature reviews also stated that the introduction of fine dispersions has been postulated to improve ductility in body centered cubic (BCC) metals such as Mo by acting as a dislocation source, decreasing the effective slip plane length, or reducing dislocation pile ups at grain boundaries [49-50].
4. When the addition of spinel ($MgAl_2O_4$) particles is of excessive, as in the case of #697 (with 6wt%$MgAl_2O_4$), such effects may act as local notches, crack initiation sites, and significantly increase yield strength relative to cleavage strength. Although their presence may also be counteracted by impurity

segregation to and/or precipitation at the dispersion/Mo interface, the bigger spinel ($MgAl_2O_4$) particle size would getter excessive amount of Molybdenum oxide and thus defeated the purpose of ductilizing Molybdenum alloy.

6.4 Atomistic simulations

Through atomistic simulations, we have seen that the introduction of oxygen impurity has induced significant electronic charge redistribution in its nearby regions. Some electrons originally responsible for Mo-Mo metallic bonds are either withdrawn by oxygen to form ionic bonds, or swallowed by the first or second layer Mo's electron cloud to become more localized. Since these electrons (forming Mo-Mo metallic bonds) are crucial to hold the solid tight against distortion and to resist cracking, we conclude that the mechanical property is compromised, i.e. trace amount of residual oxygen at grain boundary promotes intergranual fracture. The fracture is most likely mediated through broken bonds between the second and third layer Mo, since the metallic bonding is significantly weakened there as indicated in our simulation.

This helps to explain the experimental observations. We see the unalloyed Mo with grain boundary oxygen impurities suffers from low fracture toughness. The observed failure type is mostly intergrannual fracture. When Si and B are included in the alloy system, they tend to form protective silica glass scale to prevent further oxidation. Therefore, depending on the microstructural morphology, the grain boundary oxygen impurity level will decrease, yielding a much tougher Mo phase. However, as the applied load ultimately exceeds the strength of Mo_3Si and Mo_5Si_2B, catastrophic failure (i.e. transgranular fracture) occurs due to the brittleness of the ceramic phases.

REFERENCE

[1]. www.fossil.energy.gov/programs/powersystems/futuregen

[2]. C. L. Briant, "High Temperature silicides and Refractory Alloys", MRS Symposia Proceedings, Boston, MA, Vol.322, pp.461-472, (1994).

[3]. M. R. Jackson, B. P. Bewlay, R.G. Rowe, D.W. Skelly, and H.A. Lipsitt, "High-Temperature Refractory Metal-Intermetallic Composites", JOM, Vol.48, pp.39-44,(1996)

[4]. M.J. Kramer, M. Akinc, A.J. Thom, J.J. Williams, and H.L. Zhao; J.H. Schneibel, C.J. Rawn, and C.L. Fu, in MRS Symposium Proceedings, 2001

[5]. C.A. Nunes, R. Sakidja, and J.H. perepezko, in "Structureal Intermetallics 1997", M.V. Nathal et al., eds., TMS, pp.831-839 (1997)

[6]. J.H. Schneibel, C.T. Liu, D.S. Easton, and C.A. Carmichael, "Microstructure and mechanical properties of Mo-Mo3Si-Mo5-SiB2Silicides", Materials Science and Engineering A261, pp. 78-83, 1999

[7]. Schneibel, J.H.; Easton, D.S.; Choe, H.; Ritchie, R.O. ; "Fracture toughness, creep strength and oxidation resistance of Mo-Mo3Si-Mo5SiB2 molybdenum silicides", Proceedings of the International Symposium on Structural Intermetallics, 2001, p 801-809

[8]. D. M. Scruggs, L. H. Van Vlack, and W. M. Spurgeon, "Reaction Between Nitrogen and Spinel in Chromium", J. Amer. Ceram. Soc. 51(1968) 473

[9]. M.P. Brady, I.M. Anderson, M.L. Weaver, H.M. Meyer, L.R. Walker, M.K. Miller, D.J. Larson, I.G. Wright, V.K. Sikka, A.Rar, G.M. Pharr, J.R. Keiser, and C.A. Walls, "Nitrogen Impurity Gettering in Oxide Dispersion Ductilized Chromium,", Mater. Sci. Eng. A358, pp.243-254 (2003)

[10]. D. M. Scruggs, "Ductile tungsten composition containing a spinel dispersed uniformly throughout," United States Patent 3,320,037, Patented May 16, 1967.

[11]. J. H. Schneibel, Oak Ridge National Laboratory, Jamie J. Kruzic and Robert O. Ritchie, Lawrence Berkeley National Laboratory, "Mo-Si-B Alloy development", Proceedings of the 17th Annual conference on Fossil Energy Materials, 2003.

[12]. http://www.tms.org/

[13]. Tsukagoshi, K.; Yoshida, S.; Takahashi, S.; Tsukino, T. and Kawada, Y. Design and operation of latest and advanced combined cycle plant Consideration of unit No. 4-1 Higashi Niigata thermal power station of Tohoku electric Power Co. Inc., Mitsubishi Juko Giho, 37(1), 2-5, 2000.

[14]. Ryohei Tanaka, "Research and development of ultra-high temperature materials in Japan", Materials at High Temperatures, v 17, n 4, 2000, p 457-464

[15]. Tanaka, R. "Past, present, and future of materials for high temperature applications", in Proceeding Symposium of Ultra-high Temperature Materials. 1-10, 1997

[16]. David Andrew Helmick, "High temperature oxidation behavior of Mo-Si-B base alloys", Dissertation, University of Pittsburgh, 2003

[17]. A.K.Vasudevan and J.Petrovic, "A comparative overview of molybdenum silicide composites", Mater. Sci. and Engng. A155(1992)1-17

[18]. Yao, Z.; Stiglich, J.; Sudarshan, T.S.; "Molybdenum silicide based materials and their properties", Journal of Materials Engineering and Performance, v 8, n 3, 1999, p 291-304.

[19]. Vander Voort, Metallography: Principles and Practice. Materials Science and Engineering Series, McGraw-Hill, 1984, 610-655.J. H. Schneibel, J. J. Kruzic, R. O. Ritchie, Proceedings of the 17th Annual Conference on Fossil Energy Materials Baltimore, MD, April 22-24, 2003, in print.

[20]. B.S. Kang, C. Feng, J. H. Schneibel, "Thermomechanical properties of molybdenum alloys with spinel particles", Twentieth Annual International Pittsburgh Coal Conference proceeding. Sep, 2003

[21]. H. Choe, D. Chen, J.H. Schneibel and R.O. Rithchie, Fracture and fatigue growth behavior in Mo-12Si-8.5B Intermetallics at ambient and elevated temperature, 2000 TMS proceedings Vander Voort, Metallography: Principles and Practice. Materials Science and Engineering Series, McGraw-Hill, 1984, 610-655.

[22]. Dieter, George Ellwood, Mechanical metallurgy, McGraw-Hill series in materials science and engineering, 1986

[23]. Donald R. Askeland, "The Science and Engineering of Materials." Pg: 240 & 651

[24]. http://imoa.org.uk

[25]. http://mineral.galleries.com/minerals/oxides/spinel/spinel.htm

[26]. C.L.Fu and X.Wang, "Thermal Expansion coefficients of Mo-Si compounds by first-principles calculations" ,Philosophical Magazine Letters 2000, vol 80, No 10 683-690.

[27]. J. H. Schneibel, J. J. Kruzic, R. O. Ritchie, Proceedings of the 17th Annual Conference on Fossil Energy Materials Baltimore, MD, April 22-24, 2003, in print.

[28]. Joachim H. Schneibel**,** Claudia J. Rawn, Chong Long Fu., "Tailoring the thermal expansion anisotropy of Mo5Si3." Oak Ridge National Laboratory.

[29]. C.L. Fu and Xindong Wang., "Thermal expansion coefficients of Mo-Si compounds by first principles calculations." Oak Ridge National Laboratory.

[30]. Misra, J.J.Petrovic and T. E. Mitchell., "Microstructures and Mechanical properties of a Mo3Si- Mo5Si3 composite." Los Alamos National Laboratory.

[31]. J.H. Schneibel**,** and C.A.Carmichael., " Processing and properties of Molybdenum silicide intermetallics containing boron." Oak Ridge National Laboratory.

[32]. C.J.Rawn, J.H.Schneibel, C.M. Hoffmann and C.R.Hubbard. "The Crystal Structure and Thermal Expansion of Mo_5SiB_2" Metals and Ceramics Division, Oak Ridge National Laboratory, Oak Ridge, TN 37831.

[33]. M. K. Meyer, M. J. Kramer, and M. Akinca [sic], "Compressive creep behavior of Mo5Si3 with the addition of boron," Intermetallics 4 (1996) 273-281.

[34]. M. Akinc, M. K. Meyer, M. J. Kramer, A. J. Thom, J. J. Huebsch, and B. Cook, "Boron-doped molybdenum silicides for structural applications," Intermetallics A261 (1999) 16-23.

[35]. M. K. Meyer, A. J. Thom, and M. Akinc, "Oxide scale formation and isothermal oxidation behavior of Mo-Si-B intermetallics at 600-1000°C," Intermetallics 7 (1999) 153-162.

[36]. D. M. Berczik, United States Patent 5,595,616 (1997), "Method for enhancing the oxidation resistance of a molybdenum alloy, and a method of making a molybdenum alloy."

[37]. D. M. Berczik, United States Patent 5,693,156 (1997), "Oxidation Resistant Molybdenum Alloys."

[38]. J. A. Shields Jr., Advanced Mat. & Proc., 10/92, 1992, p.28.

[39]. Archer, Briggs and Loeb, "Molybdenum: Steels, Irons, Alloys." Climax Molybdenum Company, New York, 1948.

[40]. www.buehler.com.

[41]. R. W. James, "Solid State Physics" (ed. F. Seitz, D. Turnbull), 15, Academic 1963, p55-120.

[42]. W. H. Zachariasen, *Theory of X-Ray Diffraction in Crystals*, Wily, 1967.

[43]. Cosslett, V. E. (1950) "Introduction to Electron Optics", O.U.P., Oxford, p68-100.

[44]. JEOL JSM-6400 SEM Operation Manual.

[45]. Barbi, N. C. and D. B. Lister (1981) *Energy-Dispersive Spectrometry*, Heinrich, Newbury, Myklebust, Fiori, eds. NBS Special Publication 604, 35-44.

[46]. Hall, T. A. and B. L. Gupta (1986) in *Principles of Analytical Electron Microscopy*, Joy, Romig, and Goldstein, eds. Plenum New York, 219-248.

[47]. Haasen, P, "Physical Metallurgy", Cambridge University Press 1996, p305.

[48]. Henkel Daniel P, Pense Alan W, "Structures and properties of engineering materials", 5, McGraw-Hill, p127-131.

[49]. Wilcox BA, Veigel ND, Clauer AH. Met. Trans.; 1972 3:273.

[50]. Jiuxing Z, Lu L, Meiling Z, Yancao H, and Tieyong Z. Int J. Refractory Hard Mater.; 1999 17: 405.

[51]. Siegel, R.W., E. Hu, and M.C. Roco, eds. 1998. *R&D status and trends in nanoparticles, nanostructured materials, and nanodevices in the United States*. Baltimore: Loyola College, International Technology Research Institute. NTIS #PB98-117914.

[52]. Shull, R.D. 1998. NIST activities in nanotechnology. In *R&D Status and Trends*, ed. Siegel et al.

[53]. Salishekev, G.A., O.R. Valiakhmetov, V.A. Valitov, and S.K. Mukhtarov. 1994. *Materials Science Forum*. 170-172:121.

[54]. Mishra, R.S., R.Z. Valiev, and A.K. Mukherjee. 1997. *Nanostructured Materials* 9:473.

[55]. Daniel Post, Bongtae Han, Peter Ifju, "High sensitivity moiré: experimental analysis for mechanics and materials", Springer, 1994.

[56]. B.S. –J, Kang, J. Skeen, K. Perry and Y.Y. Hung, “Crack tip displacement measurements using automated phase shift moiré interferometry”, 1997 SEM spring conference on experimental mechanics, pp311-312, Bellevue, WA, 1997.

[57]. D.L. Price, B.R. Cooper, and J.M. Wills, “Full-potential linear-muffin-tin-orbital study of brittle fracture in titanium carbide”, Physical Review B, 46, pp.11368-11375 (1992)

[58]. D.L. Price, B.R. Cooper, and J.M. Wills, “Linear-muffin-tin-orbital calculation of TaC(001) surface relaxation”, Physical Review B, 46, pp.15301-15310 (1993)

[59]. H. Choe, D. Chen, J.H. Schneibel, R.O. Ritchie, "Ambient to High Temperature Fracture Toughness and Fatigue-Crack Propagation Behavior in a Mo-12Si-8.5B (at.%) Intermetallic," Intermetallics, 9, pp.319-329 (2001).

[60]. J. H. Schneibel, P. F. Tortorelli, M. J. Kramer, A. J. Thom, J. J. Kruzic, and R. O. Ritchie, “Optimization of Mo-Si-B Intermetallics,” in Defect Properties and Related Phenomena in Intermetallic Alloys, E. P. George, M. J. Mills, H. Inui, G. Eggeler, eds., MRS Symposium Proceedings, vol. 753, Materials Research Society, Warrendale, PA, BB2.2.pp.1-6. (2003)

[61]. J. J. Kruzic, J. H. Schneibel, R. O. Ritchie,“Fracture and Fatigue Resistance of Mo-Si-B Alloys for Ultrahigh-Temperature Structural Applications,” Scripta Materialia, 50 (4), pp.459-464 (2004)

[62]. J.C. Slater and G.F. Koster, “Simplified LCAO method for the periodic potential problem”, Physical Review 94, pp.1498-1524 (1954)

[63]. D.A. Papaconstantopoulos, “Handbook of the Band Structure of Elemental Solids,” Plenum, New York, (1986)

[64]. D.A. Papaconstantopoulos and M.J. Mehl, “Applications of a tight-binding total-energy method for transition and noble metals: Elastic constants, vacancies, and surfaces of monatomic metals”, Physical Review B 54, pp.4519-4530 (1996)

[65]. D.A. Papaconstantopoulos and M.J. Mehl, “Precise tight-binding description of the band structure of MgB_2”, Physical Review B 64, pp.172510-172513 (2001)

[66]. A.K. McMahan and J.E. Klepeis, “Direct calculation of Slater-Koster parameters: Fourfold-coordinated silicon/boron phases”, Physical Review B 56, pp.12250-12262 (1997)

[67]. D.L. Price, B.R. Cooper, and J.M. Wills, "Full-potential linear-muffin-tin-orbital study of brittle fracture in titanium carbide", Physical Review B, 46, pp.11368-11375 (1992); D.L. Price, B.R. Cooper, and J.M. Wills, "Linear-muffin-tin-orbital calculation of TaC(001) surface relaxation", Physical Review B, 46, pp.15301-15310 (1993)

[68]. D. Djajaputra and B.R. Cooper, Physica Status. Solidi. (b) 236, pp.97

[69]. O.K. Andersen and O. Jepsen, "Explicit, first-principles tight-binding theory", Physical Review Letters, 53, pp.2571-2574 (1984)

[70]. Th. Frauenheim, F. Weich, Th. Kohler, S. Uhlmann, D. Porezag, and G. Seifert, "Density-functional-based construction of transferable nonorthogonal tight-binding potentials for Si and SiH", Physical Review B, 52, pp.11492-11501 (1995)

[71]. C.Z. Wang, B.C. Pan, M.S. Tang, H. Haas, M. Sigalas, G.D. Lee, and K.M. Ho, MRS Symposium Proceedings, 491, pp.211

[72]. M.S. Daw, S.M. Foiles, and M.I. Baskes, Material Science Rep, 9, pp251

[73]. N.W. Ashcroft and N.D. Mermin, "Solid State Physics", Saunders College, Philadelphia, (1976) pp.425